GROUND TEST ANALYSES OF THE AFOSR BOUNDARY LAYER TRANSITION (BOLT) FLIGHT GEOMETRY

A Thesis

by

HEATHER EMILY KOSTAK

Submitted to the Office of Graduate and Professional Studies of
Texas A&M University
in partial fulfillment of the requirements for the degree of

MASTER OF SCIENCE

Chair of Committee,	Rodney D.W. Bowersox
Committee Members,	Helen L. Reed
	Simon W. North
Head of Department,	Rodney D.W. Bowersox

May 2020

Major Subject: Aerospace Engineering

ABSTRACT

The Air Force Office of Scientific Research Boundary Layer Transition (BOLT) flight experiment is a collaboration between academia, government, and industry. The objective was to challenge the hypersonic aerodynamics community to predict transition in flight for a complex geometry. Quantifying the transition mechanisms on the BOLT geometry is the topic for this thesis. Experiments were performed in a range of ground test facilities, including the TAMU ACE and Mach 6 Quiet tunnels, the Purdue BAM6QT, the NASA 20-inch Mach 6 Air Tunnel, and the CUBRC LENS II facility. The measurements included surface temperature and heat flux maps, high-frequency surface pressure fluctuations, and mass flux contours. The results were compared across the facilities and with quiet direct numerical simulation (QDNS) results from the University of Minnesota. The surface heating under quiet conditions was characterized by a streak structure, and the results were found to agree to within 10% across both quiet tunnels and with the QDNS. Transition was not observed under quiet conditions. However, the boundary layer spectral content indicated instability growth (20-40 kHz) in a primary streak just off of the centerline. Conversely, transition was observed in all of the conventional noise facilities. The modal growth was similar across all facilities, regardless of the freestream environment. The instability within the primary streak roll-up was examined in more detail in the TAMU M6QT using hot-wire anemometry. The surface pressure spectra and 2-D contours showed similar modal growth. The flow structure and instability locations were in qualitative agreement with the simulation results.

DEDICATION

To my dad,

For encouraging me, believing in me, and pushing me to be myself.

I hope I made you proud.

ACKNOWLEDGMENTS

Without the knowledge and encouragement from amazing colleagues and advisors, both past and present, a lot of work presented in this thesis would not have been accomplished. Although the list would be pages long, there are a few people that I would like to acknowledge here.

First and foremost, I would like to thank my advisor, Dr. Rodney Bowersox for persuading me to continue my graduate level education at Texas A&M University. Overall, it has been a bumpy ride, but I am grateful for every accomplishment we've had along the way. I have him to thank for the continuous encouragement and optimism throughout this campaign. He truly is a one-of-a-kind advisor that puts so much faith in each of his students.

Thank you to my committee members, Drs. Helen Reed and Simon North. Working alongside your students both in and out of the lab truly shows me how much you care for our success in our research and studies.

I must thank Dr. Jerrod Hofferth for recommending me to take on research as an undergraduate at the Flight Research Laboratory despite my novice coding skills in his class. He is also the person to thank for my very first internship in college with the Air Force Research Laboratory in Tullahoma, TN as well as an overall interest in graduate school. I must thank Dr. William Saric for hiring me on as a sophomore undergraduate in his lab and teaching me that only those who work hard are recognized in life.

I have a few people at the NAL to thank, both past and present, for helping me along the way. Thank you to Ian Neel and Andrew Leidy for passing down generations of knowledge and expertise to me. I must thank both of them for being so patient with my continuous questions. The NAL ran so smoothly with both of them. They truly were the dream team. Thank you to Casey Broslawski, Tyler Dean, and Farhan Siddiqui. These guys got me through the PhD qualifying exams, kept my spirits high throughout my research campaigns, and helped me whenever they could. Thank you to Zachary Buen and Madeline Smotzer for keeping my feet on the ground and making me laugh every day at the lab. I must thank Cecil Rhodes, Rebecca Marianno, and Colleen Leatherman for their organizational skills and keeping the NAL on track with maintenance, purchase orders, and meetings. Without them, the lab would not function properly.

Thank you to my parents, James and Monica Kostak, for supporting me every day throughout my degree. I hope to have made both of you proud.

Finally, I must thank Coleton James Teplicek, my fiancé, for standing by my side for over six years at the time of writing this thesis. He gave me the most encouragement throughout my studies, both undergraduate and graduate, and never failed to kindly remind me that there is more to life than work. I would not have made it through this degree in one piece without him.

CONTRIBUTORS AND FUNDING SOURCES

Contributors

This work was supported by a thesis committee consisting of Professors Rodney Bowersox (advisor) and Helen Reed of the Department of Aerospace Engineering and Professor Simon North of the Department of Chemistry.

A large contribution of data were provided by Purdue University, NASA Langley Research Center, Johns Hopkins University Applied Physics Laboratory, CUBRC, and University of Minnesota. Unless otherwise noted, the data contained in this thesis were processed and analyzed by the student independently. The current work contains comparisons of experimental and computational results from past and present work.

Funding Sources

The work presented in this thesis could not have been accomplished without the help from the United States Air Force Office of Scientific Research through grant number FA9550-18-1-0010 (Program Manager Dr. Ivett Leyva). The author spent the summer of 2018 at JHUAPL with the Force Projection Sector processing and analyzing data contained in this thesis. The author also participated in wind tunnel testing at NASA Langley for some of the work presented in this thesis.

NOMENCLATURE

ACE	Actively Controlled Expansion tunnel
f	frequency
M6QT	NASA Langley Mach 6 Quiet Tunnel
BAM6QT	Boeing/AFOSR Mach 6 Quiet Tunnel
i	spatial coordinate for heat conduction equation
IR	infrared
K#	Kulite at location #
M	Mach number
n	time coordinate for heat conduction equation
p_0	tunnel stagnation pressure
p_{t2}	Pitot pressure in test section (p_{t2}= mean, p'_{t2}= rms)
P#	PCB at location #
Q (or q)	heat flux in $\frac{W}{m^2}$
Re	Reynolds number
r/r_{exit}	fractional lateral distance along nozzle plane
rms	root mean square
St	Stanton number
t	time
T	temperature in kelvin
μm	micrometer

width	z-span of BOLT in inches
X/L	fractional distance along nozzle length
z	spanwise location off the centerline of BOLT (in m, in, or mm)
ΔT	change in temperature in kelvin
′	fluctuation
PEEK	polyetheretherketone
AEDC	Arnold Engineering Development Complex
AFRL	Air Force Research Laboratory
T_0	total temperature
PU	Purdue
ZnSe	Zinc selenide
α	thermal diffusivity in m/s
κ	thermal conductivity in $\frac{W}{m^2 \cdot K}$
c_p	specific heat capacity in $\frac{J}{kg \cdot K}$
ρ_∞	freestream density
U_∞	freestream velocity
T_w	temperature at the wall
DNS	direct numerical simulation
CFD	computational fluid dynamics
KEC	Kinetic Energy Consistent
$u_\xi^{'}$	freestream velocity perturbation
PSD	power spectral density

AoA	angle of attack
ρU	mass flux in $\frac{kg}{m^2 \cdot s}$
V_b^2	bridge voltage
LST	linear stability theory

TABLE OF CONTENTS

Page

LIST OF FIGURES

Page

LIST OF TABLES

Page

1. INTRODUCTION

1.1 Background and Motivation

1.1.1 Hypersonics and Boundary Layer Transition

Understanding the process and mechanisms that lead to transition is critical when developing a hypersonic vehicle. Upon reaching hypersonic speeds in flight, surface heating leading to higher skin friction drag becomes a main source for transition of the boundary layer from laminar to turbulent. The flow passing over the vehicle can introduce coupling of mechanisms and instabilities causing breakdown on the vehicle with a result of increased drag. These stability mechanisms are dependent on the geometry (concave and convex surfaces; swept leading edges) and the environment. Pressure gradients on the surface and curvature of the geometry introduce unique instabilities and interactions of these modes, but the environment the vehicle is tested in - Reynolds number, wall temperature, roughness, and freestream conditions - can cause welcoming (or unwelcoming) effects. Transition is an initial value problem heavily dependent on the upstream initial conditions. Receptivity is the result of environmental disturbances entering the boundary layer causing steady and unsteady fluctuations [1]. Within the hypersonic community, receptivity is still an unsolved problem in the field. Amplitudes, phase, and frequency are dependent on receptivity for the breakdown of laminar flow [2]. The well-known figure from Morkovin of the turbulence onset problem [3] is shown in Figure 1-1. The figure portrays the complex nature of breakdown instigated by numerous processes in many different ways. The work presented in this thesis follows the path

labeled ‘A’ in the roadmap. The other paths are well explained and documented in previous works [3, 4]. Path A begins with weak environmental disturbances where receptivity is dependent on the initial growth described by linear stability theory (LST) of primary modes, i.e. the linearized, unsteady, Navier Stokes equations. These instabilities (crossflow, first- and second-mode, etc.) can occur independently or together and are highly dependent on the geometry, flow conditions, roughness, and initial conditions. As the amplitude increases, nonlinear interactions of the modes occur leading to secondary instabilities, which in turn quickly lead to breakdown and into turbulence.

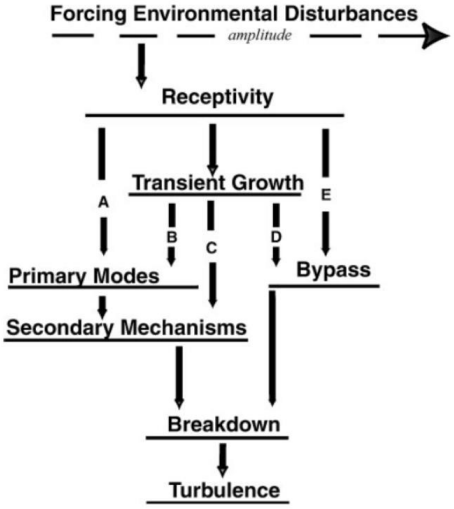

Figure 1-1. Different paths leading to transition from laminar to turbulent flow (reprinted from [3]).

For experiments and computations, understanding the receptivity process, the linear stability of a problem, and ending with the nonlinear breakdown is critical in hypersonic flow. Early work on hypersonic boundary layer stability focused primarily on 2-D planar and axisymmetric shapes with insight on the first- and second-mode instability mechanisms by Mack [5-7]. More complex geometries, such as elliptic cones, provided

insight on the stability and transition mechanisms within a 3-D boundary layer. Crossflow increases the amplification rate of the most unstable first mode wave, which is two-dimensional in nature and amplifies the most unstable second mode wave which may be oblique [8]. The traveling crossflow instability was found to be not as critical in a low-disturbance environment but was predicted to have higher growth rates than stationary crossflow. Stationary crossflow produces early nonlinear effects with a strong dependence on surface roughness and receptivity [2, 9, 10]. To-date, many experiments have been completed and indicate that the basic stability mechanisms in 3-D boundary layers consist of multiple modes with some occurring simultaneously, e.g. first modes, second modes, stationary and traveling crossflow, and secondary instabilities [11-17].

1.1.2 Hypersonic International Flight Research Experimentation

Elliptic cones have been a major focus in boundary layer stability within the hypersonic regime since the geometry is easily described analytically with a body resembling a hypersonic vehicle [8]. Several phenomena occur on 3D geometries that are not present on axisymmetric configurations, such as leading-edge and attachment line transition and contamination caused by the leading edge radius and sweep of the geometry [18]. Early work involved an elliptic cone with an aspect ratio of 2:1 tested at a freestream Mach number of 8 in the Von Karman Gas Dynamics Facility Tunnel B at the Arnold Engineering Development Center (AEDC). The stainless steel cone featured a half angle of 7° with respect to the minor axis and a nose radius of 40 μm along the major axis. Two traveling waves were seen on the model with Schlieren imagery: ‘rope-like waves’ seen on axisymmetric models and elongated streaks oriented 5° from the cone surface [8, 19].

Frequency content above the surface using hot-wire anemometry showed growth around 10 kHz and 70 kHz near the leading edge of the cone ($\theta = 90°$). Flow along the centerline on the top of the cone proved unstable where higher frequencies were obtained, around 60-80 kHz. The strong pressure gradient located on the elliptic cone drives the flow from the leading edge toward the top of the centerline. More recently, this effect has been seen and verified in experiments, simulations, and in flight on a 2:1 elliptic cone geometry for the Hypersonic International Flight Research Experimentation (HIFiRE) program [20].

The HIFiRE program was developed by the U.S. Air Force Research Laboratory (AFRL) and Australian Defense Science and Technology to further the understanding of boundary layer transition for development of technology that is critical for advancement in hypersonics. The flight test program not only features an elliptic cone producing a 3-D flow configuration (HIFiRE-5A&B), but also a 7° half angle axisymmetric cone with a nose radius of 2.5 mm (HIFiRE-1). The HIFiRE-5 flight geometry, which features similar instabilities that occur on the surface of BOLT, has a 2:1 elliptic cross section with a 7° half angle along the minor axis. Many ground tests and computations have been made with a 38.1% scale of the geometry leading up to the flight tests as well as after [16, 21-25]. The elliptic cone enhances natural transition on the surface which results in the crossflow instability dominating. A simulation at Mach 6 on the 38.1% scale model in Figure 1-2a represents the intrinsic dynamics and complexity of the 3-D mean flow upon the surface [20]. The black lines represent streamlines traveling from the leading edge to the centerline (an effect previously seen experimentally with oil-flow [26] in Figure 1-2b) where the cross-sectional slices represent Mach number contours [20]. Both simulation and

experimental work verify the pressure gradient along the leading edge forcing flow to the centerline. The mushroom-like roll-up effect along the centerline, shown in Figure 1-2a, is similar to a feature seen on BOLT.

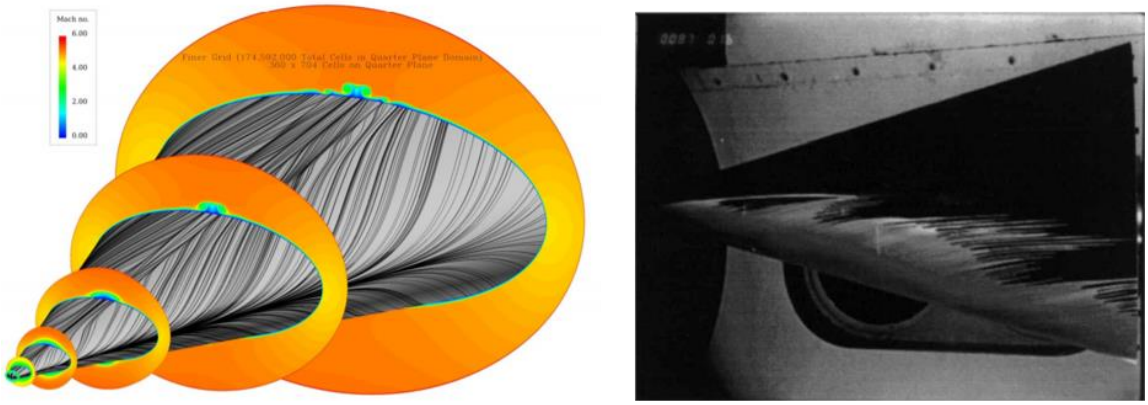

(a) (b)

Figure 1-2. (a) HIFiRE-5 simulation at Mach 6 (reprinted from [20]) and (b) oil-flow visualization on a 2:1 elliptic cone at Mach 8 (reprinted from [26]).

The majority of this paper focuses on quantifying the effects of transition in different facilities on various scale models of BOLT with comparisons with computations. A similar study was previously done on the 38.1% scale model of the HIFiRE-5 2:1 elliptic cone geometry [13, 16, 21, 22]. Subscale models of the HIFiRE-5 geometry have been tested in numerous wind tunnel facilities to gain an understanding of environmental effects on the model [11-16, 21, 22, 24, 25, 27-31]. To quantify these effects, comparisons were made with fast-response surface pressure transducers, IR thermography, Schlieren imaging, oil flow, and temperature sensitive paint (TSP). Results have shown that the crossflow instability is the dominant path causing boundary layer transition. Subscale models were tested in quiet and conventional facilities at Purdue University and Texas A&M University with the corresponding models shown in Figure 1-3.

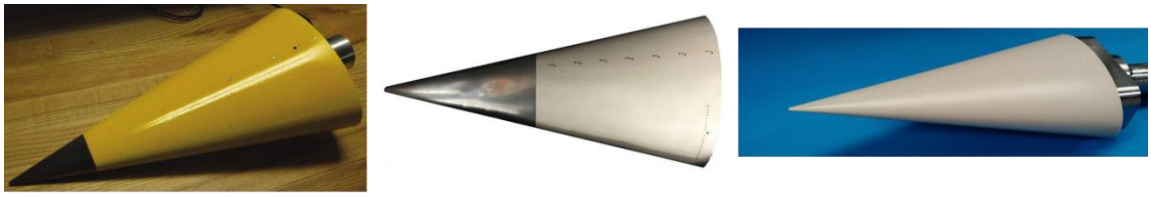

(a) (b) (c)

Figure 1-3. 38.1% subscale models of the HIFiRE-5 2:1 elliptic cone geometry. (a) Juliano et al. 2015 (reprinted from [11]), (b) Borg et al. 2016 (reprinted from [14]), and (c) Neel et al. 2017 (reprinted from [21])

Heating on the surface of the 38.1% scale HIFiRE-5 was observed through IR thermography (Borg et al. 2016 & Neel et al. 2017) and TSP (Juliano et al. 2015). A high emissivity and high temperature polyetheretherketone (PEEK) plastic was used for viewing the heating on the surface for experiments by Borg et al. and Neel et al. The surface for Juliano et al. experiments was painted with a Ru(bpy) luminosphore dissolved in ethanol, mixed into a clear paint, and applied on top with several coats of Top Flite LustreKote spray paint [11]. Testing of the TSP painted model and the half-PEEK model were in the Purdue Boeing/AFOSR Mach 6 Quiet Tunnel (BAM6QT). Neel et al. studies were in the Mach 6 Quiet Tunnel (M6QT) and Actively Controlled Expansion (ACE) tunnel at Texas A&M. A direct comparison of heat flux on the surface in conventional flow for the three models is shown in Figure 1-4. The Reynolds number is given above each image for reference and the viewing area of the model in the tunnel of each facility was limited by the window area. The heat flux results were computed by Juliano et al., Borg et al., and Neel et al. individually. With a comparable Reynolds number, a similar magnitude and structure of heating is seen on the model between the different wind tunnel campaigns in Figure 1-4. Even with different freestream environments, the results on the 38.1% scale models in the BAM6QT and ACE look promising. Testing of the same

models in quiet flow were made and compared between the M6QT and BAM6QT in Figure 1-5. With different freestream environments, the structures on the surface of the elliptic cone in Figure 1-4 and Figure 1-5 are evidently different. Defined streaks in the streamwise direction are seen at lower Reynolds numbers; with an increase in Reynolds number, transition occurs and the streaks travel upstream on the model [15, 32]. Transition is referenced as the sudden increase in heating on the model.

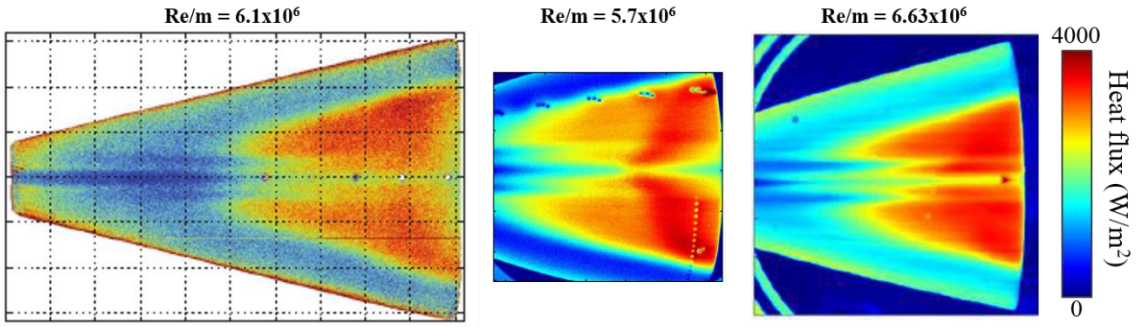

Figure 1-4. Heat flux comparison for conventional flow. (a) Juliano et al. 2015 (reprinted from [11]), (b) Borg et al. 2016 (reprinted from [14]), and (c) Neel et al. 2017 (reprinted from [21])

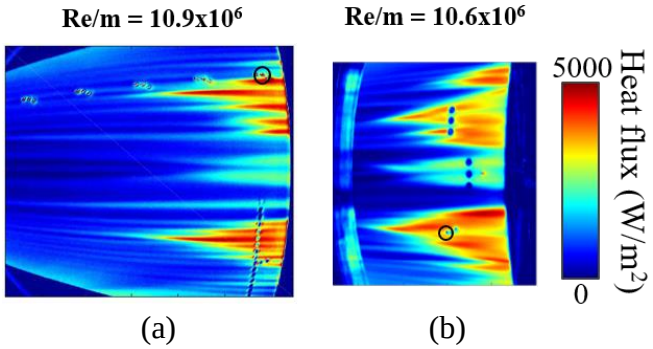

Figure 1-5. Heat flux comparison for quiet flow. (a) Borg et al. 2017 (reprinted from [15]) and (b) Neel 2019 (reprinted from [32])

High frequency Kulite surface pressure transducers were inserted in locations where transition was observed on the 38.1% scale elliptic cone. In Figure 1-5, the sensors

circled in black are for comparison. The Kulite location for discussion on the model by Borg et al. 2017 is further outboard and further downstream on the model than the location for the Neel 2019 studies. The power spectral density (PSD) spectra for the two Kulites in quiet flow are given in Figure 1-6, where the legend represents the freestream Reynolds number for each colored line in the plot. The spectra are normalized by the tunnel static pressure with respect to the facility. At similar locations on the model, but seen more clearly in Figure 1-6a, a peak frequency centered around 45 kHz starts to grow and is overtaken by turbulence at higher Reynolds numbers. The peak is observed in Figure 1-6a and Figure 1-6b around Re/m = 7.6×10^6 and Re/m = 8.7×10^6, respectively. The structure is the traveling crossflow instability that is also seen in computations around the same location and frequency [33]. However, at the same location on the model in noisy flow, the traveling crossflow instability is not apparent in Figure 1-7. Both plots are normalized differently, but no structure around 45 kHz is present. The spectra show that with an increase in Re/m, the boundary layer progresses from laminar to fully turbulent [14]. The comparisons between conventional and quiet flow show how a freestream environment in a facility can produce different results on wind tunnel models.

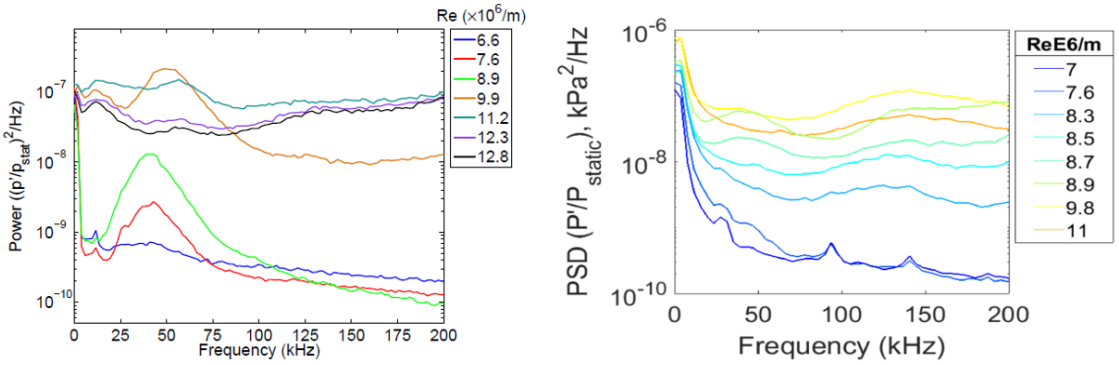

(a) (b)

Figure 1-6. Comparison between Kulite sensor measurements in quiet flow. (a) Borg et al. 2016 (reprinted from [14]) and (b) Neel 2019 (reprinted from [32])

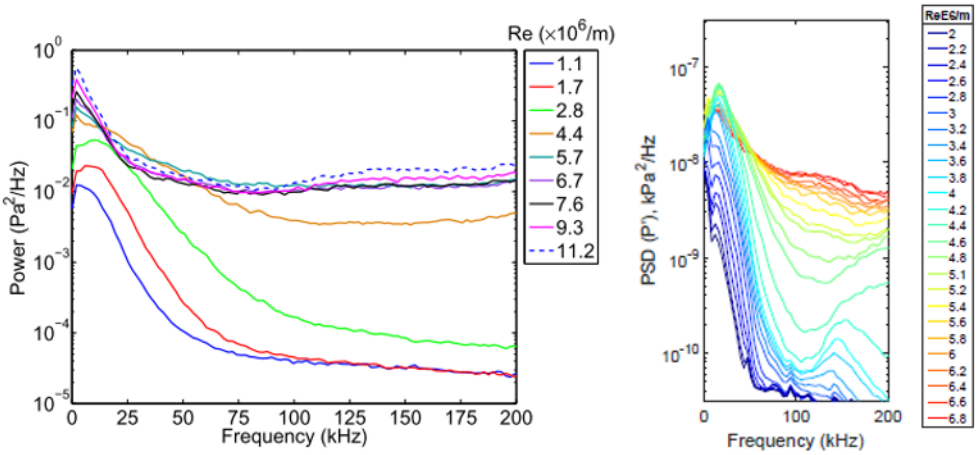

(a) (b)

Figure 1-7. Comparison between Kulite sensor measurements in noisy flow. (a) Borg et al. 2016 (reprinted from [14]) and (b) Neel 2019 (reprinted from [32])

With improved knowledge of both ground testing and simulations, post-flight comparisons were made with the HIFiRE-5 flight data [34-37]. No wind tunnel in the world can replicate all conditions in a flight environment. Therefore, pieces of data between ground testing and simulation must be combined together to fully understand the big picture of a hypersonic vehicle in flight. The transition Reynolds number is plotted with respect to the angular location from 0° to 90° for the HIFiRE-5 geometry in Figure 1-8 [35]. It is seen that the transition Reynolds number is vastly different between

conventional flow and flight, but more comparable between flight and quiet environments. Various conclusions can be drawn from the data between wind tunnel experiments and flight. Along the centerline, transition was observed at lower Reynolds numbers in flight as well as ground tests. However, centerline transition in noisy flow occurred at much lower Reynolds numbers than in quiet and flight environments. From linear stability theory (LST), crossflow was proven to be the dominant instability at φ=45° [35]. This instability at this location was present in quiet flow, flight test, and conventional flow.

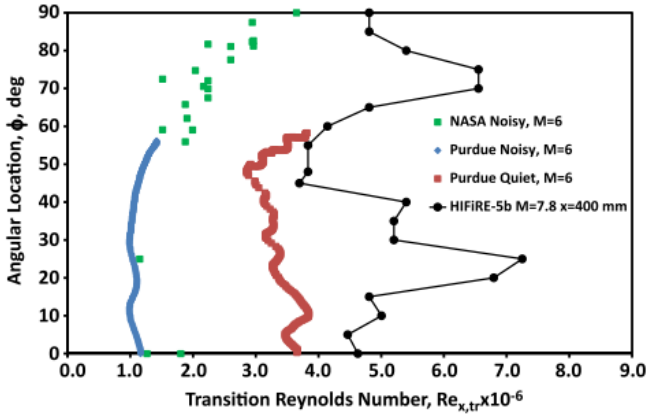

Figure 1-8. Noisy and quiet wind tunnel transitions compared to flight for the HIFiRE-5 geometry (reprinted from [35]).

The HIFiRE-5 program was successful at gathering valuable transition information on an elliptic cone geometry. The program challenged the hypersonic community, which in turn, an abundance of knowledge and understanding were obtained on both traveling and stationary crossflow and their existence with respect to the freestream environment. The freestream disturbance environment in wind tunnel facilities proves to be of importance when analyzing its' effects on wind tunnel models. These 3-D geometries provide insight into understanding the stability and transition mechanisms occurring on

hypersonic vehicles not only in flight but also through ground test facilities. Assessing modern prediction of transition at hypersonic speeds and understanding the mechanisms that cause these phenomena provides insight for future analyses and development of state-of-the-art tools. This goal led to the development of the Boundary Layer Transition (BOLT) flight test experiment.

1.1.3 Boundary Layer Transition (BOLT)

The Air Force Office of Scientific Research (AFOSR) Boundary Layer Transition (BOLT) flight test experiment was proposed to challenge the ability of modern ground simulation and experiment to predict transition in flight. Unlike the HIFiRE-1 and HIFiRE-5 geometries with convex surfaces, the features on BOLT involve concave surfaces with swept leading edges, including a 2-D leading edge, which is different from the well-studied planar bodies and axisymmetric shapes. The assembly of BOLT is made up of four surfaces: a symmetric upper and lower surface where the majority of experimental measurements are taken and two side "gutter" surfaces designed to isolate the flow of the swept leading edges. The concept behind the shape is to excite 3-D crossflow instabilities [38] and to challenge current tools for transition prediction. The complex geometry developed by a collaboration between the University of Minnesota, AFOSR, AFRL, and Purdue University is shown in Figure 1-9 with the full rocket-stack configuration in Figure 1-10.

Figure 1-9. Three-dimensional view of the complex BOLT geometry (reprinted from [38]).

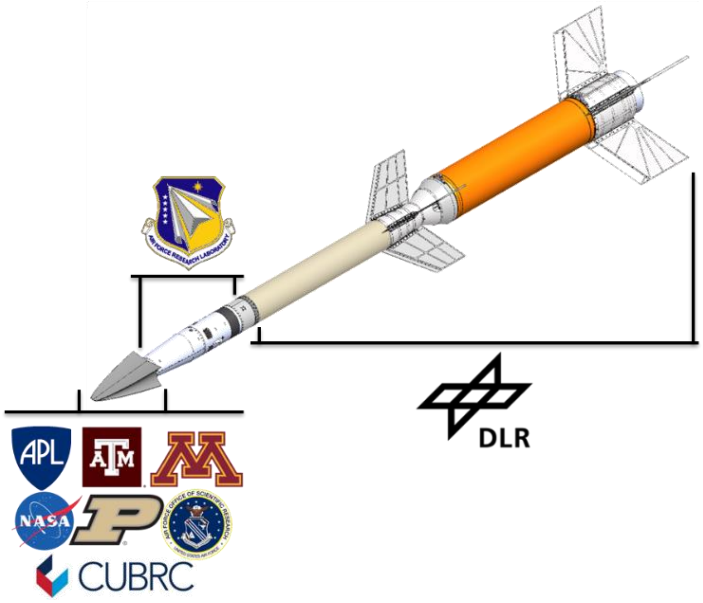

Figure 1-10. BOLT rocket stack with organizations involved.

Previous simulation results, shown in Figure 1-11 for a quarter of the geometry, show that the flow moves towards the centerline, creating an opportunity for crossflow instabilities and a centerline upwelling of flow with streamwise vortices. Computations from Texas A&M validate the presence of second-mode, stationary crossflow, and traveling crossflow on the surface [39-41]. A large counter-rotating vortex is seen along

the centerline region, similar to what was seen on the HIFiRE-5 model [20, 38]. Contour slices in Figure 1-11 represent the streamwise velocity component of magnitude designated as the colorbar to the right of the image. Due to the 3-D nature of the nosetip, a spanwise pressure gradient forms at the leading edge, causing a strong spanwise shear with vorticity within the boundary layer shown in Figure 1-12 [38]. The strength of this vortex is dependent on the Reynolds number.

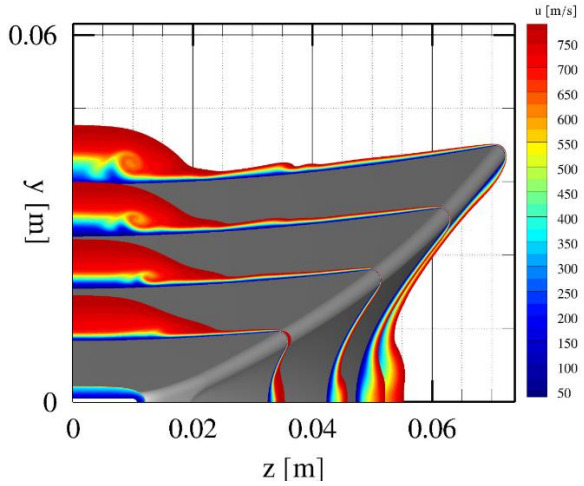

Figure 1-11. Mean flow of BOLT (reprinted from [38]).

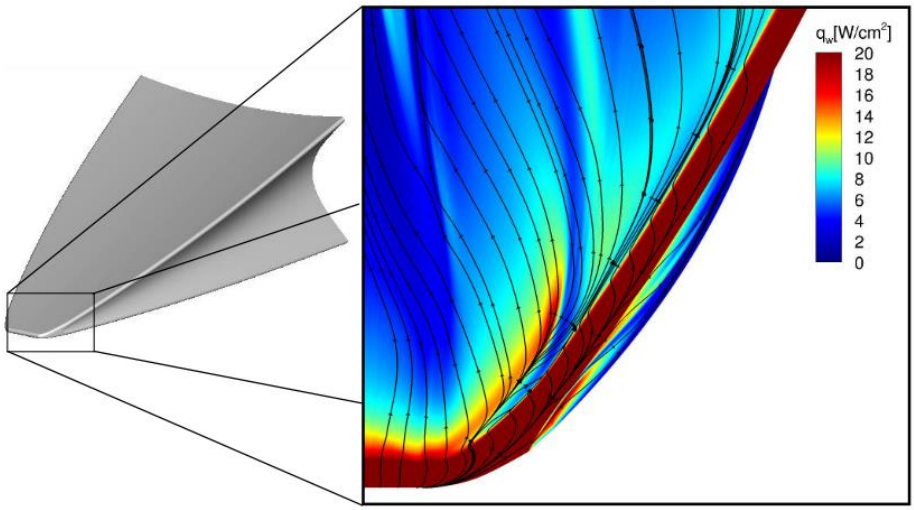

Figure 1-12. Close-up view of the BOLT nosetip. Streamlines are produced from the shear stress. Contour at the wall is of heat flux (reprinted from [38]).

The complexity of this vortex led to studies of capturing instabilities off the surface of BOLT by 'forcing disturbances' through direct numerical simulation (DNS) in the flow-field. The method utilizes low-dissipation with a shock capturing method that helps in analyzing the transition process on the surface [42]. University of Minnesota computed a forced numerical simulation by sparsity-promoting dynamic mode decomposition (SPDMD) to investigate stability and transition off the surface of BOLT [42, 43]. SPDMD was used to extract amplified perturbations in the boundary layer from spanwise invariant, wall-normal momentum forcing [42, 43]. By introducing a forcing term upstream with perturbations introduced into the boundary layer, modes and instabilities grow downstream on the surface of BOLT, shown in Figure 1-13, where traveling crossflow and brief upstream second-mode instabilities are present. The red and blue colors represent both the positive and negative streamwise velocity perturbations $u'_{\xi} = \pm 3x10^{-6}$ m/s. Two additional features are also observed: a mixed mode containing a range of frequency content that is oblique and localized near the boundary layer edge and a vortical mode near the centerline due to the roll up of the boundary layer [42, 43].

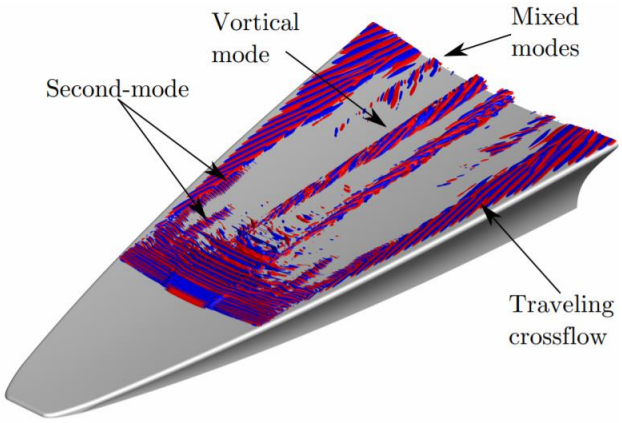

Figure 1-13. Isosurface of streamwise velocity perturbation. Half of the BOLT model is shown. Results are for a 33% scale model at Re/m = 9.9×10^6 (reprinted from [43]).

The unique features and instabilities on the surface of BOLT have posed as a challenge for current tools and analyses. The hope is that with wind tunnel testing at Purdue University, Texas A&M University, NASA Langley Research Center, and CUBRC along with computational analyses from the University of Minnesota and Texas A&M, the mechanisms causing transition in flight can be determined.

1.2 Research Objective and Approach

A complete research objective of this thesis is to gain a better understanding of boundary layer transition on a complex geometry in hypersonic flow by challenging current tools and facility capabilities.

The approach taken was to identify transition instabilities and mechanisms both on and off the surface of the BOLT geometry at hypersonic speeds through ground test and simulation. On-surface measurements of the geometry will be compared between Texas A&M University, Purdue University, NASA Langley Research Center, and CUBRC hypersonic wind tunnel facilities. The freestream environment within each facility ranges

from conventional to quiet (flight-like) to high-enthalpy flow. Measurements on the surface include surface pressure fluctuations measured by PCBs and Kulites as well as the surface heat flux viewed by infrared thermography and TSP and measured directly with Schmidt Boelter gauges. The heat flux results from the quiet wind tunnel facilities were compared with computations performed by the University of Minnesota. Measurements off the surface of a 33% scale BOLT model in the M6QT were acquired through constant temperature hot-wire anemometry within a vortical mode. Off-body measurements were compared with sparsity-promoting dynamic mode decomposition (SPDMD) simulations from the University of Minnesota.

1.3 Thesis Structure

The current work presented in this thesis involves a collaboration between universities, industry, and the government. The data provided for this thesis contributed to a greater understanding of boundary layer transition in hypersonic wind tunnel facilities and computational fluid dynamics (CFD). The present work for this thesis is structured in a way with Chapter 1 providing a background and motivation for boundary layer transition at hypersonic speeds with the current objectives for the project. Chapter 2 provides an introduction to the geometry and wind tunnel models, background of all facilities, and diagnostic techniques discussed in this paper as well as uncertainty. Results are reported in Chapter 3 for surface heating, surface pressure spectra, and hot-wire anemometry measurements for the BOLT geometry. Chapter 4 leads into the conclusions and discussion of the current research as well as recommendations. Complete wind tunnel campaign logs at TAMU are located in Appendix A and B. All IR thermography results

for conventional and quiet flow at TAMU are located in Appendix C and D. All surface pressure spectra results for conventional and quiet flow are located in Appendix E and F. Finally, Appendix G contains previous blockage model IR results at TAMU.

2. EXPERIMENTAL METHODS

2.1 Wind Tunnel Models

The Boundary Layer Transition (BOLT) flight test geometry was designed by the Johns Hopkins University Applied Physics Laboratory (JHUAPL) [44]. Experimental wind tunnel testing of two 33% scale models, a 31% scale model, and a full-scale model will be discussed in this thesis. JHUAPL designed and fabricated a 33% scale model that was tested at Texas A&M University, Purdue University, and NASA Langley Research Center. This 33% scale model will be referenced as the *JHUAPL* model. The machined model contains a single PEEK plastic surface for IR thermography viewing with the remaining assembly made of 6061 aluminum. The assembly is shown in Figure 2-1 with the dimensions included. The geometry features concave surfaces with highly swept leading edges.

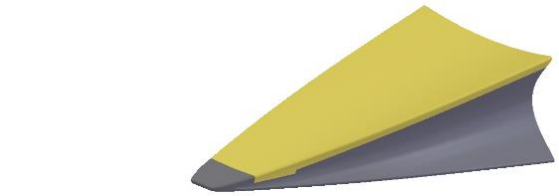

(a) IR viewing surface

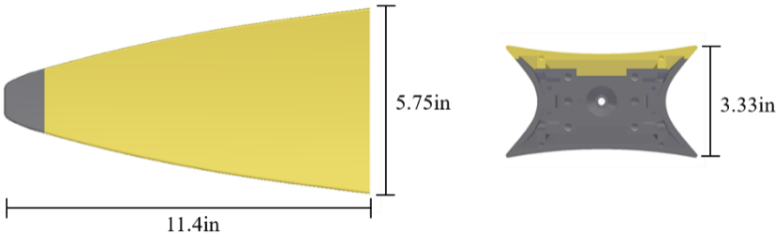

(b) Dimensions of BOLT

Figure 2-1. 33% scale BOLT geometry and assembly in SolidWorks (yellow - PEEK plastic, gray - 6061 aluminum); (a) is the IR viewing surface and (b) are the dimensions

Thermal conductivity, specific heat capacity, and density of the PEEK material are stated in Table 2-1. The values are based on the manufacturer's quote of the material and were provided to TAMU from JHUAPL. The properties are necessary for heat flux calculations from IR thermography for all facilities that are discussed in Chapter 3.

Table 2-1. PEEK property materials used for analysis for all IR results in this paper

Thermal Conductivity $\kappa \left(\frac{W}{m^2 \cdot K}\right)$	**Specific Heat Capacity** $c_p \left(\frac{J}{kg \cdot K}\right)$	**Density** $\rho \left(\frac{kg}{m^3}\right)$
0.290	1026	1300

An exploded view of the model, with the PEEK surface replaced with an experimental aluminum surface for roughness experiments [45], is shown in Figure 2-2. The assembly allows for easy access and placement of surface pressure transducers and heat flux gauges from below each surface. This thesis will not focus on the roughness experiments but the IR images from the roughness campaign are used for heat flux gauge comparisons.

JHUAPL provided TAMU with spare machined parts and CAD drawings to machine a duplicate of the 33% scale geometry. This geometry will be referenced as the *TAMU* model with the data. The manufacturing and design are similar to Figure 2-2, but the roughness cut-out located on the top surface is not present on the TAMU model. Off-body measurements were made on the TAMU model only due to a pure aluminum body with no surface pressure transducer ports. A 31% scale model was tested in the TAMU facilities at various Mach numbers that the vehicle will see in flight. The model was 3-D printed out of polycarbonate material using a Stratasys FDM 400mc printer with a layer thickness of 0.010 in. Thermal properties of the polycarbonate material that were used for

IR thermography processing are listed in Table 2-2. Images of all three subscale wind tunnel models are shown in Figure 2-3.

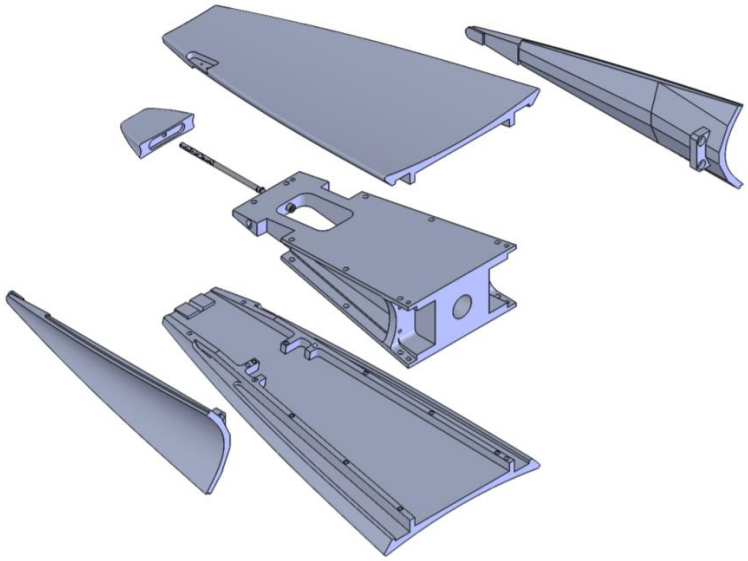

Figure 2-2. Exploded view of 33% scale BOLT model (reprinted from [45]).

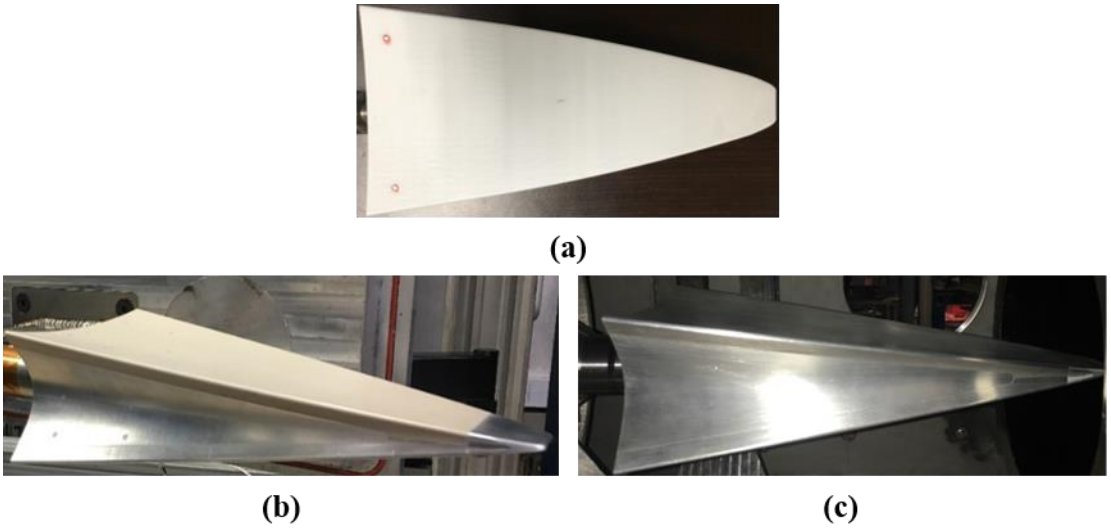

(a) **(b)** **(c)**

Figure 2-3. 31% and 33% scale BOLT wind tunnel models; (a) 31% scale (reprinted from [46]), (b) JHUAPL (reprinted from [47]), and (c) TAMU

Table 2-2. Polycarbonate material properties used for analysis in this paper

Thermal Conductivity $\kappa \left(\frac{W}{m^2 \cdot K}\right)$	**Specific Heat Capacity** $c_p \left(\frac{J}{kg \cdot K}\right)$	**Density** $\rho \left(\frac{kg}{m^3}\right)$
0.19	1200	1200

A flight-scale model of BOLT was tested at the Calspan-University of Buffalo Research Center (CUBRC). The length of the solid model is 0.865 m from the leading edge to the back of the geometry. The majority of the testing campaign at CUBRC consisted of roughness experiments, but those data will not be featured in this thesis. The top surface and gutter of the aluminum body were painted with temperature sensitive paint to view the surface heating on the model. An image of the full-scale model with Mike Holden as a reference for the size is shown in Figure 2-4.

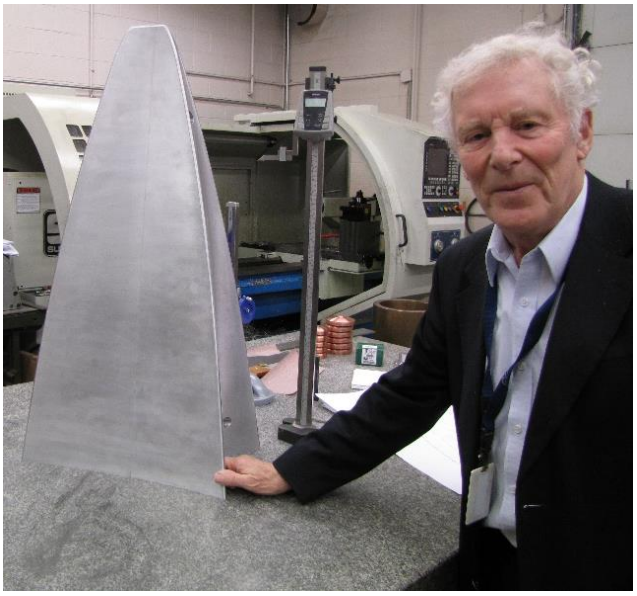

Figure 2-4. Flight-scale model of BOLT tested at CUBRC.

2.2 Facilities

2.2.1 Texas A&M University

Located at Texas A&M University is the National Aerothermochemistry and Hypersonics Laboratory. Two hypersonic blow-down wind tunnel facilities located within the lab and used extensively for this research are the NASA Langley Mach 6 Quiet Tunnel (M6QT) and the Actively Controlled Expansion (ACE) tunnel. Both wind tunnel facilities are supplied by the same infrastructure, so no two tunnels can run simultaneously. Two CompAir Reavell 5442 compressors provide high-pressure air stored in a 2500 pisa capacity tank. The compressed air is filtered of sub-micron contaminants and oil from the compressors and dried by desiccant driers to 233 K. A 2-inch pipe supplies air from the compressed tank to the laboratory with a 4-inch pipe supplying air to the ejector system. Once the air from the 2-inch line reaches the laboratory, it is heated by a 0.5 MW Chromalox heater, sent through a one-micron particle filter, and passed into the tunnel. The tunnel is preheated to a stagnation temperature of 430 K with low-speed (around 35 psi – 55 psi depending on the facility) air to prevent liquefaction within the tunnel. The JHUAPL and 31% 3-D printed model were inserted into the tunnel after preheat, whereas the TAMU model was present. A two-stage Venturi air-ejector system, located outside the building, pulls the vacuum for both facilities which uses the majority of the air supplied by the compressed tank. The Fox brand ejectors can supply a vacuum of 530 kPa with 25 kg/s of compressed air at 1 MPa. A typical run for the present experiments lasts approximately 40 seconds. More information on tunnel infrastructure is well documented in dissertations from previous colleagues [32, 48].

2.2.1.1 The NASA Langley Mach 6 Quiet Tunnel (M6QT)

The M6QT, originally located at NASA Langley Research Center, is currently located at the National Aerothermochemistry and Hypersonics Laboratory (NAL) at Texas A&M University. The previous design of the tunnel was to maximize the existence of a laminar boundary layer off the nozzle walls, thereby producing stability and transition measurements in an environment closely resembling that of flight. Upon reestablishing the M6QT at Texas A&M in 2005, the performance within the tunnel was brought back to its quiet conditions [49] consistent with its past environment at NASA [50]. Located within the first half of the settling chamber are a series of meshes and screens to help dampen and reduce the noise of the incoming flow into the nozzle. At the nozzle throat is a bleed valve system that when engaged produces a new laminar boundary layer on the nozzle wall, therefore minimizing disturbances within the testing environment. The slow-expanding, axisymmetric nozzle is highly polished with a length of 1 m, a throat diameter of 1 in, and an exit diameter of 7.5 in. The nozzle was formed by electroforming nickel onto a stainless-steel mandrel that was later plated with a nickel-phosphorus alloy. The contour was designed to minimize nozzle wall curvature and delay the growth of Görtler vortices off the wall [49, 51]. The infrastructure of the facility is shown in Figure 2-5 [52]. For the present experiments, the tunnel operated in the range of Re/m = $7x10^6$ – $11x10^6$.

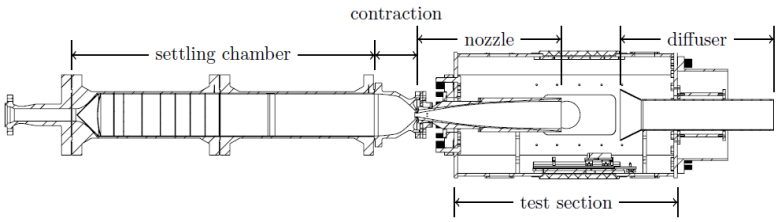

Figure 2-5. Texas A&M University Mach 6 Quiet Tunnel schematic (reprinted from [52]).

Creating a ‘quiet’ environment is critical and challenging for wind tunnel design. A “double cone” diagram of the quiet test core environment is given in Figure 2-6, where the upstream cone is bounded by the uniform flow at the exit Mach number and the downstream cone is bounded by the pressure disturbances radiating off the turbulent nozzle wall at the Mach angle [49]. Having as much of the model in the quiet test core creates a low-disturbance flow over the model. With a change in Reynolds number, the quiet core shifts upstream or downstream within the nozzle. A representation of this effect from Pitot pressure fluctuations measured with a Kulite dynamic pressure sensor in the facility on a flared cone [53] is shown in Figure 2-7. The color bar represents the freestream noise measured within the facility, where the dark blue region is the field of least disturbances denoted as the ‘quiet core’. A more detailed discussion of the existence and concept of the quiet core is given by Hofferth [49, 53, 54].

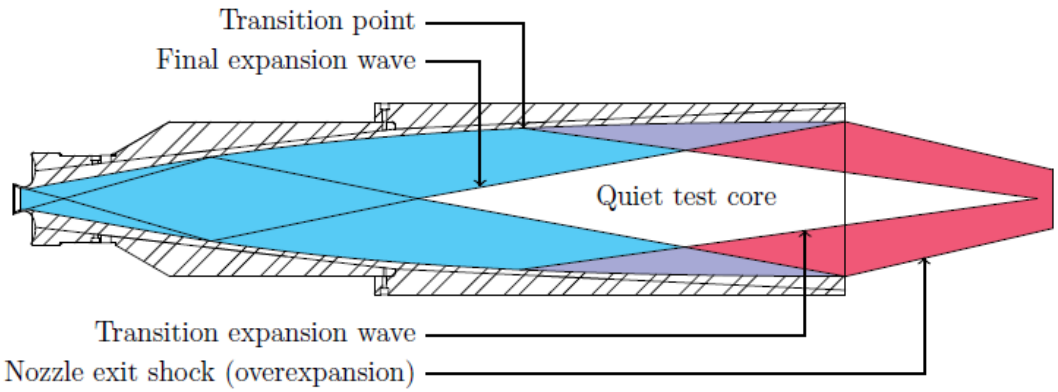

Figure 2-6. Mach 6 Quiet Tunnel nozzle with the location of the quiet test core in the facility (reprinted from [52]).

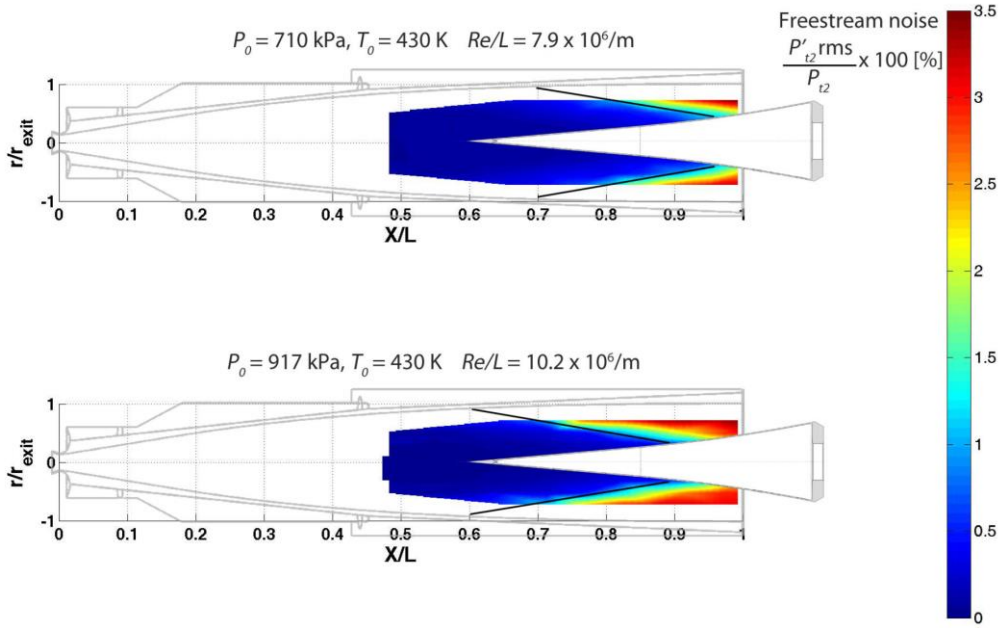

Figure 2-7. Contours of normalized freestream RMS Pitot pressure around a flared cone. Freestream conditions are Re/m = 7.9×10^6 (top) and Re/m = 10.2×10^6 (bottom) (reprinted from [53]).

The BOLT model was pushed as far upstream into the quiet core as capable in Figure 2-8. The minimum amount able to protrude past the nozzle exit while avoiding the shock off the model leading edge as well as the nozzle exit shock was 2.54 cm. This placement was kept for each run of both 33% scale models for direct comparison. Optical access was accessible by viewing the PEEK surface with the IR camera positioned at the top of the M6QT. Upon investigating the IR imagery results, elevated heating is seen on the outer portion of the JHUAPL model from noise interference. This effect will be seen in the results in Chapter 3.

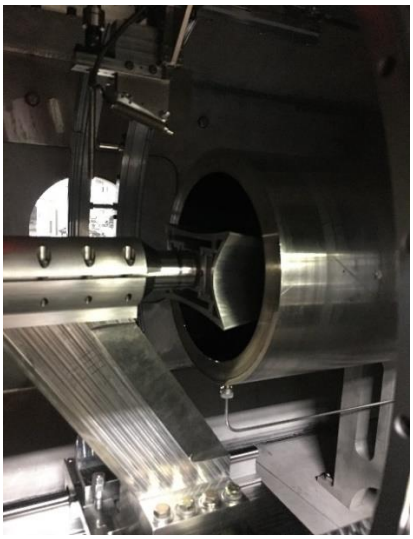

Figure 2-8. Placement of the TAMU BOLT model within the M6QT test section (reprinted from [47]).

2.2.1.2 The Actively Controlled Expansion (ACE) Tunnel

ACE is a conventional, variable Mach number wind tunnel facility that contains a higher percentage of freestream disturbances within the flow. The Mach number within the facility is varied by manually adjusting the height of the nozzle throat. For the current study, three Mach numbers were tested: 5.4, 6, and 7.4. The settling chamber contains two aerogrids and three mesh screens to help make the incoming flow more uniform. The cross-sectional area of the test section is 0.23 m x 0.36 m with a length of 0.69 m. A diagram of the ACE facility is shown in Figure 2-9. More detailed schematics of the ACE facility as well as the new diffuser design and installation are available in various sources [48, 55-57].

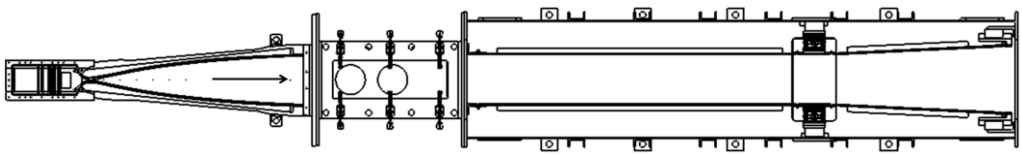

Figure 2-9. Diagram of the ACE wind tunnel facility at TAMU (reprinted from [48]).

The freestream environment within ACE has been well-documented over the years [13, 32, 57] for various Reynolds and Mach numbers. At Re/m = $3x10^6$, the nozzle walls of ACE transition and a higher amount of freestream disturbances are present in the flow due to noise radiating off the nozzle sidewalls. An excellent graph that portrays the difference in the freestream disturbance environment relative to the Mach number and Reynolds number in ACE, the M6QT, and the Purdue BAM6QT is shown in Figure 2-10 [32].

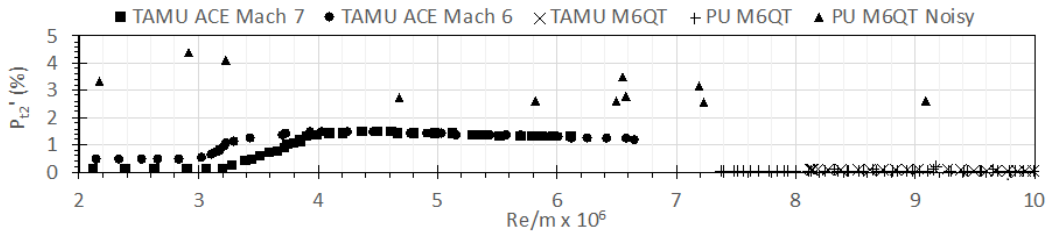

Figure 2-10. Freestream disturbance environment comparison between the M6QT, BAM6QT, and ACE (reprinted from [32]).

The *y*-axis represents the freestream Pitot pressure fluctuations within the designated facilities and the *x*-axis is in Reynolds number per meter (Re/m). As the Mach number increases within ACE, the acoustic freestream disturbance levels are less effective than at the lower Mach numbers. However, at Re/m = $3x10^6$, the freestream disturbances begin to dominate within the flow, showing a sudden increase in the curves. Comparing these results to the M6QT and the BAM6QT, very low disturbances are seen in quiet flow. When the BAM6QT is run with bleed valves closed (noisy), higher freestream fluctuations are present than those in ACE. A side view of the JHUAPL BOLT model within ACE is shown in Figure 2-11 where flow is from left to right. The IR camera is also seen mounted above the tunnel on a cage constructed of XT-95 optical railing. The position of the camera

is ideal for looking straight through a Zinc selenide (ZnSe) window onto the PEEK surface of the model.

Figure 2-11. BOLT located in the Actively Controlled Expansion tunnel (reprinted from [47]).

2.2.2 Purdue University

Located at Purdue University, the Boeing/AFOSR Mach 6 Quiet Tunnel (BAM6QT) is a low-disturbance facility featuring a Ludwieg tube design producing hypersonic flow. The BAM6QT contains a similar bleed valve system as Texas A&M to produce quiet or conventional flow within the facility. The highly-polished nozzle is elongated to minimize the Görtler instability. The wind tunnel design is capable of producing freestream noise levels as low as 0.01% when ran as quiet but can produce noise levels near 3%, previously seen in Figure 2-10, when operated as a conventional hypersonic facility [58]. A schematic of the facility is given in Figure 2-12 where the design incorporates a long driver tube followed by a converging-diverging nozzle ending with a large dump tank. The facility utilizes two aluminum diaphragms with pressure located between them, which is half that of the pressurized region within the tunnel [59].

When the diaphragms burst, an expansion wave travels upstream through the nozzle and a shock wave propagates downstream. The expansion wave continues to reflect back and forth within the tunnel, causing a quasi-drop in the total pressure [59] during a wind tunnel run. The run lasts approximately 5 seconds. Wind tunnel models are placed at the end of the diverging section of the nozzle where the change in the tunnel diameter is gradual. Models within the facility can be mounted at various angles of attack (AoA) and yaw, but the present study will focus on zero AoA and yaw experiments with the JHUAPL BOLT model. An image of the JHUAPL model right before closing of the BAM6QT is shown in Figure 2-13. The model is mounted such that the PEEK surface is towards the window for IR thermography. The other experimental surface (not visible) is painted with TSP.

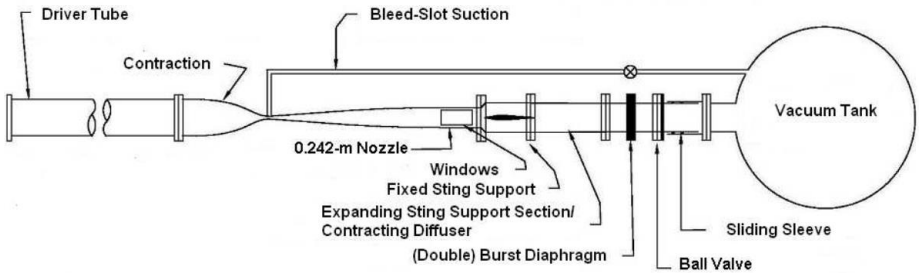

Figure 2-12. A schematic of the Boeing/AFOSR Mach 6 Quiet Tunnel located at Purdue University (reprinted from [59]).

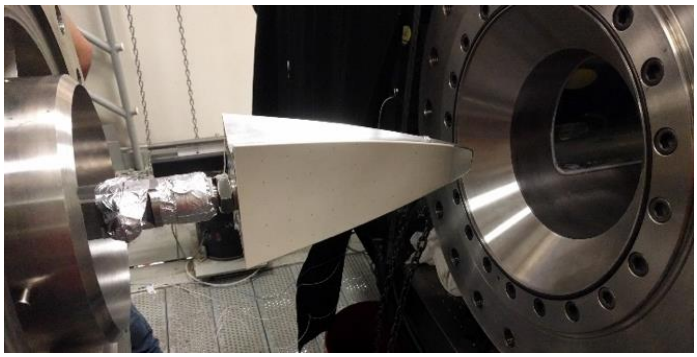

Figure 2-13. The BOLT model outside of the BAM6QT before placement in the facility; PEEK side shown (reprinted from [46]).

2.2.3 NASA Langley Research Center

The 20-inch Mach 6 Air Tunnel is a conventional hypersonic blow-down facility located at NASA Langley Research Center. The tunnel first became operational in the year 1958 with a basis for aerodynamic and aerothermodynamic testing. Air is supplied by a 4250 psi bottle field and a 600 psi bottle field that is preheated [60] and filtered. A layout of the facility is shown in Figure 2-14 with a more concise and detailed breakdown of the infrastructure given by Berger et al. 2015 [60].

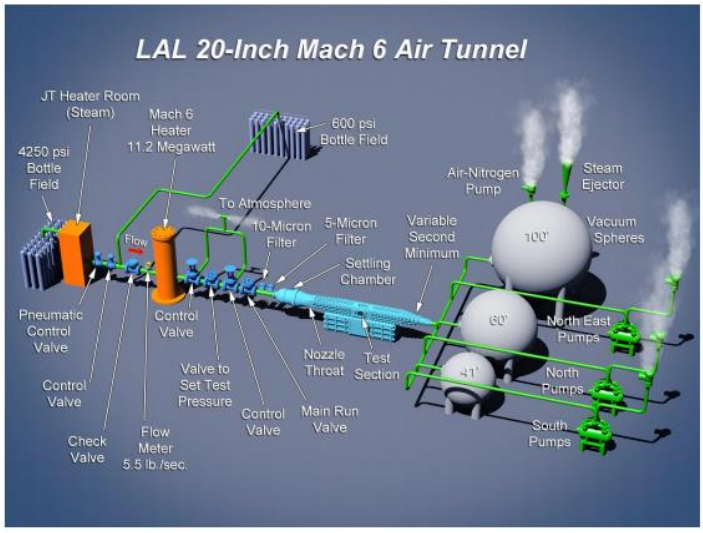

Figure 2-14. NASA Langley Research Center 20-Inch Mach 6 Air Tunnel schematic (reprinted from [60]).

The settling chamber is equipped with screens and a perforated conical baffle at the entrance. The 7.45 ft long nozzle is two-dimensional, where the top and bottom walls are contoured and the sides are parallel. The cross-sectional area of the test section is 20.5 in x 20 in. The facility incorporates a bottom-mounted injection system that transfers the wind tunnel model from the sheltered model box to the tunnel test section centerline in less than half a second when the tunnel is on condition. For the BOLT experiments, a run

time of a few seconds was only needed, but the facility can run well over 15 minutes. The Mach number is 5.8-6.1, with a unit Reynolds number (Re/m) range of $1.6x10^6$ to $27x10^6$. Zero AoA and yaw are discussed for the current analysis. A photograph from a roughness experiment of the JHUAPL wind tunnel model before placement into the tunnel is shown in Figure 2-15. The tunnel has the capability of a full-field view for IR thermography through a ZnSe antireflective-coated window located at the top of the test section.

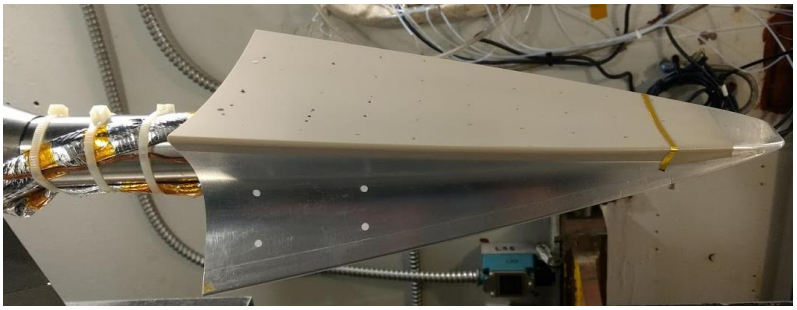

Figure 2-15. The BOLT model located in the shelter box in the 20-Inch Mach 6 Air Tunnel for a roughness experiment (reprinted from [46]).

2.2.4 Calspan-University of Buffalo Research Center (CUBRC)

The CUBRC LENS II facility is a hypervelocity reflected shock tunnel. The facility can run as either a shock tunnel or Ludwieg tube with fully duplicated flight conditions from Mach 3 to 9 and is shown on the right in Figure 2-16. The facility features long driver and driven tubes, around 60- and 100-ft in length, respectively, [61] with three different contoured nozzles to achieve the Mach number range previously mentioned. Test times range from 100-200 ms. Within the double-diaphragm unit, the test gas is pressurized which causes the diaphragms to burst. A shock wave then travels towards the driven tube, is reflected, and travels back upstream creating stagnant high-pressure and

temperature gas. The test gas travels through the nozzle, into the test section, and a valve quickly closes at the nozzle throat terminating the flow [61].

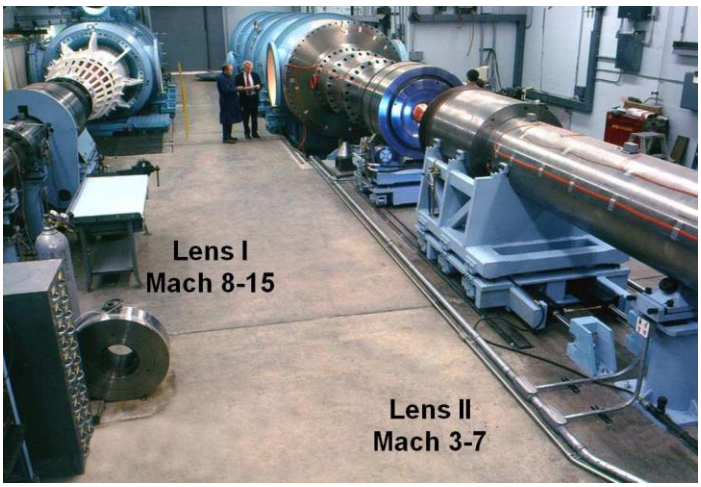

Figure 2-16. LENS I and LENS II facilities located at CUBRC (reprinted from [61]).

For the current BOLT experiments, the facility ran as a shock tube within the Woomera trajectory Mach numbers and Reynolds numbers with a run time of 100 ms. The full-scale aluminum blockage model in the LENS II facility is shown in Figure 2-17. Due to the high-enthalpy environment within the tunnel and model material, TSP was used to view the heating on the surface. The TSP is represented as the yellow color painted on the aluminum surface.

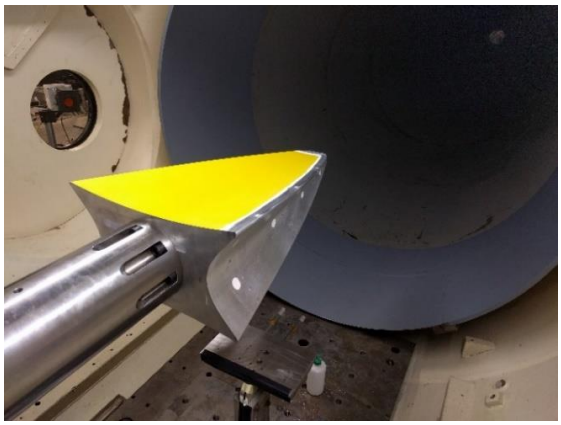

Figure 2-17. Full-scale model of the BOLT geometry in the CUBRC LENS II facility. Yellow surface represents TSP.

2.3 Instrumentation

2.3.1 IR Thermography

Infrared thermography was used by Texas A&M University, Purdue University, and NASA Langley to view the global surface temperature on the PEEK surface of BOLT. The sensitivity of IR thermography allowed for the identification of boundary layer flow structures (such as stationary crossflow instability vortices) and transition; e.g., see Figure 1-4 and Figure 1-5. Each facility used different mounting techniques, software, and cameras when viewing the surface. Table 2-3 lists each IR camera and corresponding characteristics used by each facility to produce temperature maps of the surface of BOLT.

Table 2-3. IR thermography camera characteristics for each facility

Type	Texas A&M	Purdue	Langley
Camera	FLIR SC8100	Xenics Onca MWIR-640	FLIR SC6701
Resolution (pixels)	1024 x 1024	640 x 512	640 x 512
Wavelength sensitivity (μm)	3-5	3.7-4.8	3-5
Raw output	14-bit	14-bit	14-bit

Calibration of each camera was achieved separately by each facility. At Texas A&M, a thermocouple was embedded in a black aluminum calibration plate that was

gradually heated and observed by the FLIR SC8100. The process and method is heavily documented by Dr. Andrew Leidy in his dissertation [48]. NASA Langley incorporated a bench-top calibration method using a Mikron M310 black-body source. The raw temperature IR images produced from each facility were calibrated and processed at Texas A&M for the current data analysis.

The Texas A&M NAL 1-D heat transfer data reduction code for converting the temperature maps of the IR images into heat flux was developed by Dr. Ian Neel at Texas A&M [22] but modified for configurations of BOLT [46]. The MATLAB code was initially inspired by the FORTRAN code QCALC [62] and configured for a more modern approach for HIFiRE studies [14, 27]. All experimental IR data presented in this thesis were processed using this code. The code involves a forward time central difference scheme shown in Equation 2.1 for solving the heat conduction equation.

$$\frac{\partial T}{\partial t} = \alpha \frac{\partial^2 T}{\partial x^2} \sim \frac{T_i^{n+1} - T_i^n}{\Delta t} = \alpha \frac{\left(T_{i+1}^n - 2T_i^n + T_{i-1}^n\right)}{\Delta x^2} \tag{2.1}$$

The thermal diffusivity, α in Equation 2.1, is defined in Equation 2.2:

$$\alpha = \frac{\kappa}{\rho c_p} \tag{2.2}$$

The material properties in Equation 2.2 were previously mentioned in Table 2-1 for PEEK provided by JHUAPL. The heat flux is then calculated using a second order approximation of the first spatial derivative using Equation 2.3:

$$q(n) = \frac{-k\left(-\frac{3}{2}T_0^n + 2T_1^n - \frac{1}{2}T_2^n\right)}{\Delta x} \tag{2.3}$$

Where *n* is the time coordinate and *i* is spatial. Two boundary conditions are implemented: a surface condition which is the time dependent surface temperature from the IR camera

and a depth condition which is assumed constant within the defined depth of the model material. Due to the low thermal conductivity of PEEK, the 1-D analysis performed is deemed appropriate. The comparisons with CFD provide some support of this assumption. A more detailed explanation of the code and process during a tunnel run is provided by Neel 2019 [32].

Since each facility has different run conditions, i.e. settling chamber temperature, converting the heat flux data into Stanton number using Equation 2.4 were more appropriate. The subscript ∞ denotes freestream conditions, *0* is the stagnation properties, and *w* is the wall properties. These results will be shown in Chapter 3.

$$St = \frac{q}{\rho_\infty U_\infty c_p (T_0 - T_w)} \tag{2.4}$$

2.3.2 Temperature Sensitive Paint (TSP)

Temperature sensitive paint (TSP) is a luminescent paint mixture that enables surface temperature measurements through thermal quenching. TSPs are coatings that involve a carrier, binder, and photo luminescent probes [63]. Incoming light collides with the luminescent molecules within the paint and forces an electron into an excited state. The electron then returns to its ground state and releases a photon with decreased intensity. The mechanism is dependent on temperature, thus changes in temperature on the surface can be determined from a charged-couple device (CCD). Both Purdue and CUBRC acquired TSP images. The process of TSP is heavily documented by Hubner et al. 2002 for high speed flows [63] in the LENS I facility at CUBRC. The process is assumed the same for the LENS II facility.

At Purdue University, TSP data were acquired simultaneously with IR thermography. Shown in Figure 2-18 is a photo of the aluminum surface on the JHUAPL BOLT wind tunnel model painted with TSP. To maximize the excitation of the molecules, two arrays of light-emitting-diodes (LED) were used. An Innovative Scientific Solutions Inc. (ISSI) LMA LM4 array and an LM2xLZ-465 array were used to illuminate the model. Images of the surface were recorded on an IMPERX Bobcat IGV-B1620 14-bit CCD camera. When converting the intensity values from the CCD to temperature maps, three sets of images are recorded per run: a 'dark' image, an 'off' image', and an 'on' image. The change in temperature is a function of the ratio of intensity values from these images. Liu states the empirical process for correlating these images [64]. Fourier's law of heat conduction is simplified by assuming one-dimensional heat transfer. These data are then calibrated to a Schmidt-Boelter Gauge located on the model surface. All TSP images were imaged and processed at Purdue.

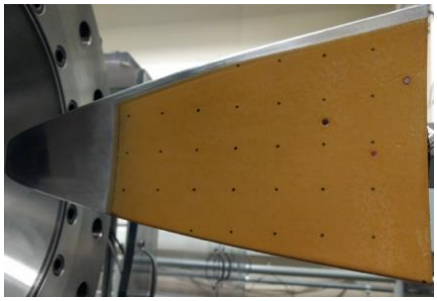

Figure 2-18. TSP painted on the aluminum surface of the JHUAPL model at Purdue (reprinted from [46]).

2.3.3 Surface Mounted Pressure Transducers

Each facility instrumented BOLT with surface mounted pressure transducers to help identify transition mechanisms. High frequency pressure measurements were

achieved using both Kulite and PCB pressure sensors. Kulite XCE-062-15A were used in each facility and have been characterized under a supersonic turbulent boundary layer [65]. The transducer is expected to have a linear frequency response up to 30% to 40% of its resonant frequency [65], which corresponds to about 0 – 100 kHz. The Piezotronics PCB 132B38 model were used extensively in this campaign. The PCBs were powered by manufacturer in-line signal conditioners. Measurements in the hundreds of kilohertz are necessary due to the known frequency range of the second mode and potential secondary instabilities. PCBs have proven reliable for frequencies between 50 kHz and 1 MHz. A summary of the pressure fluctuation methods for each facility with the corresponding filtering of sensors is given in Table 2-4.

At Texas A&M, data were acquired by an in-house LabVIEW VI with two National Instruments USB-6366 (16-bit) DAQ systems. The PCBs are high-passed filtered by built-in electronics with a 2 dB cutoff at 11 kHz. The Kulite signal conditioning box was built in-house by Dr. Jerrod Hofferth, with a circuit design modified by the one previously developed by S.P. Schneider research group at Purdue University [54]. The box provides a DC and AC signal output for each sensor, where the DC output is gained by 100 and low-passed filtered with a first-order RC circuit at 482.5 kHz. The AC-coupled content were high-pass filtered at 842 Hz with a gain of 28.9. The AC-coupled PCB data signals were low-passed at either 500 kHz or 1 MHz. The author found no difference in the data with either of these two filters. Kulite data signals were low-pass filtered at 200 kHz. Both PCBs and Kulites utilized 8-pole Bessel filters of unity gain for anti-aliasing. The filtering units were located within a 2-channel Khron-Hite FMB3002 chassis.

At Purdue University, data were acquired through a Tektronix TDS7104 oscilloscope using High-Res mode. Data were sampled at 2-5 MHz to satisfy the Nyquist criteria for resolving pressure fluctuations up to 1 MHz. NASA Langley acquired data using PXIe-6358/6124 National Instruments DAQ systems with precision filters.

Table 2-4. Type of sensor and filtering characteristics for each wind tunnel facility

Type	TAMU	Purdue	Langley
PCB Sampling	2 MHz	2 – 5 MHz	2.5 MHz
PCB Low-pass	500 kHz or 1 MHz	None	1 MHz
PCB High-pass	11 kHz	11 kHz	11 kHz
Kulite Sampling	2 MHz	1.25 MHz	200 kHz
Kulite Low-pass	200 kHz	None	80 kHz
Kulite High-pass	842 Hz	840 Hz	100 Hz

The PCB and Kulite sensors were adhered into the wind tunnel models using the PCB manufacturers preferred method of nail polish which has a higher pressure sensitivity than RTV and Neoprene [66]. NASA Langley added RTV to the back of the sensor to limit movement. The sensor top surface was mounted flush with the PEEK surface. With a limited quantity of PCB and Kulite sensors available at Texas A&M, various sensor configurations were tested. The unused ports were plugged using Teflon rod stock.

Power spectral density (PSD) plots of the spectra measurements at Texas A&M and Purdue were computed using Welch's method, where a Hamming window of size 2^{10} was used with a 50% overlap. NASA Langley also used Welch's method, where the Hamming window size for the PCBs and Kulites were 2^{10} and 2^{8}, respectively, both with a 50% overlap. The author has found the different window size techniques (Hanning vs. Hamming) made little to no difference in the final results.

The sensor locations were strategically placed based on the structures observed in the IR and TSP data [45] and are shown in Figure 2-19. Table 2-5 lists the location of each sensor located on BOLT. A limited number of sensors were available at Texas A&M. Therefore, Appendix A and B lists the configuration of sensors per each wind tunnel run. NASA Langley and Purdue ran all sensors simultaneously.

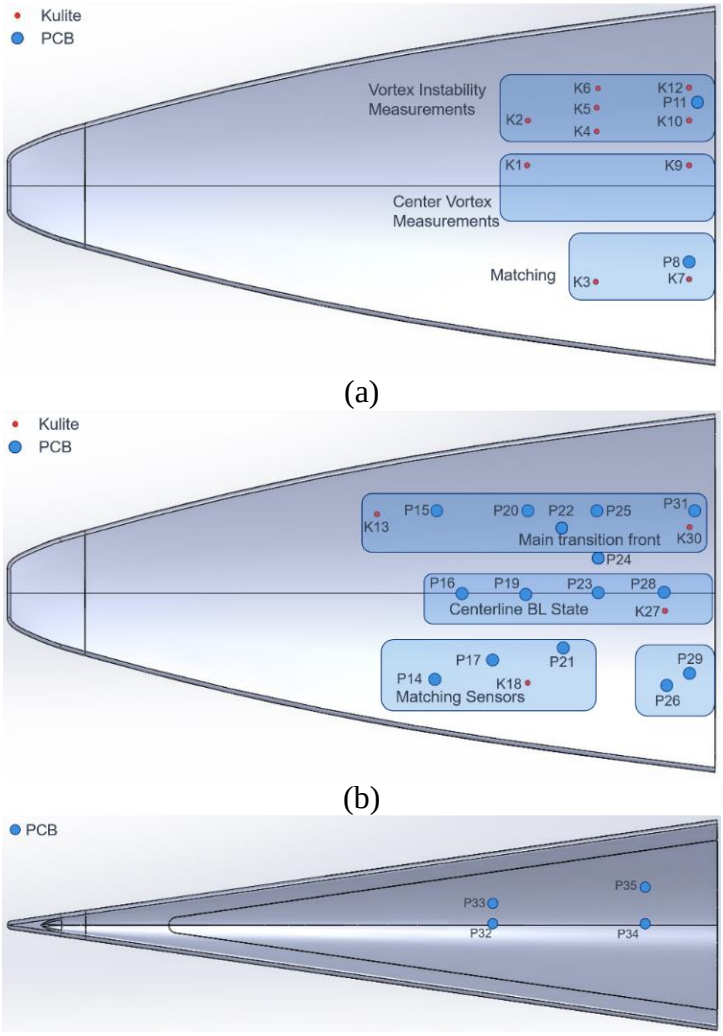

Figure 2-19. Sensor layout on the surfaces of BOLT; (a) is the layout on the PEEK surface, (b) is the layout on the aluminum surface, and (c) is the layout on one of the gutter surfaces. The rectangular-shaped boxes represent measurement regions of interest from JHUAPL.

Table 2-5. Location of sensors on the 33% scale BOLT model.

Sensor	x-location from back of BOLT (inches)	z-location (inches)
K1	3.000	0.250
K2	3.000	1.000
K3	2.000	-1.500
K4	2.000	0.900
K5	2.000	1.250
K6	2.000	1.500
K7	0.500	-1.500
P8	0.375	-1.273
K9	0.500	0.250
K10	0.500	1.000
P11	0.375	1.273
K12	0.500	1.500
K13	5.500	1.200
P14	4.500	1.250
P15	4.500	1.250
P16	4.000	0.000
P17	3.500	-1.000
K18	3.000	-1.500
P19	3.000	0.000
P20	3.000	1.250
P21	2.500	-1.000
P22	2.500	1.000
P23	2.000	0.000
P24	2.000	0.500
P25	2.000	1.250
P26	1.000	-1.500
K27	1.000	-0.250
P28	1.000	0.000
P29	0.375	-1.273
K30	0.500	1.000
P31	0.375	1.250
P32	3.000	0.000
P33	3.000	0.680
P34	1.000	0.000
P35	1.000	0.880

2.3.4 Surface Mounted Heat Flux Gauges

Schmidt Boelter gauges were mounted in specific locations at NASA Langley to provide a direct measurement of heat flux for comparison to the IR results. The sensors used were Medtherm Corporation 8-2-0.25-48-20835TBS models lent to Langley from Purdue. The sensor contains an array of Type-T thermocouples (thermopile), which forms

a differential thermoelectric circuit that can be used for both body and surface measurements. The diameter of the sensor is 0.125 inches, the same diameter as a PCB, and was mounted flush with the surface through the same procedure as a PCB. The analog output voltage was acquired directly into a NEFF System 620 DAQ system. Low pass filters and amplifiers contained within the NEFF System were used for signal processing. The author of this thesis was provided with the already processed Schmidt Boelter gauge data. The location of the sensor used in this study is circled in yellow in Figure 2-20.

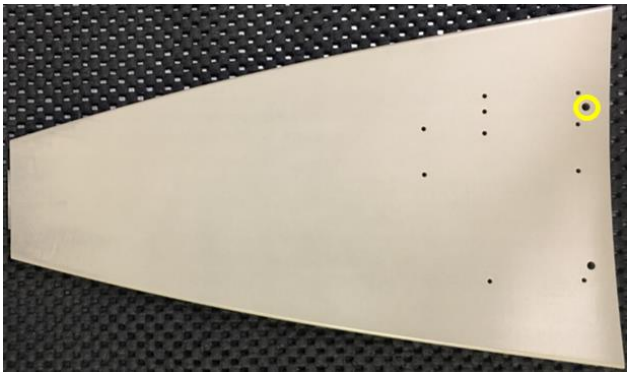

Figure 2-20. Location of the Schmidt Boelter gauge in the PEEK surface for analysis.

2.3.5 Hot-wire Anemometry

TSI high temperature probes (1220-PI2.5 and 1220-PI5) with slack were used to quantify off-body instability modes for frequencies less than 100 kHz. Hot-wires respond to changes in mass flux and total temperature [48]. The sensor temperature loading factor was set to $\tau = 0.8$ to minimize total temperature sensitivity. An A.A. Lab Systems AN-1003 constant temperature anemometer was employed to power the sensor. The wire was tuned during a wind tunnel run by adjusting the damping and ferric screws located on the AN-1003 system. The response was monitored in NI SignalExpress Project

simultaneously using a PCI-5122 digitizer/oscilloscope card. The AN-1003 unit balances the bridge that contains a feedback loop for maintaining the set resistance of the wire. The schematics of the sensor are shown in Figure 2-21, along with a photograph of the anemometer system. The sensors were not calibrated for the present study as the interest was frequency content. All hot-wire traverse runs were at a set Reynolds number of $9.9x10^6$/m for comparison with DNS results from the University of Minnesota. The hot-wire signal processing parameters are listed in Table 2-6. The designation of A or B in the table for the first 1220-PI2.5 probe listed is a replacement of probe A to probe B during the campaign due to wire breakage. The designation of C for an additional 1220-PI2.5 is a new wire installed for a different campaign. The frequency response after tuning each probe with respect to the 3-dB roll-off is also listed in Table 2-6.

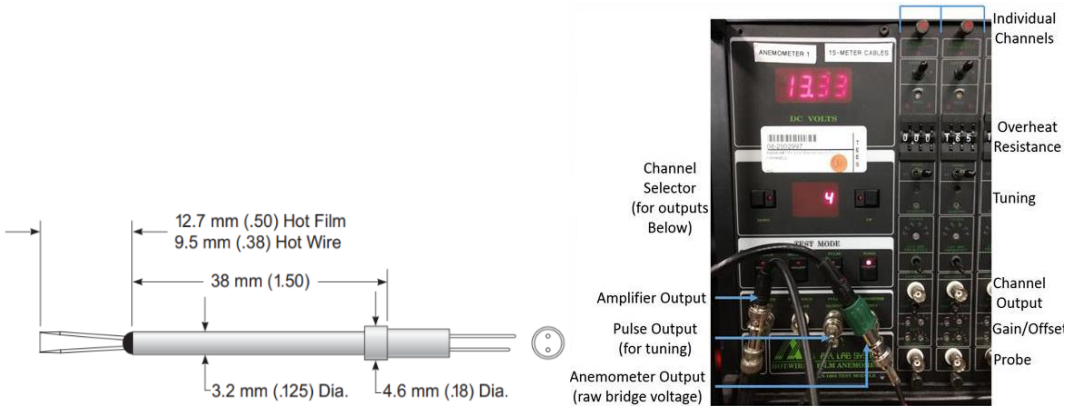

Figure 2-21. Model 1220 high-temperature straight probe (left) (reprinted from [47]) and A.A. Lab Systems interface (right) (reprinted from [48]).

Table 2-6. Hot-wire parameters for processing

Name	Diameter of Sensing Area (micrometer)	Frequency Response (kHz)	Sample rate (kHz)	High-pass (kHz)	Low-pass (kHz)
1220-PI2.5 (A & B)	6.3	130	500	1	200
1220-PI5	12.7	100	500	1	200
1220-PI2.5 (C)	6.3	160	500	1	200

Within the test section of the Mach 6 Quiet Tunnel, a three-axis traverse was previously designed and built by Stuart Craig for capability of studying three-dimensional phenomena [52]. The traverse moves in cylindrical coordinates: z (axial), r (radial), and Θ (azimuthal). The complete design characteristics of it are described in [52]. The traverse aids in quantifying effects over the surface of models through off-body measurements. Figure 2-22 is the traverse mechanism [52] with the BOLT 33% scale model installed. Two-dimensional planar data (maps) were acquired at a single streamwise location at x = 0.24 m. Results will be discussed in Chapter 3.

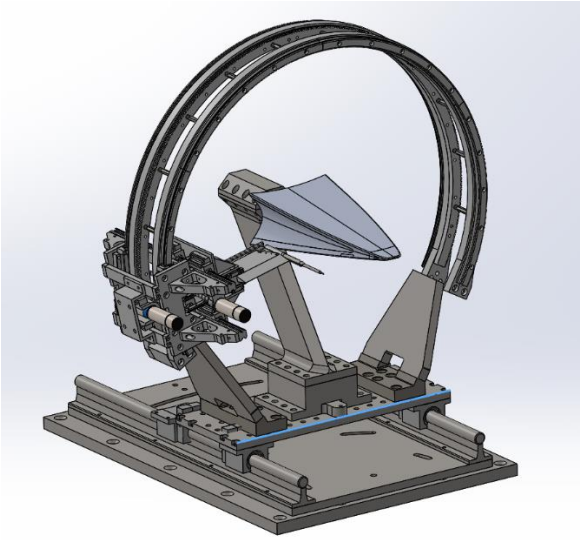

Figure 2-22. Three-dimensional traversing mechanism in the M6QT; 33% scale BOLT model mounted (the location of the hot-wire in the image is for visualization only) (reprinted from [47]).

To protect the sensor from abnormal flow in the beginning and the shock from tunnel unstart at the end, the hot-wire was hidden behind the nozzle exit during preheat, before tunnel startup, and before tunnel shutdown. Once the tunnel is on condition, the wire moves to the first measured point as per hard-coded in LabVIEW and continues with

its path before stepping back behind the nozzle. The number of steps/traverses depended on the time available for a complete wind tunnel run.

2.4 Uncertainty Estimates

2.4.1 TAMU Freestream environment

Tunnel freestream conditions for both TAMU facilities are computed using the settling chamber total pressure and temperature and the nozzle wall static pressure. The total pressure in ACE is measured using an Endevco 8540-200 pressure transducer with a factory uncertainty stated of 2.4%. The uncertainty is based on temperature, hysteresis, repeatability, and non-linearity. The total pressure in the M6QT is measured with an MKS Baratron 615A capacitance manometer with an uncertainty of ±0.12% of its measured value. The static pressure of ACE is measured by a Baratron 631C-10 with a manufacturer uncertainty listed of 0.5%. The M6QT static pressure is measured by an MKS 902 vacuum transducer with an uncertainty of ±1% of the reading. The Mach number and Reynolds number are calculated from these measurement quantities. At a Re/m = 9.9×10^6 in the quiet tunnel, the total pressure, total temperature, and Mach number standard deviation are ±0.8%, ±0.5%, and ±0.6%, respectively. At a Re/m = 5×10^6 in ACE, the total pressure, total temperature, and Mach number standard deviation are ±1.35%, ±0.57, and ±0.13%, respectively.

2.4.2 Instrumentation

The uncertainty in the IR thermography involves the properties of the PEEK material, emissivity, camera angle, temperature calibration, and processing assumptions. PEEK has a broad range of emissivity values causing large sources of uncertainty in the

analysis. The properties of PEEK used for the heat-transfer analysis were provided by JHUAPL. It has been shown that increasing the thermal diffusivity parameter within the 1-D heat conduction code by about 10% only increased the heat flux result by approximately 5% [48]. The initial temperature of BOLT within the M6QT is assumed to be the temperature of the model as it is assembled within the test section after preheating the tunnel to 430 K. A source of uncertainty is present for the long wind tunnel run times (up to 40 seconds) in ACE and the M6QT, where the thinner regions of the model may heat up to higher temperatures. A sensitivity analysis was done on varying the internal boundary condition for the 1-D heat conduction code in both ACE and the M6QT. A comparison was also made between the wing region (closer to nozzle sidewalls) and the centerline region of the model. The internal boundary condition was set to 295K (room temperature). With the assumption of a lower temperature within the interior of the model, the difference is larger in the M6QT than in ACE in Figure 2-23. The initial surface temperature of the model viewed by IR is between 303-310 K and 317-323 K in ACE and the M6QT, respectively, depending on the pixel location. In the M6QT, the model is sitting in an oven for approximately 10-15 minutes before the tunnel is turned on, therefore, it is safe to assume that the temperature within the interior of the model is the same as the temperature on the surface. In ACE, little variability is seen in Figure 2-23a. The model sits in the tunnel approximately 1-2 minutes before the tunnel starts. Thermocouples imbedded within the model would give a better approximation for the end-boundary condition. However, to better quantify the uncertainty of the IR code, experiments were performed at NASA Langley with a Schmidt Boelter heat flux gauge. Comparing the heat

transfer results from IR at NASA Langley to the Schmidt Boelter gauge at similar locations agreed to within 6%. These results will be shown in Chapter 3.

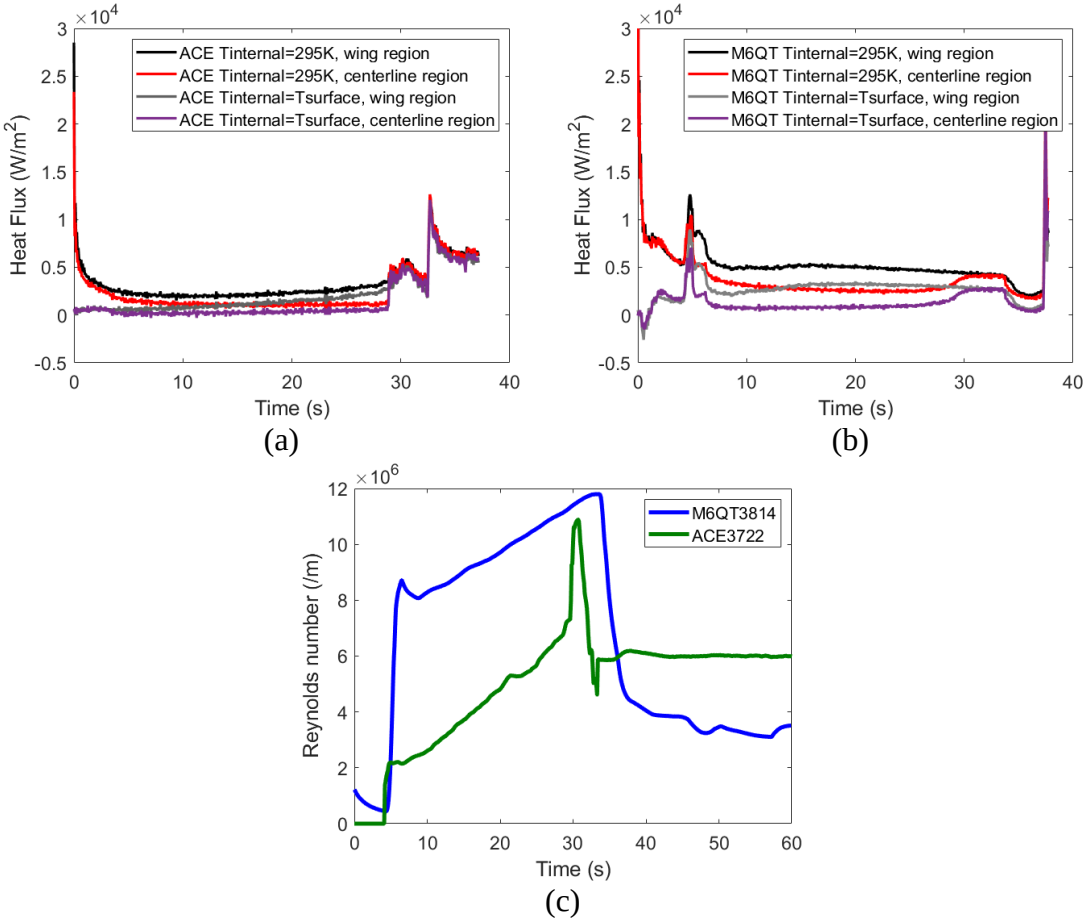

Figure 2-23. Heat conduction code sensitivity to initial boundary conditions. (a) ACE3722 results, (b) M6QT3814 results, and (c) Reynolds number

Kulite XCE-062-15A transducers have a factory stated uncertainty of ±0.1% of its 103.5 kPa range. The Kulites were calibrated at room temperature under vacuum and experience a ΔT of 50 K during a wind tunnel run. This results in a ±1% thermal zero and sensitivity shift. PCB 132B38 transducers were provided with a factory rated calibration and sensitivity uncertainty of ±30% of its 345 kPa range. These time of arrival sensors

utilized a single 50 psia test point for calibration. Various influences such as the sensing area, amplitude linearity, and structural strain cause uncertainty in the PCB measurements. Work is underway for quantifying these uncertainties in the PCB measurements by Piezotronics [66]. The PSD plots for both sensors were generated from 781 averages, which corresponds to an uncertainty of 3.6% for a PSD value.

The hot-wire results in this paper are un-calibrated, therefore, a large uncertainty is avoided in the results. Data were acquired at 500 kHz for 100 ms. The PSD plots were generated by 97 averages resulting in an uncertainty of 10.1% for each value. The location of the hot-wire within the M6QT test section is dependent on the three-axis traverse hardware explained more in-depth by Craig et al. 2015 [67]. The *r*-axis utilizes a Faulhaber 2232S024BX4 AES-4096 brushless DC motor with an absolute encoder. The *z*- and θ-axes contain a Faulhaber 2250S024BX4 AES-4096 motor with absolute encoders. The traverse was designed such that the *r*- and *z*- axes move with a resolution of 244 nm per encoder line with an accuracy of ±1220 nm. [67]. The θ-axes moves with an accuracy of $3°x10^{-5}$ per encoder line with an accuracy of $\pm 3°x10^{-4}$ [67].

3. RESULTS

3.1 Flow Visualization and Heat Transfer

Features on the surface of BOLT through wind tunnel testing were visualized through infrared thermography and temperature sensitive paint. A quiet DNS result of BOLT was computed by the University of Minnesota for Texas A&M M6QT conditions. Comparisons between the quiet DNS results and the quiet wind tunnel results will be made in this section as well as comparisons with the conventional wind tunnel results.

3.1.1 Quiet Tunnel Results with Comparison to DNS

IR thermography results from the Purdue BAM6QT for the 33% scale wind tunnel model are shown in Figure 3-1 at Re/m = 12.4×10^6 where flow is from left to right. The small circles located on the surface are surface pressure transducers. To break down the configuration, Figure 3-1.a is the measured temperature difference from the baseline temperature, meaning a background image before the tunnel starts is subtracted from the actual tunnel run image. The computed heat flux using Texas A&M's 1-D heat transfer code is presented in Figure 3-1.b with Stanton number (St) following in Figure 3-1.c. Streak-like structures are present on the model, similar to what was previously seen on the HIFiRE-5 model. IR results in the M6QT are shown in Figure 3-2 at Re/m = 10.2×10^6. Additional heating can be seen on the outer 'winged' region of the model, but the inner 60% of the model verifies the same pattern on the model at Purdue. Extra streaks can be seen on the surface of BOLT at Purdue, but this may be a result from the higher Reynolds number and/or slight model yaw. The outboard heating on the model in the TAMU facility

remains a discussion point, where transition effects off the nozzle walls previously seen in Figure 2-6 may have been a contributor. The high heat flux values at TAMU are a result of the outboard heating on the model. This effect is to not be confused as transition to turbulence.

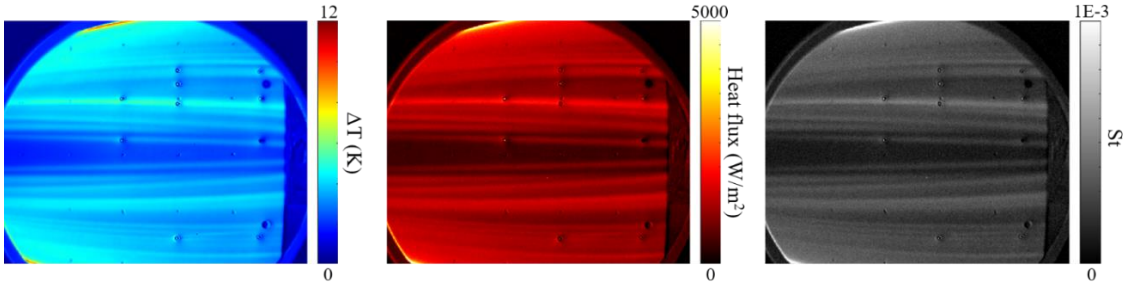

(a) ΔT → (b) heat flux → (c) St

Figure 3-1. Purdue BAM6QT results at Re/m = 12.4×10^6 with flow from left to right (reprinted from [46]). The back 6 inches of the model is shown with IR. (a) is the change in temperature, (b) is the calculated heat flux using Texas A&M's 1-D heat transfer code, and (c) is the conversion to Stanton number

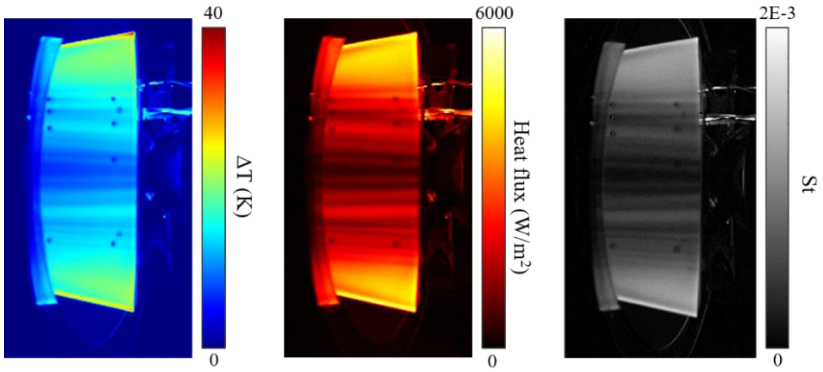

(a) ΔT → (b) heat flux → (c) St

Figure 3-2. TAMU M6QT results at Re/m = 10.2×10^6 with flow from left to right (reprinted from [46]). The back 2.5 in of the BOLT model is seen with IR. (a) is the change in temperature, (b) is the calculated heat flux using Texas A&M's 1-D heat transfer code, and (c) is the Stanton number

The TSP heat flux results imaged and processed at Purdue are shown in Figure 3-3 at Re/m = 10.2×10^6. The small dots seen on the surface are the registration marks located

1-inch apart. The two larger, more defined dots on the surface downstream on the model are the location of the Schmidt Boelter gauges used to calculate heat flux from the TSP. The less-defined dots scattered about the surface are due to reflections within the facility. Even with different Reynolds numbers and diagnostic techniques, the quiet tunnel results from Purdue show similar distinct structures. The same streaks, whether at a Reynolds per meter of 10.2×10^6 or 12.4×10^6, are visible in the TSP and IR, respectively. The inner 60% of the model in the M6QT at TAMU also compares with the Purdue results of both diagnostic techniques. No onset of transition to turbulence is seen in any of the quiet flow results.

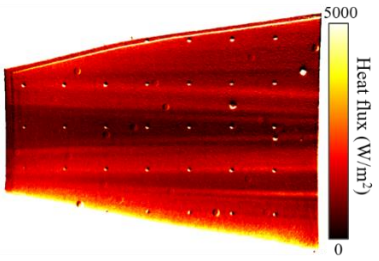

Figure 3-3. Temperature sensitive paint results on BOLT at Purdue University from a previous wind tunnel campaign of Re/m = 10.2×10^6 (reprinted from[46]). Color map is in heat flux.

University of Minnesota ran a quiet dynamic numerical simulation (QDNS) of a laminar CFD solution of BOLT at TAMU M6QT conditions for the case of Re/m = 10.2×10^6. The steady state CFD results are obtained using a low dissipation, 4th order kinetic energy consistent (KEC) numerical scheme for unstructured grids [68]. The wall is assumed to be isothermal at 300 K and is not altered to include any numerical roughness effects so as to maintain a 'smooth' wall. The computed solution is for half the domain due to the inherent symmetry and consists of approximately 160 million volume cells. For

more details see [38]. Texas A&M University computed a laminar basic state solution using the linear parabolized stability equations (LPSE) [39]. The solution is at the same conditions as Minnesota, including an isothermal wall. For more details on the analysis and computations, see [39]. Results from the laminar CFD solutions for the 33% scale BOLT model are shown in Figure 3-4. The results show complex surface flow topology with predominant streaks. A secondary flow pattern is established from the concave curvature with highly-swept leading-edges such that the flow is pushed inward toward the center of the model, an effect similar to what was seen on elliptic cones [20, 26]. The boundary layer upon the center region of BOLT is relatively large, but towards the leading-edge region it is fairly thin (see Figure 1-11). Thus, crossflow instabilities are a possibility in this region.

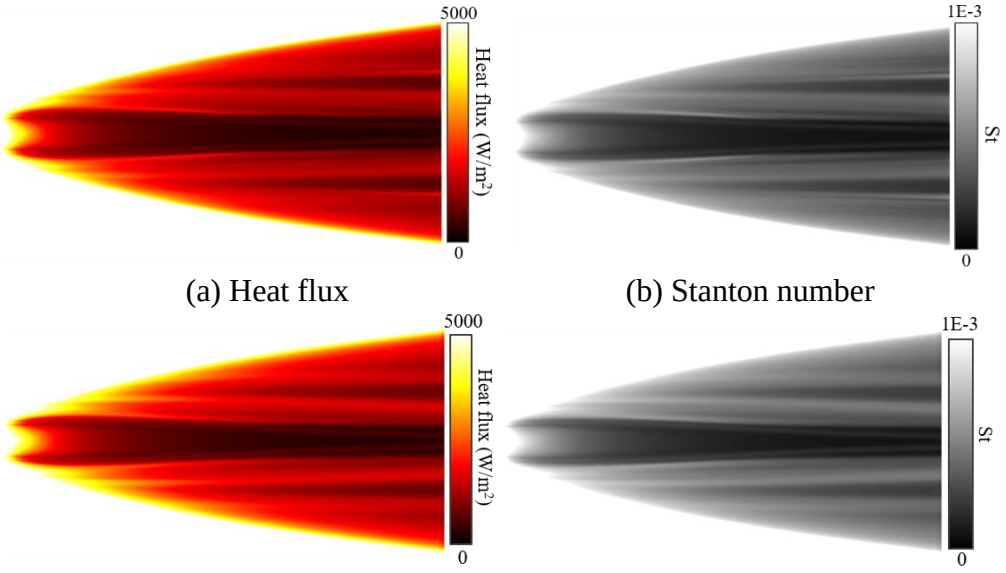

(a) Heat flux (b) Stanton number

(c) Heat Flux (d) Stanton number

Figure 3-4. CFD laminar flow solution of the 33% scale BOLT model provided by The University of Minnesota (reproduced from [38]) and Texas A&M University (reproduced from [39]). (a) and (c) are the provided heat flux solutions and (b) and (d) are conversion to Stanton number at Texas A&M

Each facility obtained remarkable IR imagery, where the flow features compared well with one another. Slice extractions of heat flux at the same position on BOLT were taken and plotted with respect to one another for each of the diagnostics of each group. For reference of this slice, the CFD from Minnesota is repeated in Figure 3-5, where the white line denotes the position of the slice. The slice was taken approximately 0.4 inches from the back, just in front of the PCB instrumentation on the PEEK surface of the machined wind tunnel model. The *y*-axis in Figure 3-6 represents the heat flux and the *x*-axis is the non-dimensional length scale of BOLT. For comparison, TAMU IR results on the 3-D printed polycarbonate model, Purdue TSP and IR on the machined model, and CFD results from Minnesota and TAMU are shown.

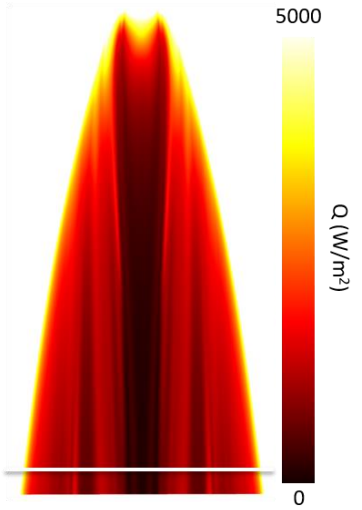

Figure 3-5. Slice extraction location on CFD from University of Minnesota.

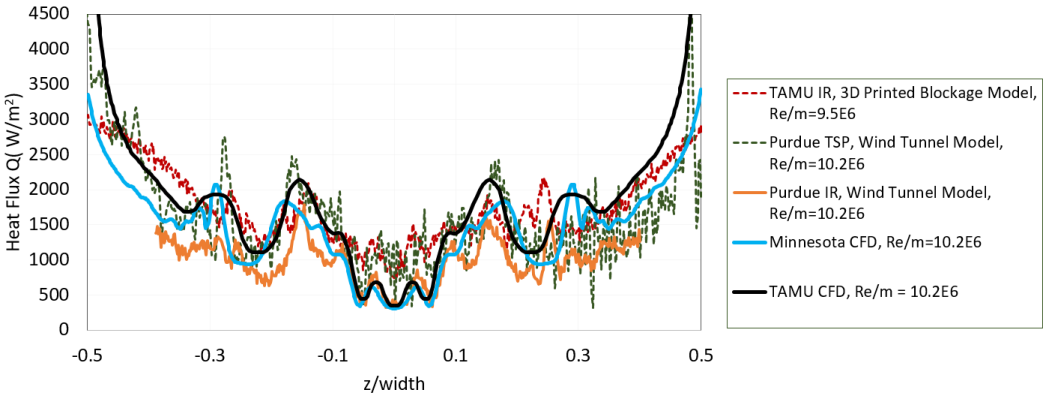

Figure 3-6. Line plot comparison of slice extractions on the machined 33% model, the 31% polycarbonate blockage model, TSP on the machined 33% model, and CFD from Minnesota and TAMU.

The results in Figure 3-6 are consistent across the research groups. Each group experiences similar streak-like structures at similar locations and the plot verifies it. Although the TSP is a bit noisy on the right-hand side of the graph, the left-hand side shows a cleaner line for comparison with the rest of the groups. Minnesota shows more streak-structures in their computations while TAMU CFD seems more dissipative in the results. The results in Figure 3-6 are rather promising. With different calculation techniques from two CFD groups and different diagnostic techniques in two wind tunnel facilities, heat flux values compared considerably as well as the location of the streaks on the surface.

3.1.2 Conventional Tunnel Results

The following conventional wind tunnel results will be shown at various Reynolds numbers. The color scheme follows the same format as the quiet tunnel results. The full-view IR results of BOLT in the 20-inch Mach 6 Air Tunnel at NASA Langley are shown in Figure 3-7. Flow over the model in the images is from left to right. Right away, it can

be seen that the flow structures on the surface of BOLT in a conventional wind tunnel facility are completely different from the structures in a low-disturbance environment. This effect was previously seen on the HIFiRE-5 wind tunnel model in Figure 1-4 and Figure 1-5. Instead of distinct streaks in the streamwise direction seen previously in quiet flow (Figure 3-1), two wedge-like structures originate from the back of the model and travel upstream with an increase in Reynolds number. The higher heating designates breakdown to turbulence has occurred.

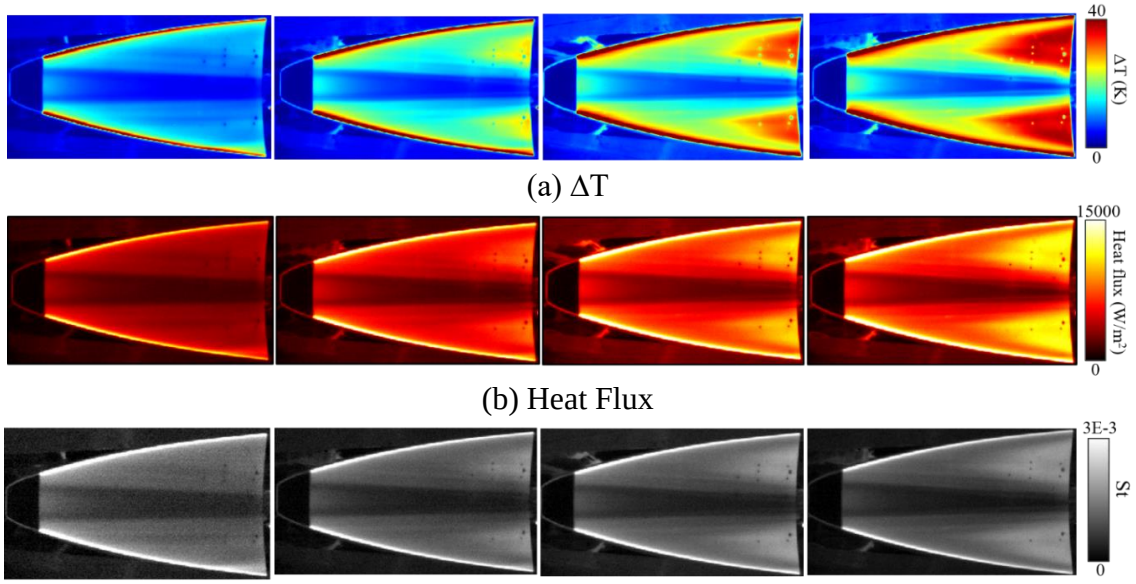

(a) ΔT

(b) Heat Flux

(c) St

Figure 3-7. NASA Langley Mach 6 IR thermography on the JHUAPL model (Left to right: Re/m = $3.5x10^6$, $5.6x10^6$, $6.7x10^6$, $8.0x10^6$) (reprinted from [46]). The entire model is shown in the facility. (a) is the change in temperature, (b) is the calculated heat flux using Texas A&M's 1-D heat transfer code, and (c) is the Stanton number

Similar results were seen on the surface of BOLT in the ACE facility at Texas A&M. With the flow from left to right, the turbulent structures on the surface in Figure 3-8 travel upstream on the model as the Reynolds number is increased. The heat flux on

the model in the ACE wind tunnel facility is a third of the magnitude of that in the 20-inch Mach 6 tunnel. This factor is due to the initial conditions within the facility, i.e. the temperature in the facility at Langley is higher.

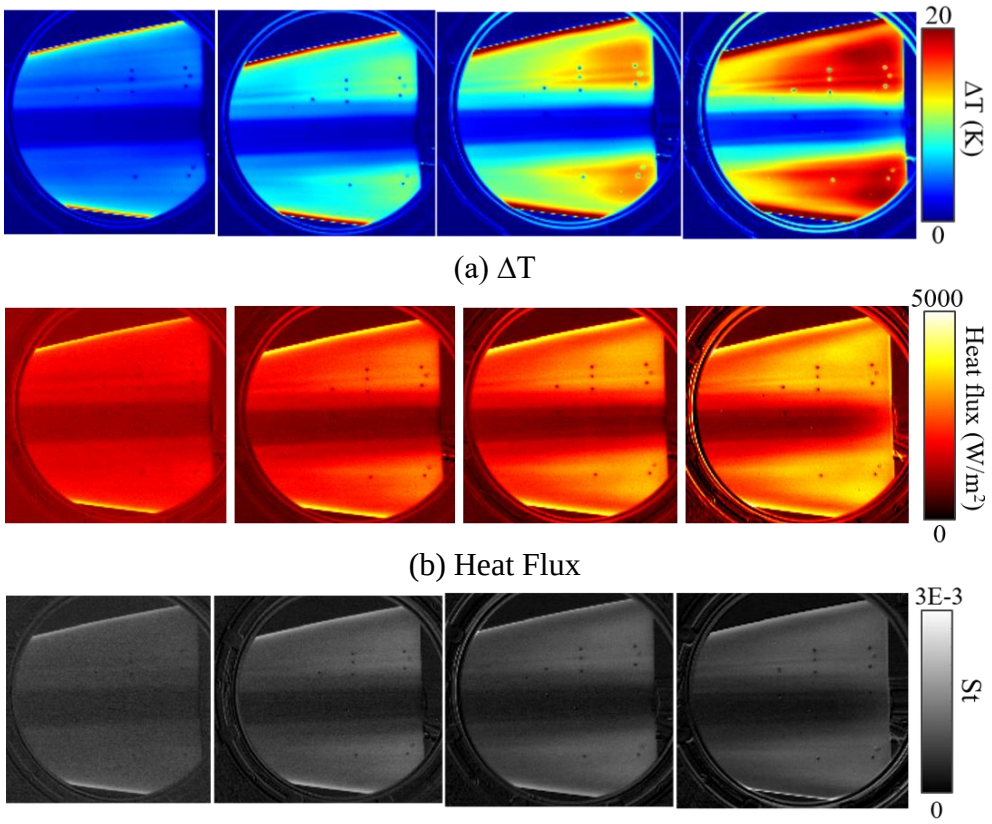

(a) ΔT

(b) Heat Flux

(c) St

Figure 3-8. TAMU ACE Mach 6 IR thermography results on the JHUAPL model (Left to right: Re/m = $3.5x10^6$, $5.6x10^6$, $6.7x10^6$, $8.0x10^6$) (reprinted from [46]). The back 6 in of the model is shown. (a) is the change in temperature, (b) is the calculated heat flux using Texas A&M's 1-D heat transfer code, and (c) is the Stanton number

The results in the BAM6QT at Purdue under noisy conditions are shown in Figure 3-9 at two Reynolds numbers, Re/m = $3.5x10^6$ and $8x10^6$. The flow is from left to right where the dots located on the surface represent 1-inch registration marks. Due to malfunctioning of the contraction Kulite in the tunnel at Purdue, freestream conditions

were inaccessible to convert to Stanton number. The wedge-like structure on the surface at the higher Reynolds number is similar to the results from Texas A&M and NASA Langley. However, the freestream disturbances located in the BAM6QT are much higher than the levels in ACE and the 20-inch Mach 6. This effect was previously compared between TAMU facilities and the BAM6QT conditions in Figure 2-10. The wedge itself is farther upstream on the model due to higher freestream disturbances within the facility. With a short run time, the heating on the model is low in the BAM6QT.

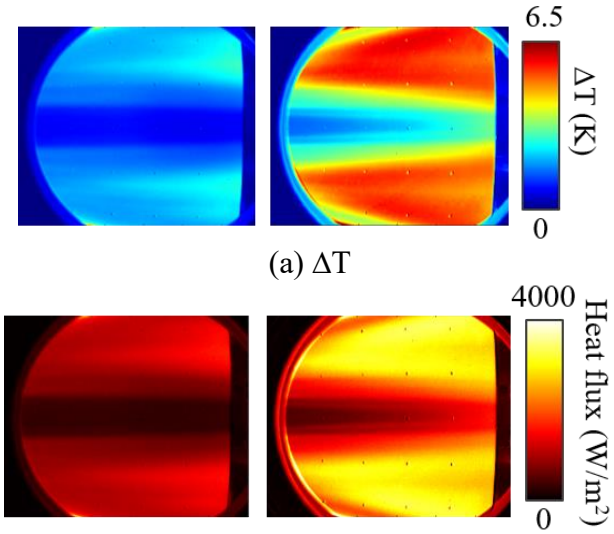

(a) ΔT

(b) Heat Flux

Figure 3-9. Purdue (Noisy) Mach 6 IR thermography results on the JHUAPL model (Left to right: Re/m = $3.5x10^6$, $8.0x10^6$) (reprinted from [46]). The back 6 inches of the model is shown. (a) is the change in temperature and (b) is the calculated heat flux using Texas A&M's 1-D heat transfer code

A 31% scale BOLT blockage wind tunnel model made of polycarbonate material was tested at two Mach numbers in the ACE facility. Mach 5.4 and Mach 7.4 lie within the Woomera flight trajectory and were desired for results. Figure 3-10 and Figure 3-11 are IR results at Mach 5.4 and Mach 7.4, respectively, in the ACE facility. The two circles

located on the model were from a previous campaign involving surface pressure transducers. These results will not be shown in this thesis. With flow from left to right, wedge-like structures travel upstream on the model as the Reynolds number increases. This verifies the same effect of turbulence not only occurs at Mach 6, but also at lower and higher Mach numbers. The extra streaks visible in Figure 3-11 at Mach 7.4 are due to a slight melting effect of the leading edge at high Reynolds numbers and high temperatures.

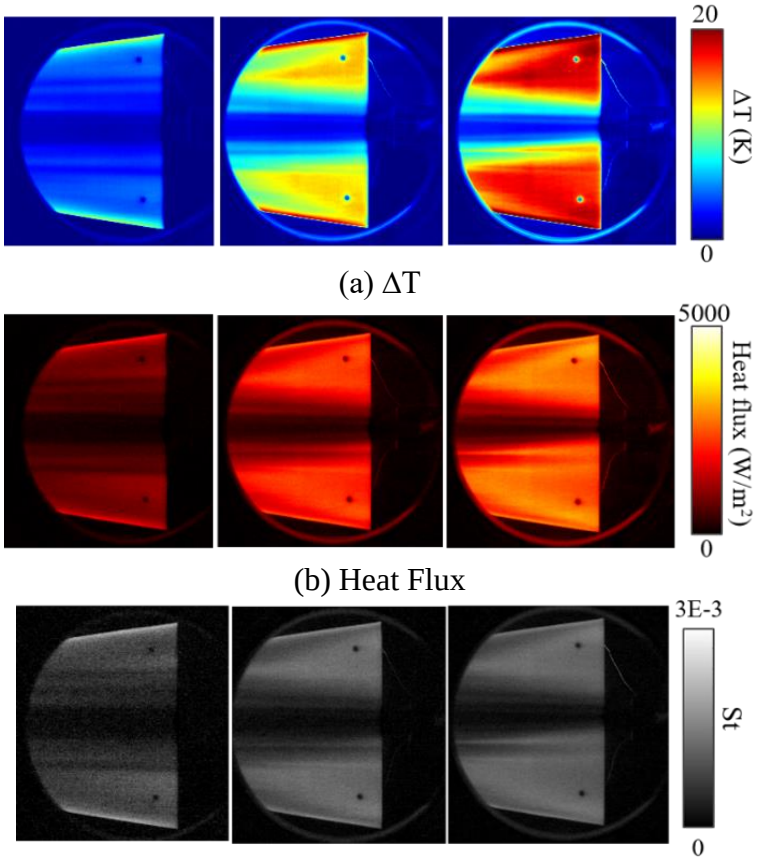

Figure 3-10. TAMU ACE Mach 5.4 IR thermography on the 31% scale blockage model of polycarbonate material (Left to right: Re/m = $3.5x10^6$, $5.6x10^6$, $6.8x10^6$) (reprinted from [46]). (a) is the change in temperature, (b) is the calculated heat flux using Texas A&M's 1-D heat transfer code, and (c) is the Stanton number

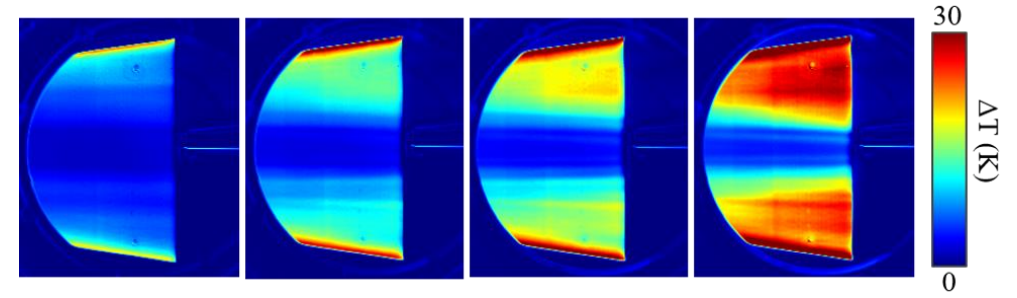

(a) ΔT

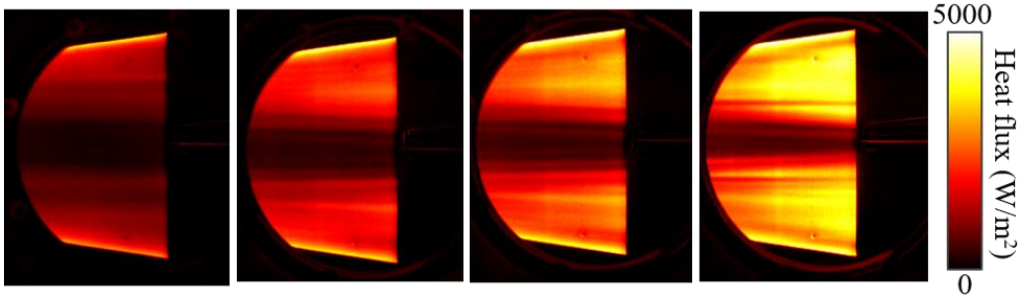

(b) Heat Flux

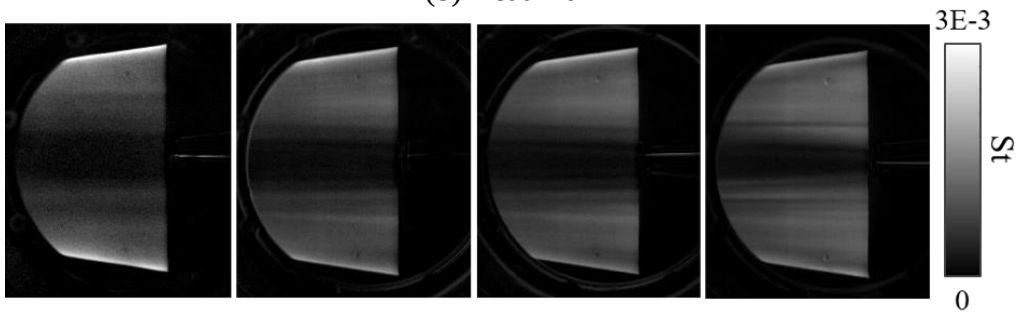

(c) St

Figure 3-11. TAMU ACE Mach 7.4 IR thermography on the 31% scale blockage model of polycarbonate material (Left to right: Re/m = $3.5x10^6$, $5.6x10^6$, $6.8x10^6$, $8.0x10^6$) (reprinted from [46]). (a) is the change in temperature, (b) is the calculated heat flux using Texas A&M's 1-D heat transfer code, and (c) is the Stanton number

Testing at CUBRC was incorporated into this thesis to gain a better understanding of the differences and similarities on the surface of BOLT in a high-enthalpy environment on a full-scale model. With the capability of producing flight-like velocities, the environment in the LENS II facility is that of conventional flow. A full-scale BOLT model was tested at Mach 7.4 with a Reynolds per meter of $8x10^6$. The heating observed on the solid aluminum model, shown in Figure 3-12 with flow from left to right, was captured by

TSP on the surface. The heat flux data were provided by JHUAPL. Even at high-enthalpy conditions, the turbulent wedges are present and the locations qualitatively compare with Figure 3-11 at the same Mach number and Reynolds number. The turbulent structures on the surface of BOLT in ACE, the BAM6QT (noisy conditions), 20-inch Mach 6, and LENS II are similar even at different Mach and Reynolds numbers.

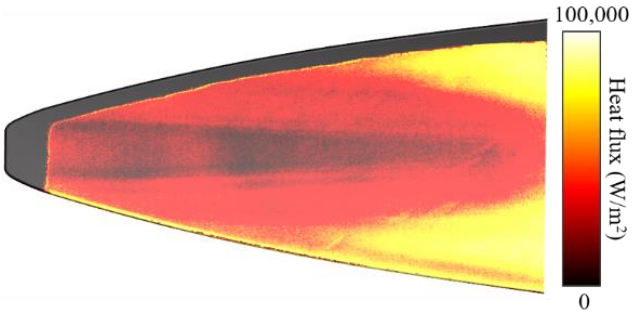

Figure 3-12. CUBRC Mach 7.4 TSP on the full-scale BOLT model in the LENS II facility at Re/m = 8.0×10^6 (reprinted from [46]).

3.2 Heat Transfer Code and Schmidt Boelter Gauge Comparison

As previously mentioned in section 2.3, Texas A&M National Aerothermochemistry and Hypersonics Laboratory developed a MATLAB code for converting infrared temperature maps into heat flux. In the current section, a comparison between the code and Schmidt Boelter gauge data will be assessed. The data analyzed involved roughness 'trip-heights' on the model to instigate transition that was tested at NASA Langley. Due to malfunction of the Schmidt Boelter gauges for 'smooth' (non-tripped) wind tunnel runs, wind tunnel runs with a roughness present will be analyzed. For this thesis, however, the roughness heights are not of interest; the heat flux values downstream on the model are. The process involved the usual method of computing heat flux using the in-house heat transfer code at A&M for Langley IR images. The values in

the IR image computed near the region of the Schmidt Boelter gauge were compared to the actual gauge data. The location of the gauge on the PEEK surface is shown for reference again in Figure 3-13, although the image itself is flipped to better correlate with the IR images.

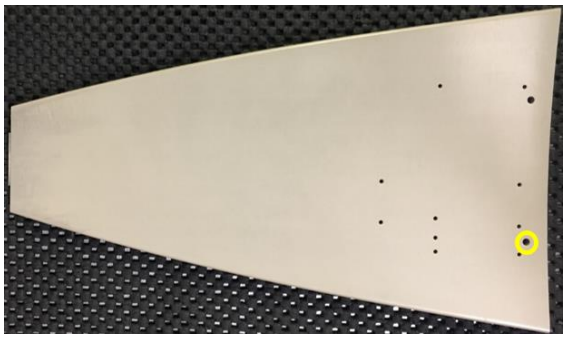

Figure 3-13. Location of the Schmidt Boelter gauge for analysis.

Six different wind tunnel runs were chosen for comparison and are shown in Figure 3-14. The *X* and *Y* refer to pixel location in the image, the *Index* label is the heat flux value in W/m^2, and *R*, *G*, *B* refer to the color mapping in MATLAB. Roughness trips can be seen on the model for different configurations in each image. The Schmidt Boelter gauge is located directly behind the point of measurement in Figure 3-14, seen as a red dot (also circled in Figure 3-13). The data from the sensor were provided to TAMU from NASA Langley for each wind tunnel run. The overall comparison between the two measurements, IR and sensor, is listed in Table 3-1. The data between the code and the sensor measurement agree within 6%.

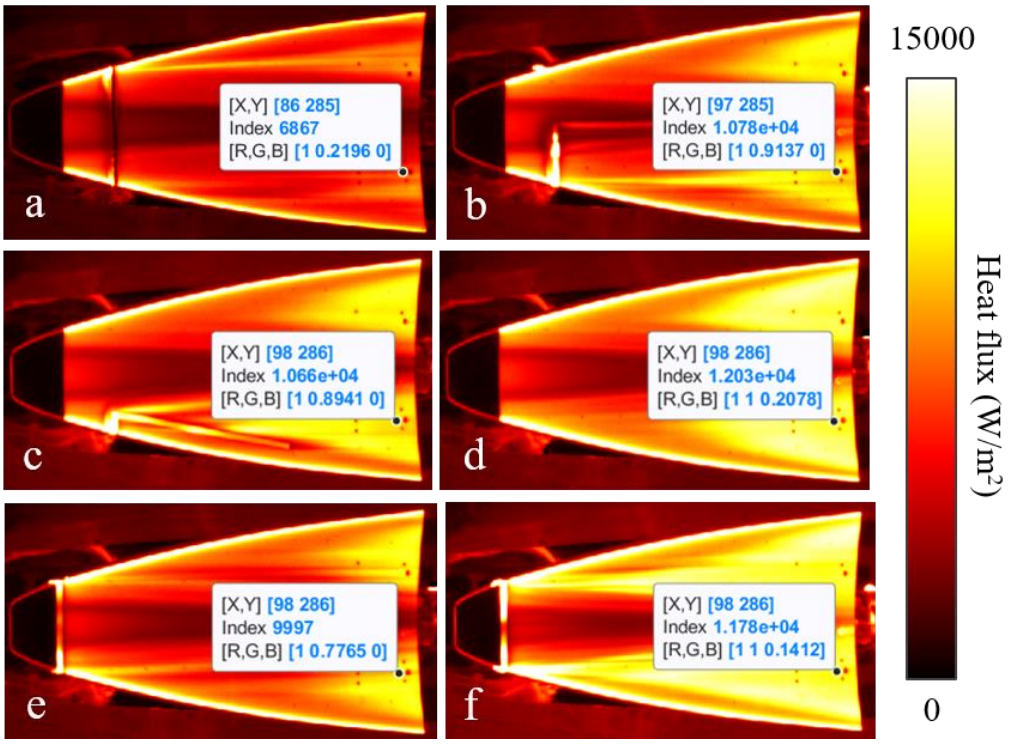

Figure 3-14. Heat flux data on the model for various wind tunnel runs at NASA Langley. Reynolds number for each image from (a) to (f) is Re/m = $4.9x10^6$, $7.95x10^6$, $7.88x10^6$, $9.38x10^6$, $7.89x10^6$, and $9.47x10^6$, respectively. Images portray different roughness configurations.

Table 3-1. Heat transfer results and Schmidt Boelter gauge results

Reynolds Number	IR Heat Flux Data (kW/m^2)	Schmidt Boelter Data (kW/m^2)	Percentage %
$4.90x10^6$	6.87	6.50	5.39
$7.95x10^6$	10.78	10.93	1.39
$7.88x10^6$	10.66	10.62	0.38
$9.38x10^6$	12.03	12.56	4.41
$7.89x10^6$	10.00	9.96	0.40
$9.47x10^6$	11.78	11.32	3.90

When comparing other wind tunnel runs, the difference between the two variables varied more at the lower and higher range of Reynolds numbers within the campaign. The frames chosen for comparison during the run would also alter the measurement. Thus, for this analysis, frames near 1.3 seconds into the run were chosen for less variation and

uncertainty in the results. Schmidt Boelter measurements can be off from the theoretical heat transfer value by 20-25% as previously measured at Purdue on a straight, sharp cone at 0° AoA [69].

3.3 Surface Pressure Transducers

Surface pressure spectra were acquired with Kulite and PCB pressure transducers to help identify instability mechanisms. The IR visualization provided a basis to locate the instrumentation on the model.

3.3.1 Surface Pressure Spectra – Conventional Flow

In this section, PSD plots for surface pressure spectra are shown for conventional flow. The TAMU ACE and Langley 20-inch Mach 6 provided Reynolds number sweeps, while at Purdue a fixed Reynolds number condition is provided. All voltage measurements were calibrated to pressure. The legend in each PSD plot represents the spectra at a specific Reynolds number. The processing techniques and filtering for each facility were discussed earlier in Chapter 2, i.e. the sharper roll-off in the data from Langley is due to filter cut-off. Although there are 35 sensor locations on the model, only a few important locations will be discussed in this section. Appendix E contains the rest of the data for the surface pressure transducers in conventional flow. Not every facility collected data at every location which will be seen in the results.

The off-centerline Kulites proved to capture an instability in conventional flow in each facility. The Kulites in locations 1, 9 and 27 stand out with a modal growth around 30-40 kHz. The mode, first captured by K1, is present in all facilities and seen in Figure 3-15. In Figure 3-15a, the mode appears at a Reynolds per meter of 3.5×10^6 and continues

to grow as the Reynolds number is increased. This is due to the nozzle sidewalls transitioning in the ACE facility and incorporating higher freestream disturbances on the surface of BOLT. The same mode is captured in the facilities at both Purdue and Langley and is seen in Figure 3-15b-c. The mode is present for all Reynolds numbers at Langley as well as the single data point spectra at Purdue. As the flow travels downstream on the model, K27 is the next off-centerline location to capture the same instability. The mode shows existence in the ACE facility around Re/m = $3x10^6$ and is present in the Purdue facility at the designated Reynolds number in Figure 3-16. Traveling farther downstream on the model to K9, the mode is visible in all three facilities in Figure 3-17. Similar to the growth in K27, the mode begins to grow at Re/m = $3x10^6$ in the ACE facility. In Figure 3-17c, the instability is present at lower Reynolds numbers, but the freestream noise environment within the 20-inch Mach 6 masks the results at higher Re/m. The locations of these three Kulite sensors, K1, K9 and K27, prove to be of importance for future analyses.

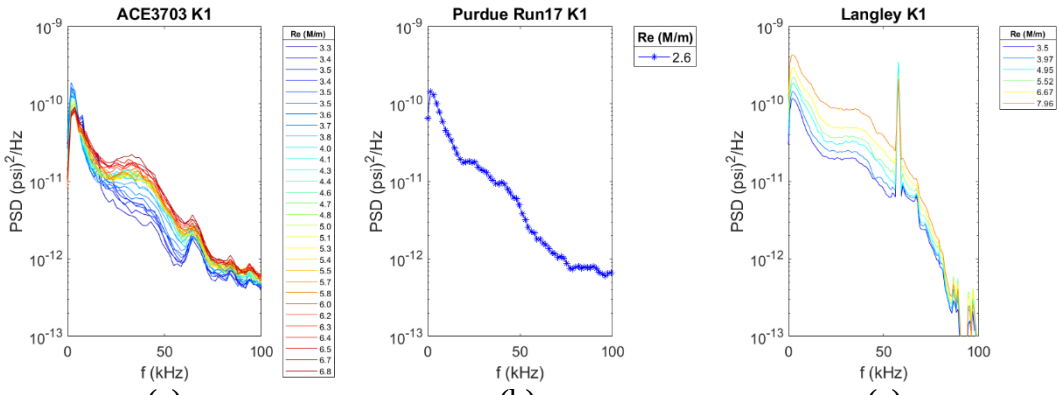

Figure 3-15. Results of surface pressure spectra in three conventional flow facilities for K1; (a) Texas A&M ACE tunnel (reprinted from [47]), (b) Purdue BAM6QT operated in conventional mode (reprinted from [46]), and (c) NASA Langley 20-inch Mach 6

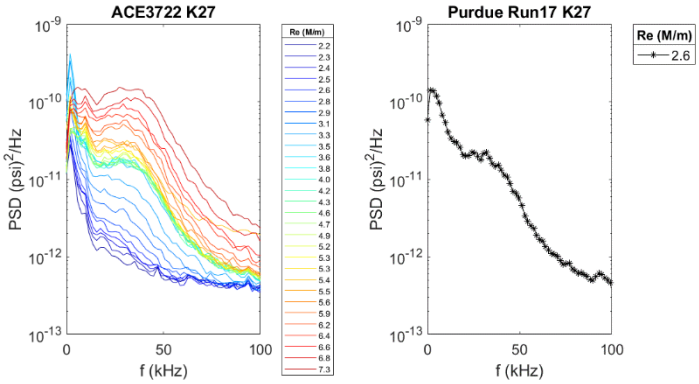

(a) (b)

Figure 3-16. Results of surface pressure spectra in two conventional flow facilities for K27; (a) Texas A&M ACE tunnel (reprinted from [47]) and (b) Purdue BAM6QT operated in conventional mode (reprinted from [46])

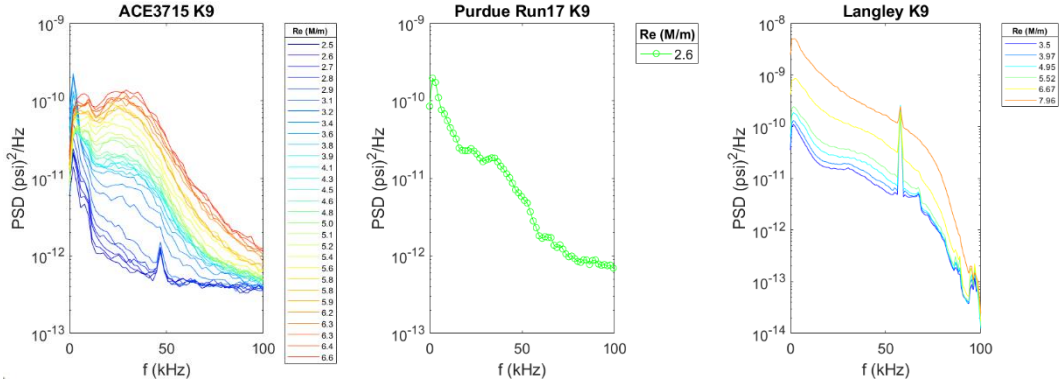

(a) (b) (c)

Figure 3-17. Results of surface pressure spectra in three conventional flow facilities for K9; (a) Texas A&M ACE tunnel (reprinted from [47]), (b) Purdue BAM6QT operated in conventional mode, and (c) NASA Langley 20-inch Mach 6

The spectra from the PCB sensors did not show defined modal growth as seen in the off-centerline Kulites. Instead, broadband growth is seen as the Reynolds number is increased in the facility. All groups featured noise interference in the PCB sensors when mounted in the aluminum surfaces of the subscale model. Therefore, the majority of the PCB sensors are deemed unusable for data comparison. These data are located in Appendix E. In Figure 3-18, both A&M and Langley experience a broad growth with no

modes apparent with an increase in Reynolds number. At the same streamwise location and mirrored to P8 is P11 in Figure 3-19. The data at P11 verify the same results of P8 in the ACE facility. Similar broadband content is also observed in P25 and P31 in Figure 3-20 and Figure 3-21, respectively. The peaks seen in the spectra at Purdue in Figure 3-20b are due to oscillations in the sensor from electronic noise.

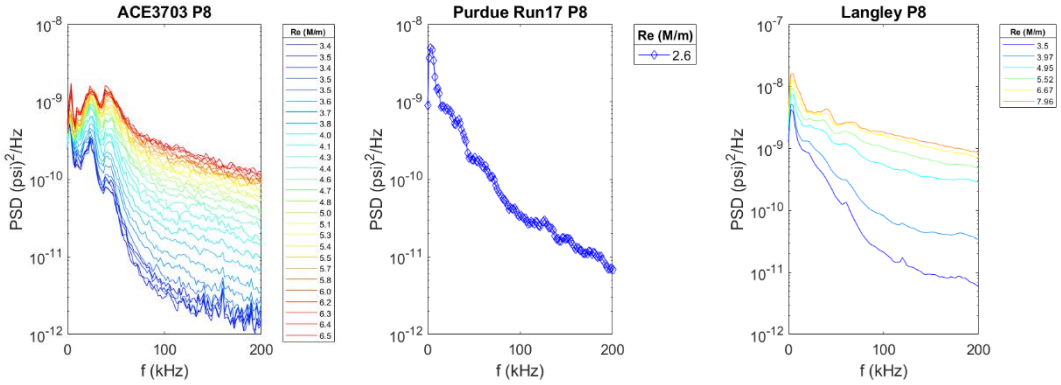

Figure 3-18. Results of surface pressure spectra in three conventional flow facilities for P8; (a) Texas A&M ACE tunnel, (b) Purdue BAM6QT operated in conventional mode (reprinted from [46]), and (c) NASA Langley 20-inch Mach 6 Tunnel (reprinted from [46])

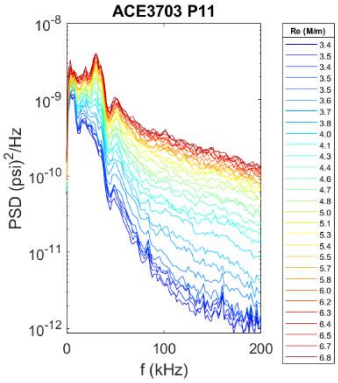

Figure 3-19. Results of surface pressure spectra in the Texas A&M ACE tunnel for P11.

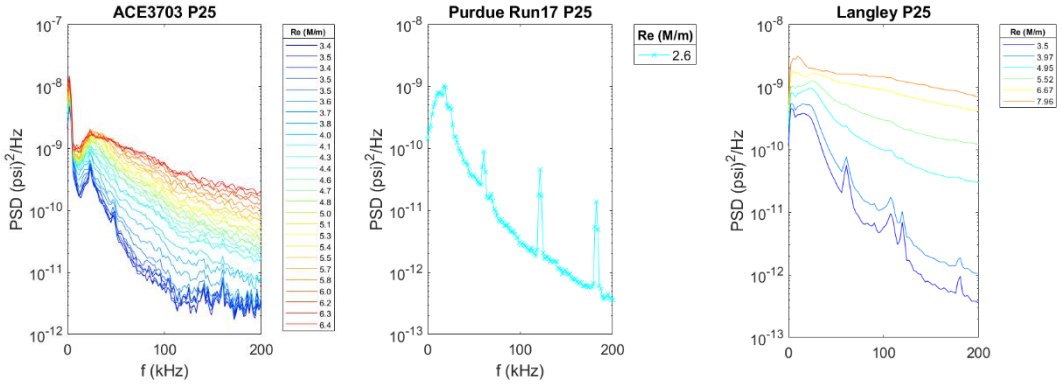

(a) (b) (c)

Figure 3-20. Results of surface pressure spectra in three conventional flow facilities for P25; (a) Texas A&M ACE tunnel, (b) Purdue BAM6QT operated in conventional mode, and (c) NASA Langley 20-inch Mach 6 Tunnel

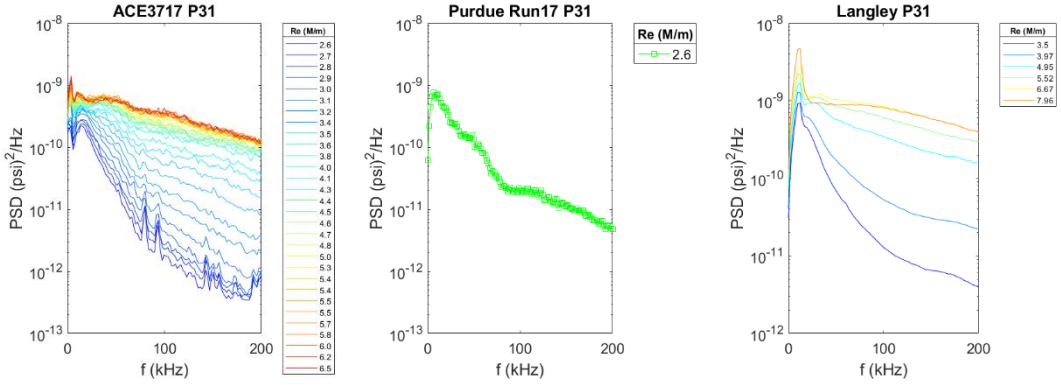

(a) (b) (c)

Figure 3-21. Results of surface pressure spectra in three conventional flow facilities for P31; (a) Texas A&M ACE tunnel, (b) Purdue BAM6QT operated in conventional mode, and (c) NASA Langley 20-inch Mach 6 Tunnel

3.3.2 Surface Pressure Spectra – Quiet Flow

Quiet flow results in the M6QT and the BAM6QT for BOLT are presented in this section. It should be noted that Run 10 at Purdue contains an incorrectly installed nosetip. The other sensor results, (located in Appendix F) are taken from two different wind tunnel runs, Run 10 and Run 16, due to sensor malfunction. Each facility acquires data differently as previously stated in Table 2-4. The final results at Purdue are seen differently under

quiet flow. Instead of a gradual 'bump' in the data to signify growth at a certain frequency that was seen by all facilities for conventional flow, sharp peaks at the frequency of suspected growth will be visible instead. This feature is quite different from their conventional flow results, so caution should be taken when analyzing the data in this section.

Taking a look at the same off-centerline Kulites analyzed for conventional flow, a similar 30 – 40 kHz mode is seen in quiet flow. The mode is first visible in the spectra in Figure 3-22 for both facilities. The mode is not seen in K1 until higher Reynolds numbers in the M6QT. Moving downstream to K27 in Figure 3-23, the mode is only apparent in the spectra at Texas A&M. The nosetip installation at Purdue may have affected the results. So far, the results are similar to what was observed under conventional flow. Lastly along the centerline, little to no growth is seen in K9 in Figure 3-24a but Figure 3-24b shows some content.

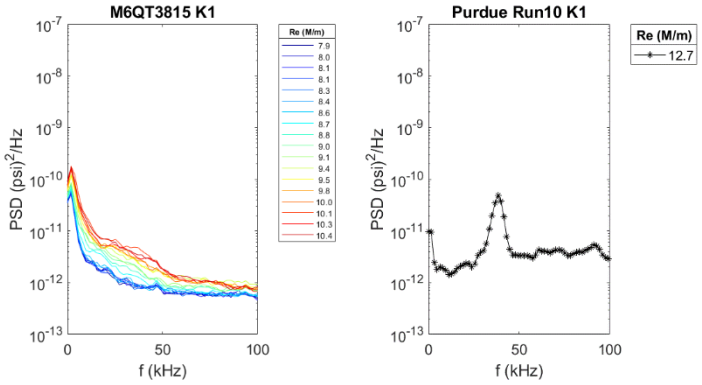

(a) (b)

Figure 3-22. Results of surface pressure spectra in two quiet flow facilities for K1; (a) Texas A&M M6QT (reprinted from [47]) and (b) the BAM6QT

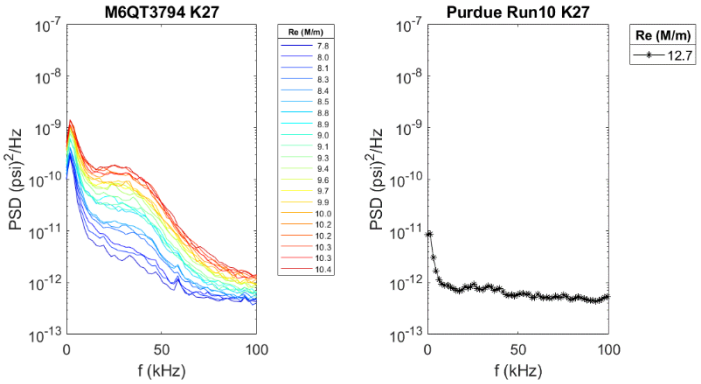

(a) (b)

Figure 3-23. Results of surface pressure spectra in two quiet flow facilities for K27; (a) Texas A&M M6QT (reprinted from [47]) and (b) the BAM6QT (reprinted from [46])

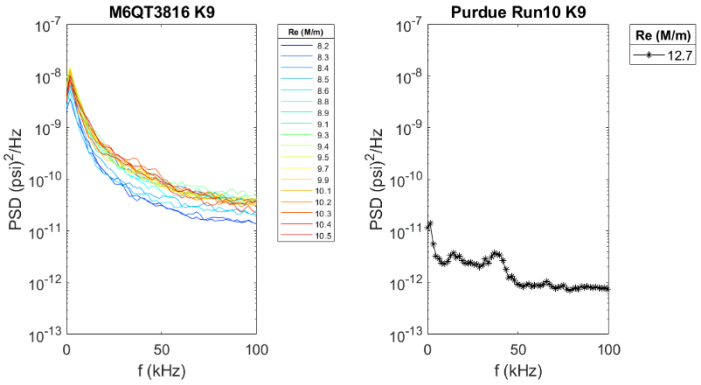

(a) (b)

Figure 3-24. Results of surface pressure spectra in two quiet flow facilities for K9; (a) Texas A&M M6QT (reprinted from [47]) and (b) the BAM6QT

In conventional flow, no modal growth was observed in K10 (see Appendix E). However, a 30 – 40 kHz mode is seen in both the M6QT and the BAM6QT in Figure 3-25. This result is still of discussion at this location. Model orientation, such as a slight yaw, could have caused a slight variation in the flow over the sensors during these wind tunnel runs. The nosetip installation before Run 10 may have contributed to the additional content in Figure 3-25b.

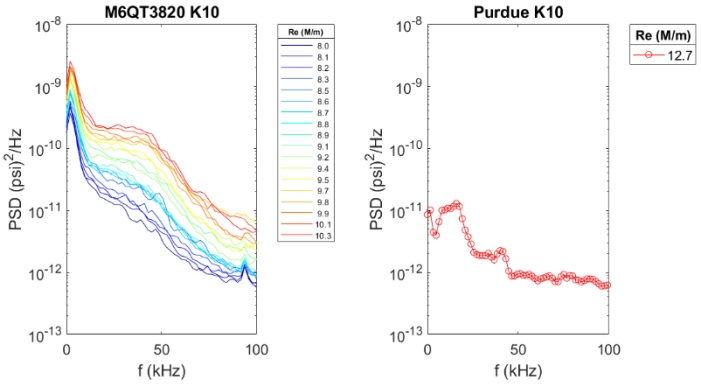

(a) (b)

Figure 3-25. Results of surface pressure spectra in two quiet flow facilities for K10; (a) Texas A&M M6QT and (b) the BAM6QT

The results of the PCB sensors mounted in the aluminum surfaces in quiet flow contained noise interference similar to the conventional flow results. Thus, only results in the PEEK surface will be shown in this section. The results for P8 and P11 in Figure 3-26 and Figure 3-27, respectively, were similar to the results in conventional flow. Broadband growth is observed in both of the sensors in the M6QT, as well as mirrored results between the two locations. No modal growth was observed in any of the PCB sensors for both facilities.

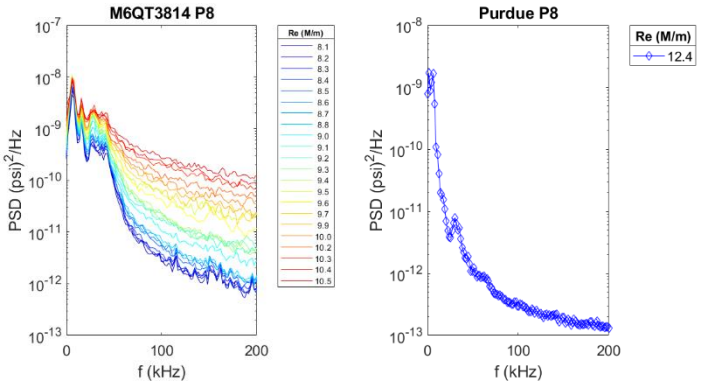

(a) (b)

Figure 3-26. Results of surface pressure spectra in two quiet flow facilities for P8; (a) Texas A&M M6QT and (b) the BAM6QT

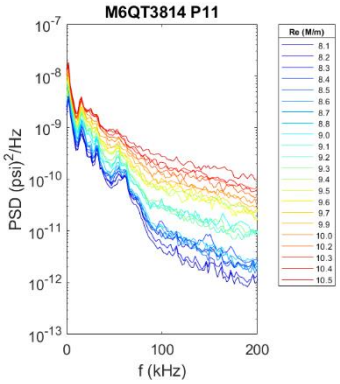

Figure 3-27. Results of surface pressure spectra in the Texas A&M M6QT for P11.

3.4 Instabilities and Transition

Off-body measurements were made in the region of the vortical mode from the SPDMD results discussed earlier in Chapter 1 due to the unique structure as well as the close proximity to the off-centerline Kulites. The reader should refer to Thome et al. 2019 for reference on the mathematics behind the computations as well as Knutson et al. 2018 [42, 70]. The current section utilizes quiet flow at a Re/m = 9.9×10^6.

3.4.1 Numerical Simulation

For the current analyses, the streamwise location within the vortical mode at x = 0.24 m was chosen due to the ease of access of this location with the traverse in the M6QT as well as current data computed by Thome et al. 2019 [42]. At this position within the vortical mode, the hot-wire measurements are between K1 and K27. A slice within the vortical mode at x = 0.24 m for a quarter of the geometry is shown in Figure 3-28. The colors represent both the positive and negative streamwise velocity perturbations $u'_\xi = \pm 3 \times 10^{-6}$ m/s where the isolines represent the mean streamwise velocity. The *y*-coordinate is the vertical location from the center of the geometry and the *z*-coordinate is the spanwise

location from the centerline. Listed in the plot is the dominant frequency of 37 kHz at this location computed from SPDMD.

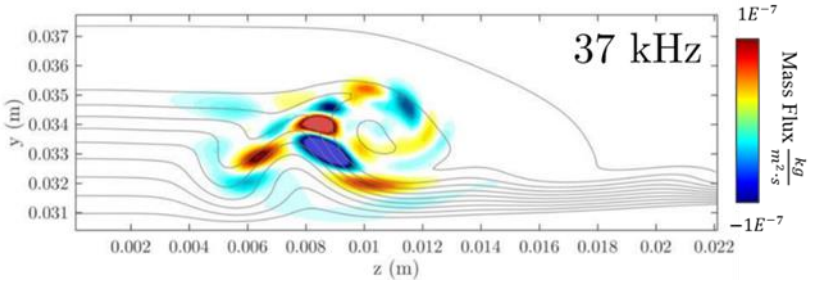

Figure 3-28. At x = 0.24 m, the u'$_\xi$ mode with the dominant frequency listed as 37 kHz from the SPDMD analysis (modified from [42]).

Since the locations of content in Figure 3-28 are for a broad range, the author was provided with a similar plot at the same *x*-location within the vortical mode to better determine locations of interest for hot-wire measurements for the given 37 kHz frequency. The plot in Figure 3-29 represents the streamwise velocity disturbance magnitude of the dominant frequency. The *y*- and *z*-coordinate definitions are the same as the previous figure. The locations of content in Figure 3-29 help to map out hot-wire measurements in the M6QT. The off-centerline Kulites are located at z = 6.35 mm, directly under the first structure seen in Figure 3-29.

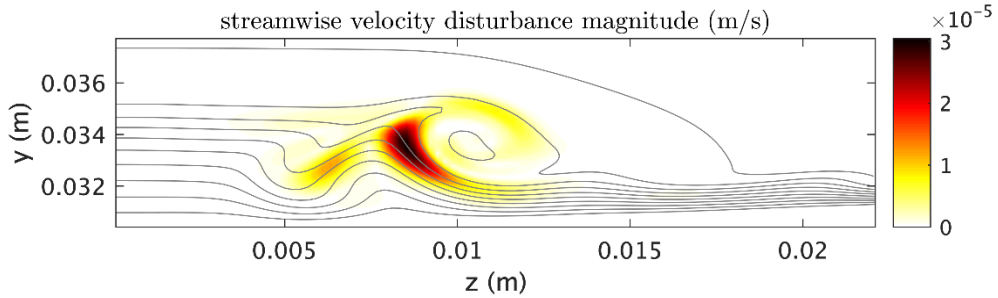

Figure 3-29. Streamwise velocity disturbance magnitude of the dominant mode of 37 kHz (reprinted from [47]).

3.4.2 Hot-wire measurements on BOLT

Hot-wire measurements were taken off the surface of the TAMU 33% scale machined BOLT model in the M6QT. Locations of measurements inside the instability region were determined from Figure 3-29 and are stated in Table 3-2 for each wind tunnel run. The *y*- and *z*- locations stated in the table are the same definition as the *y*- and *z*-coordinates in the plots provided by the University of Minnesota but in millimeters. Each wind tunnel run consisted of the hot-wire traversing straight up in the *y*-direction while stepping in the *z*-direction when applicable. Since the traverse operates in an *r*-θ-*z* movement, *y* and *z* were converted to polar coordinates accordingly for each sweep. All hot-wire measurements are un-calibrated and left in voltage.

Table 3-2. Hot-wire traverse locations for each wind tunnel run.

Run #	Z location (mm)	Y location (mm)	TSI Probe
4015	8.6	32-35	1220-PI2.5 (A)
4016	8.7	32-35	1220-PI2.5 (A)
4017	8.5	32-35	1220-PI2.5 (B)
4018	8.8	32-35	1220-PI2.5 (B)
4019	8.2	32-35	1220-PI2.5 (B)
4020	8.6	32-40	1220-PI2.5 (B)
4022	5.5, 5.97, 6.43, 6.9	32-37	1220-PI2.5 (B)
4023	7.4, 7.8, 8.3, 8.8	32-37	1220-PI5
4098	8.7, 9.3, 9.8	32-39	1220-PI2.5 (C)
4099	10.3, 10.8, 11.4	32-39	1220-PI2.5 (C)
4100	11.9, 12.4, 12.9	32-39	1220-PI2.5 (C)
4101	13.5, 14, 14.5	32-39	1220-PI2.5 (C)
4103	7.2, 7.7, 8.2	32-39	1220-PI2.5 (C)
4104	5.6, 6.1, 6.6	32-39	1220-PI2.5 (C)
4105	4.0, 4.5, 5.1	32-39	1220-PI2.5 (C)
4108	15, 15.6, 16.1	32-39	1220-PI2.5 (C)
4109	16.6, 17.1, 17.7	32-39	1220-PI2.5 (C)
4112	18.2, 18.7, 19.2	32-39	1220-PI2.5 (C)
4113	19.8, 20.3, 20.8	32-39	1220-PI2.5 (C)

The results forthcoming are preliminary and still of discussion. The first hot-wire experimental campaign focused on the amplified region of Figure 3-29 (Run 4015-4019)

with fine increments in the *y*-direction. These results are shown in Figure 3-30 with similar content seen in all plots. The legends for the PSD plots in Figure 3-30 represent the spectra for each of the measured *y*-locations. A 20 – 40 kHz structure is seen in the spectra. While the hot-wire moves in and out of the vortical mode of Figure 3-29, content is seen in the data, starts to grow, and begins to collapse. A zoomed-in view of this effect is shown in Figure 3-31. The peaks at 19 and 50 kHz are strain-gauging in the wire but these do not pose as an interference in the final results.

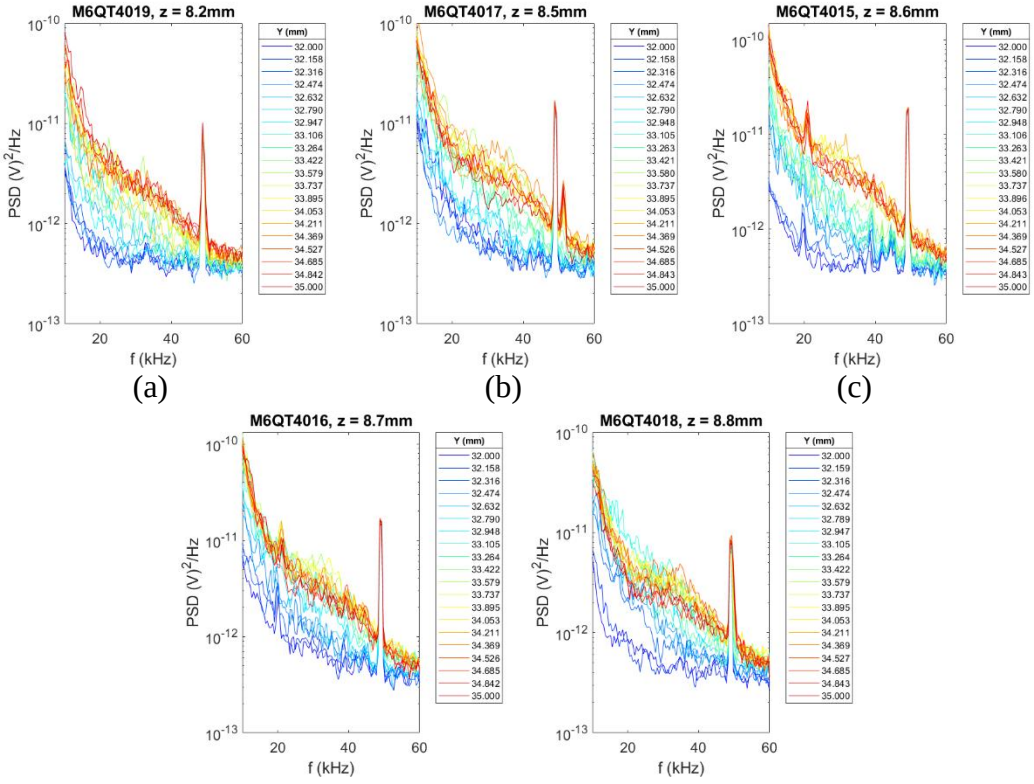

Figure 3-30. Preliminary hot-wire traverse data for five locations (modified from [47]). The different PSD lines in each plot represent data taken at a specific *y* location.

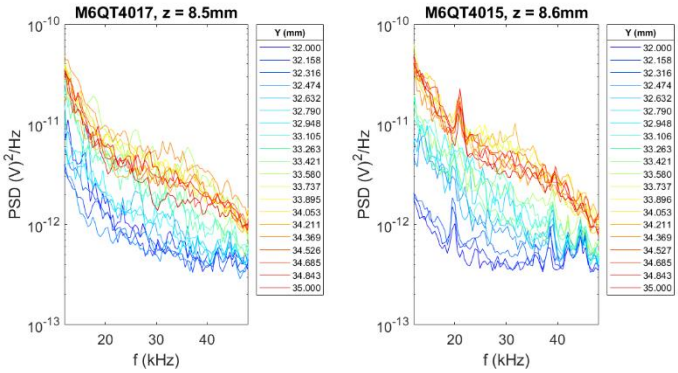

(a) (b)

Figure 3-31. Zoomed in plots of locations z = 8.5mm and 8.6mm (modified from [47]).

The next experimental campaign involved stepping well out of the amplified region in Figure 3-29 and towards the boundary layer (Run 4020). Therefore, a higher upper-bound in *y* was needed. Location z = 8.6 mm was repeated for this campaign. Upon moving in and out of the vortical mode, a sudden peak appears around y = 37 mm in the spectra in Figure 3-32**.** The peak continues to grow in magnitude and frequency as the hot-wire moves toward the boundary layer edge. It is unclear whether the hot-wire is outside the boundary layer at this point and the sudden occurrence of the peak is still of discussion.

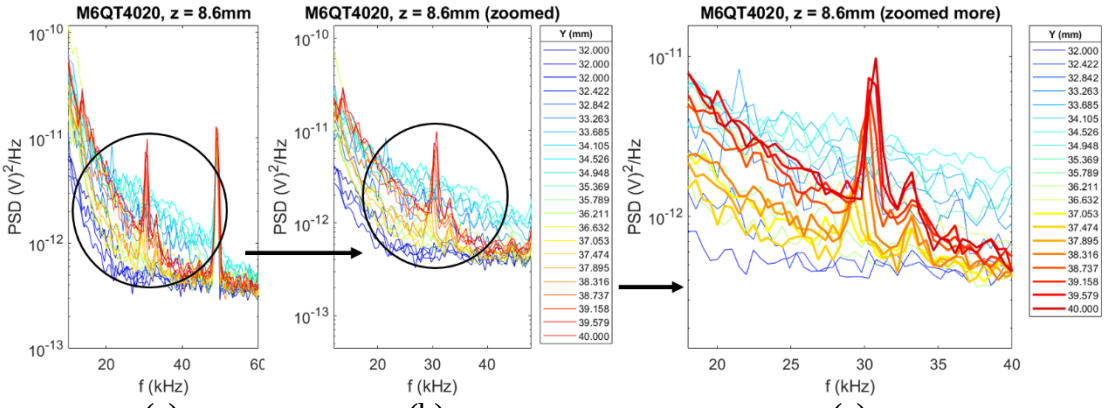

(a) (b) (c)

Figure 3-32. Hot-wire PSD for Run 4020 in and out of the vortical mode (modified from [47]). (a) PSD, (b) zoomed in view, (a) more zoomed in view of the growth of the structure

The last two experimental campaigns for this thesis focused on visualizing the structure of the vortical mode in Figure 3-29. A key note should be cautiously taken: different measurement scales are used for comparison. Rather, the region of disturbances and amplification are compared between simulations and experiments. A 2-D contour of the RMS normalized by the mean voltage for each measured point from z = 5.5 – 8.8 mm is plotted in Figure 3-33 for Run 4022 and Run 4023. The *y*- and *z*- locations are defined the same as above. The RMS is calculated from the DC voltage for each measured point using Equation 3.1. For the hot-wire measurements, the number of samples per measurement corresponds to 50,000 samples. Less fine increments in the *y*-direction with more steps in *z* were made for a larger area during a single wind tunnel run.

$$RMS_{single\ point} = \sqrt{\frac{(x_1-\bar{x})^2+\cdots+(x_n-\bar{x})^2}{\#\ of\ samples}} \tag{3.1}$$

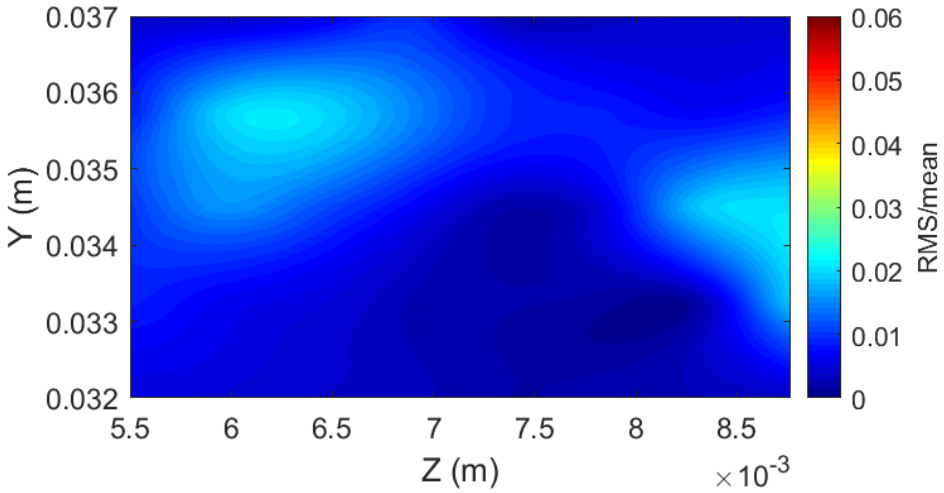

Figure 3-33. RMS normalized by the mean voltage for each point measured in Run 4022 and 4023 (reproduced from [47]).

The regions of sudden amplification in Figure 3-33 are similar to the regions in Figure 3-28 and Figure 3-29. The data between z = 7.5 – 8.8 mm appears to align well with the simulations. The location from z = 5.5 – 7.5 mm is precisely where the off-centerline Kulites are located, approximately 6.35 mm off-centerline. At this location, Thome et al. reports a 37 kHz amplitude [42], while the Kulites see a 35 kHz growth. Wire breakage prevented acquiring data over the entire vortical mode region during this campaign, but a second campaign was established to visualize the entire structure with a single hot-wire probe. A 2-D contour of RMS normalized by the mean voltage for eleven wind tunnel runs is plotted in Figure 3-34. RMS was calculated using the trapezoidal rule for the PSD spectra integrated over all frequencies. The vortical structure is apparent and the shape resembles that of Figure 3-29. Experimental measurements were taken farther off-centerline after observing additional content not seen in the computations. These features are still of discussion within these results. The spanwise locations where content is observed in the experiments may be slightly shifted in the plot due to human error for the coordinates of the traverse and/or a slight yaw of the model. Comparing to simulations, the vortex structure in the experiments is approximately 1 - 2 mm off for this campaign.

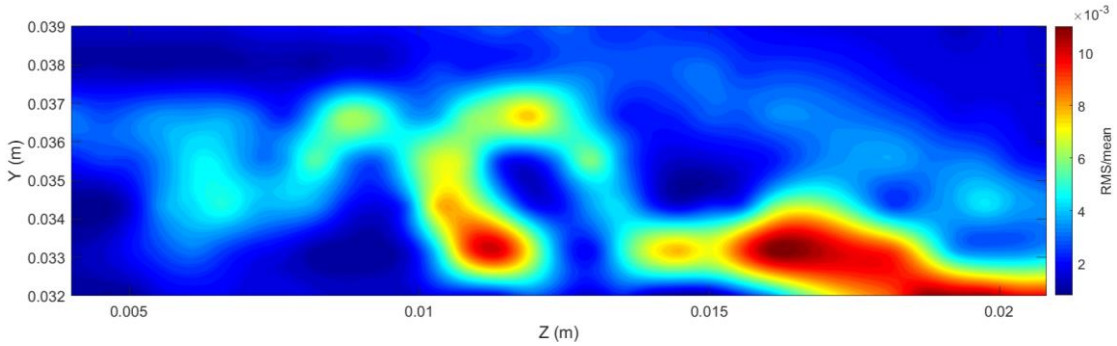

Figure 3-34. RMS normalized by the mean voltage for each point measured in Run 4098, 4099, 4100, 4101, 4103, 4104, 4105, 4108, 4109, 4112, and 4113.

The hot-wire PSD spectra within the vortex region from z = 10.3-11.4 mm in Figure 3-34 are plotted in Figure 3-35. Content is observed between 20-50 kHz in the spectra at the *y*-locations similar to the vortex region in Figure 3-34. Peaks observed around 19 and 63 kHz are due to strain-gauging in the wire at higher *y*-locations. With an integration from 25-40 kHz, the structure in the lower right corner in Figure 3-36 begins to fade as well as the top of the vortex structure. Spectra for z = 7.2-8.2 mm are plotted in Figure 3-37 due to their intensity within this band. Content is observed between 20-40 kHz at these locations.

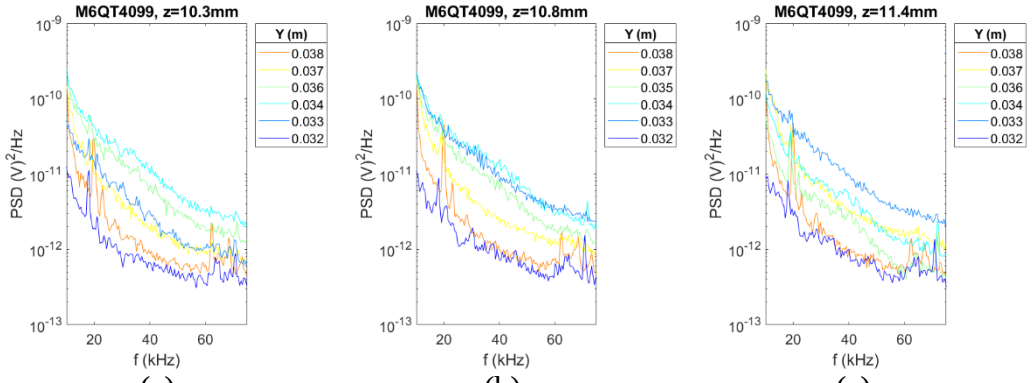

(a) (b) (c)

Figure 3-35. PSD spectra in the vortex region at z-locations (a) 10.3mm, (b) 10.8mm, and (c) 11.4mm.

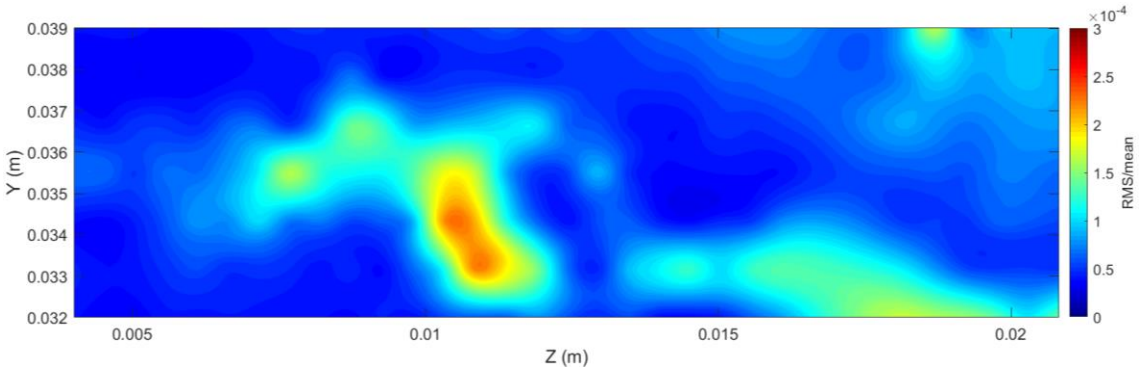

Figure 3-36. RMS normalized by the mean voltage for each point computed between the frequency band of 25-40 kHz for Run 4098, 4099, 4100, 4101, 4103, 4104, 4105, 4108, 4109, 4112, and 4113.

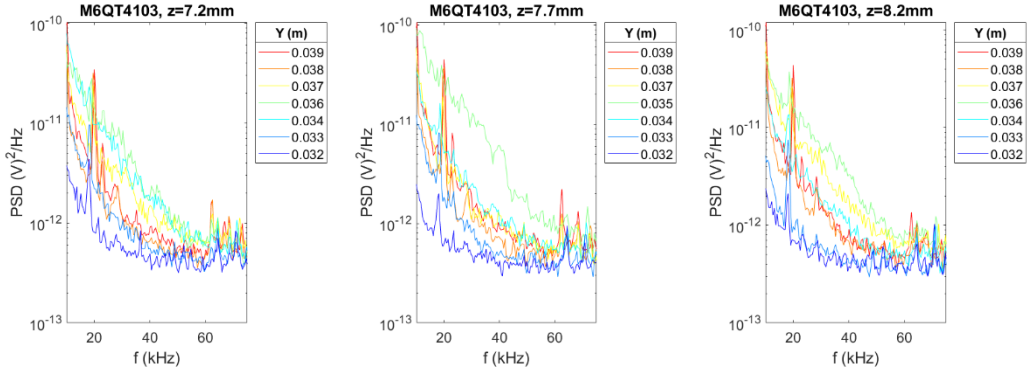

(a) (b) (c)

Figure 3-37. PSD spectra for z-locations (a) 7.2mm, (b) 7.7mm, and (c) 8.2mm.

Further analysis was continued in the region to the right of the vortex. The PSD spectra for this region are plotted in Figure 3-38. The spectra show little to no broadband growth at these locations. Therefore, an integration band for analysis in this region is limited. Higher amplitudes in the PSD spectra around 32-33 mm in the *y*-direction influenced the intensity in the contour plots. Finer increments in the *y*-direction at these locations would give ideal results in the spectra for analysis.

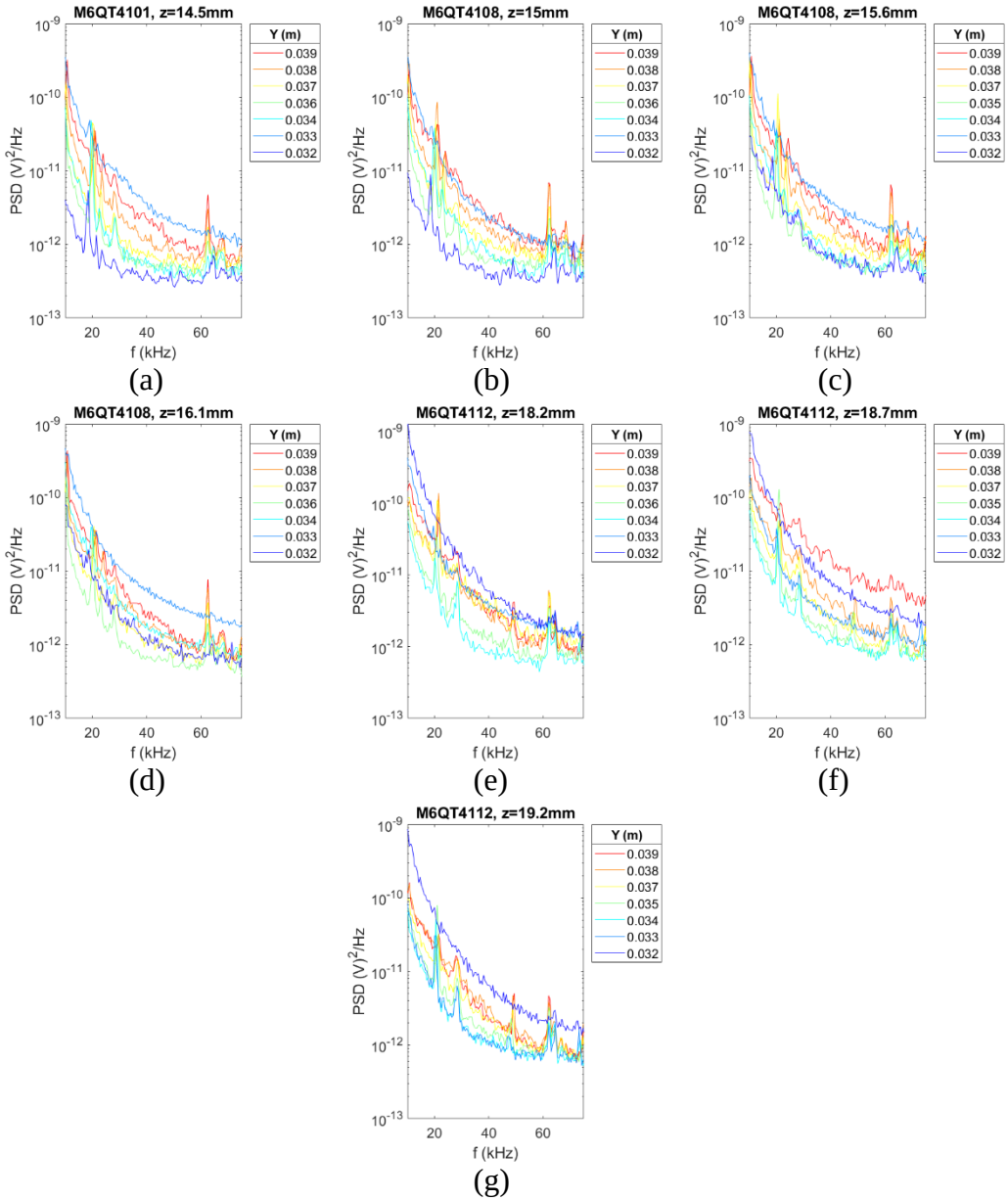

Figure 3-38. PSD spectra for z-locations (a) 14.5mm, (b) 15mm, (c) 15.6mm, (d) 16.1mm, (e) 18.2mm, (f) 18.7mm, and (g) 19.2mm.

Within the QDNS solution from the University of Minnesota and TAMU CFD, the mass flux was computed at x = 0.24 m. Calibration of the hot-wire data from Figure 3-34 into mass flux is ideal using King's Law [71]. However, it has been shown that a simple

linear fit is a result at low densities within the facilities at A&M [72]. Equation 3.2 is the general form of King's Law:

$$V_b^2 = A + B(\rho U)^n \tag{3.2}$$

Where V_b^2 is the bridge voltage, ρU is the mass flux, and *A*, *B*, and *n* are the calibration constants. For this thesis, a comparison of the bridge voltage from the experiments and the mass flux from the computations at the streamwise location of x = 0.24 m is shown in Figure 3-39. The contour colors in the experiments and computations represent the different levels of bridge voltage and mass flux, respectively. From left to right in each plot of Figure 3-39, the location and structure of the first gradual dip, the vortex, as well as the second roll-over in the experiments (middle) resembles that of the computations (top and bottom). The boundary layer edge and freestream environment locations are identical in each plot. Stated earlier, the location of content in the experiments were approximately 1 - 2 mm off from the computations and Figure 3-39 shows it. The thin boundary-layer from z = 14 - 20 mm in the figure verifies the limited amount of content observed in the hot-wire spectra in Figure 3-38. Overall, the contour mapping of the bridge voltage from the experiments and the mass flux from the computations qualitatively agree. Using the CFD as a calibration from bridge voltage to mass flux, a linear approximation of King's Law with $n \simeq 1$ is stated in Equation 3.3 where B $\simeq$ 0.3144 and A $\simeq$ 7.0759.

$$V_b^2 \simeq 0.3144(\rho U) + 7.0759 \tag{3.3}$$

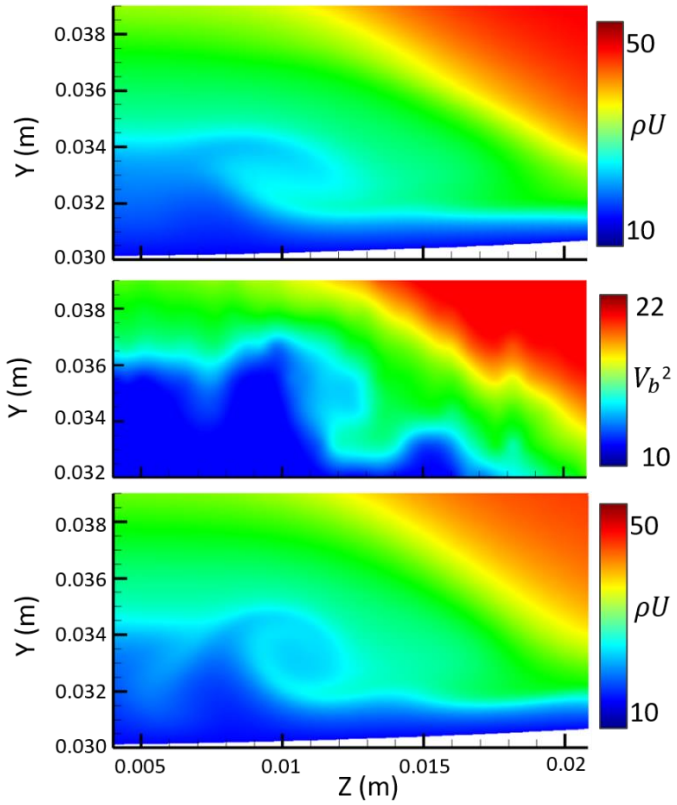

Figure 3-39. Visualization of the vortex structure between TAMU CFD in mass flux (top), the experiments in bridge voltage (middle), and Minnesota DNS in mass flux (bottom) at x=0.24m.

The off-body experiments were compared with the locations of surface heating from IR thermography at a similar Reynolds number in the M6QT. Figure 3-40 are the heat flux results at Re/m = 9.8×10^6 with flow from left to right for both images. Figure 3-40b is a zoomed-in image of the model with a yellow box signifying where hot-wire measurements were approximately taken and a blue circle pointing out the location of K9 downstream. The streak located near -10 mm in Figure 3-40b is in the region of the vortex located in the SPDMD analysis (Figure 3-39) as well as K9. This streak is also in-line with K1 and K27 (see Figure 3-1 and Figure 3-3). The PSD results from the off-centerline Kulites as well as the location with respect to the vortical mode quantitatively agree.

Similar frequencies were seen across the computations utilizing SPDMD and the experimental measurements from hot-wires and Kulites.

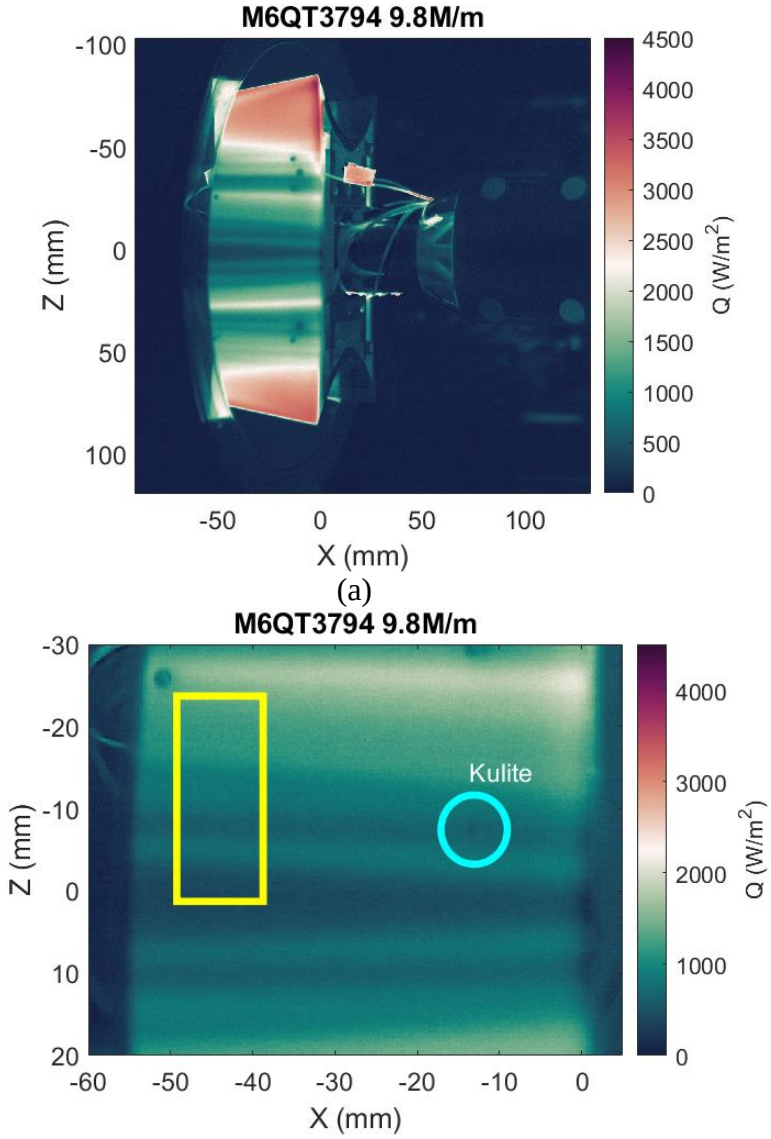

Figure 3-40. Heat flux results on the JHUAPL model at Re/m = 9.8x10^6. (a) is the entire image and (b) is a zoomed-in view referencing the location of hot-wire measurements (boxed) and K9 downstream (circled)

4. DISCUSSION AND CONCLUSIONS

The following chapter summarizes conclusions and findings in the experimental work at Texas A&M, Purdue, NASA Langley, and CUBRC of the BOLT geometry with computations from the University of Minnesota. The motivation of these studies and data are based on past and present literature, most notably wind tunnel testing of the HIFiRE-5 geometry heavily detailed in Chapter 1. Comparisons between experiments and computations are made.

4.1 The Impact of this Study

As discussed in Chapter 1, hypersonic transitional flows are complex, where the mechanisms leading to transition are configuration and environment dependent. The ability to understand these phenomena on a new and unique geometry has proven to be a challenge for aerodynamicists. Being able to predict these phenomena is an even greater challenge. The BOLT project was defined to challenge the ability of aerodynamicists to identify mechanisms and predict transition on a new and relatively complex geometry. The primary purpose of this thesis is to compare the results of computations and ground test to better predict what will occur naturally in flight on the surface of BOLT.

Comparisons were made between Purdue and A&M in quiet flow with the JHUAPL model. Purdue ran a higher Reynolds per meter of 12.4×10^6, but the same streak-like appearance is present on the model for a lower Reynolds number and with a different diagnostic. A similar comparison was made between the quiet tunnels at Purdue and TAMU with the HIFiRE-5 geometry [12-14, 16, 21, 22, 31, 32]. The heat flux results for

the inner 60% of the model at TAMU were qualitatively and quantitatively comparable with the results from Purdue. It is possible that this difference is due to noise-impingement in the TAMU facility. All quiet flow results were then compared to DNS and CFD results at wind tunnel conditions from the University of Minnesota and Texas A&M, respectively. No roughness effects were present in the simulations; thus a 'quiet' DNS was utilized. The results between the computations and experiments are consistent; the same structure on the surface of BOLT is seen in two different quiet wind tunnel facilities as well as simulations. A slice comparison verified it.

The flow features on the PEEK surface of BOLT in conventional flow compared well amongst the ACE, BAM6QT, and 20-inch Mach 6 facilities. Wedge-like structures signifying turbulence on the model were present at higher Reynolds numbers in the three different freestream environments. The structure location and Reynolds number are dependent on the freestream environment in each facility. The turbulent structure on the model in the BAM6QT is farther forward than in ACE and Langley at the same Mach and Reynolds number. This effect is consistent with higher freestream fluctuations, where the noise levels within the tunnel influence the structures on the surface. The BAM6QT contains higher freestream fluctuations when ran as a conventional facility than ACE. This freestream disturbance effect was also seen on the HIFiRE-5 geometry [11, 14, 21].

A 31% scale BOLT model was tested in ACE at lower and higher Mach numbers and was compared to CUBRC high-enthalpy results on a full-scale model. At the same Mach number and Reynolds number but full-scale with a different diagnostic, the structure on the surface in the high-enthalpy environment at CUBRC) compared qualitatively well

with the 31% scale model IR results. The same turbulent structure present on the 33% scale model is also present on the 3-D printed 31% scale model. These data show that regardless of the Mach number, Reynolds number, and facility, the same wedge-like structures are present on the surface of BOLT under conventional conditions.

Key instabilities occurred on the geometry in both conventional and quiet wind tunnel facilities. Most notably in the PSD spectra in conventional flow, a 35 kHz mode was observed in the Kulite surface pressure transducers in three different wind tunnel facilities off-centerline of the model. As the instability traveled downstream on the model, the mode grew in amplitude with an increase in Reynolds number. This effect in the Kulites within the ACE tunnel is influenced by the nozzle sidewalls transitioning, an effect previously seen by Neel et al. 2018 [16]. The PCB spectra in conventional flow did not show modal growth, but rather broadband growth. Similar results were present in other sensors. In quiet flow, the same mode was present in some of the off-centerline Kulite data with growth at higher Reynolds numbers. The lower fluctuation levels within the quiet facilities challenged the existence and modal growth in the off-centerline Kulite spectra. In quiet flow, the PCBs mounted in the aluminum surface were affected by noise in both quiet wind tunnel facilities. Similar broadband growth was observed in the PCB spectra in the M6QT.

Off-body measurements utilizing constant temperature hot-wire anemometry were made and the results proved successful in visualizing the off-body instabilities through SPDMD from the University of Minnesota. The region of interest, namely the vortical mode, is located near the off-centerline Kulites. At a streamwise location of $x = 0.24$ m

from the leading edge, the vortical mode contains a dominant frequency magnitude of 37 kHz. The spectra from the off-centerline Kulites in quiet flow also see modal growth similar to this frequency. The hot-wire off-body measurements verified this frequency range with growth from 20-40 kHz within the vortical mode in a similar location. The RMS contour plots computed from the hot-wire measurements proved reliable in referencing the location of disturbances and content within the vortical mode. The roll-up of the vortex in the experimental results compared well with the SPDMD results. Content seen within the computations of mass flux were also seen in the hot-wire experimental results. Streaks viewed on the model through IR thermography were within the vortical mode region as well as in-line with the off-centerline Kulites. With the exceptional data from the experiments, more comparisons can be made with the simulations for improved computational techniques in the future.

4.2 Future Work and Recommendations

More ground test analyses are needed to better quantify on-surface and off-body measurements on the BOLT geometry. A wider range of wind tunnel testing (higher Mach numbers, higher Reynolds numbers) of the BOLT geometry are needed to understand the full flight effects as well as the physics in the computations. More comparisons must be made between the computations and the experimental measurements, as well as a better understanding of the comparison between the two within the community. More computational analyses must be done for wind tunnel scale. Hot-wire measurements are underway to understand the vortical mode from simulations. A recommendation would be to test hot-wires in the BAM6QT to make sure no noise effects are interfering with the

measurements off the surface of BOLT in the M6QT. Non-invasive measurements off the surface of BOLT, such as planar-laser induced fluorescence (PLIF), molecular tagging velocimetry (MTV), and vibrationally excited nitric oxide monitoring (VENOM), have already begun at the NAL.

PCB sensors mounted in aluminum models have posed as a problem in wind tunnel testing, more prominently seen in quiet flow environments. Certain procedures have been introduced to carefully mitigate the noise interference from the aluminum to the PCB sensor. In previous test campaigns, Kapton tape was wrapped around the housing of the PCB before securing the sensor into models using nail polish at Purdue and TAMU, but little luck was achieved. The current configuration involved graciously coating the exterior housing of the PCB, allowing it to dry a little, installing the sensor flush with the surface, and adding extra nail polish at the backend for securement. This process proved daunting since no polish was allowed on the top surface of the PCB, otherwise the data as well as the PCB were ruined. Even though acetone is capable of removing nail polish, the chemical also ruins the coating on the top surface of the PCB that secures the sensor head. A better way to eliminate this interference is crucial for future wind tunnel testing at TAMU and other facilities.

Although nail polish is recommended for mounting PCB and Kulite surface pressure transducers (Piezotronics recommendation for PCBs [66]), with the TAMU M6QT installation process and long run times, the nail polish becomes soft where there is high heating on the model, causing the sensor to move. This effect happened mainly with the Kulite sensors near the back. Even with applying copious amounts of nail polish and

letting it dry overnight, the installation process of the model inside the quiet tunnel causes a 10-15 min heating of the model before an actual run. This is from preheating the M6QT to 430 K with no model present, then taking 10-15 min to install it in the test section. The heat radiating off the nozzle walls as well as the test section is an influence. A couple of wind tunnel runs ended with the Kulite sensor slightly protruding from the surface at the end. This is not a problem in ACE since the model is already secured to the tunnel door on the outside of the wind tunnel for quick installation ~1 min. A better material should be used to fully secure these surface pressure transducers. Piezotronics is already looking into a 132B38 sensor that is threaded into models for securement.

REFERENCES

[1] MORKOVIN, M. V., Instability, transition to turbulence and predictability, in *AGARD Fluid Dynamics Panel Symposium on "Laminar-Turbulent Transition"*. 1978: Lyngby, Denmark.

[2] REED, HELEN L. AND SARIC, WILLIAM S., Stability of Three-Dimensional Boundary Layers. *Annual Review of Fluid Mechanics*, 1989. **21**: p. 235-284 doi: 10.1146/annurev.fl.21.010189.001315.

[3] MORKOVIN, M. V., Transition in open flow systems-a reassessment. *Bulletin of the American Physical Society*, 1994. **39**(9): p. 1882.

[4] REED, HELEN L. AND SARIC, WILLIAM S., Receptivity: The Inspiration of Mark Morkovin (Invited), in *45th AIAA Fluid Dynamics Conference*. 2015, American Institute of Aeronautics and Astronautics doi: 10.2514/6.2015-2471.

[5] MACK, L. M., Boundary-layer linear stability theory. *In AGARD Special Course on Stability and Transition of Laminar Flow*, 1984. **709**: p. 31-81.

[6] FEDOROV, ALEXANDER, Transition and Stability of High-Speed Boundary Layers. *Annual Review of Fluid Mechanics*, 2011. **43**(1): p. 79-95 doi: 10.1146/annurev-fluid-122109-160750.

[7] ZHONG, XIAOLIN AND WANG, XIAOWEN, Direct Numerical Simulation on the Receptivity, Instability, and Transition of Hypersonic Boundary Layers. *Annual Review of Fluid Mechanics*, 2012. **44**(1): p. 527-561 doi: 10.1146/annurev-fluid-120710-101208.

[8] POGGIE, J. AND KIMMEL, R., Traveling instabilities in elliptic cone boundary-layer transition at Mach 8, in *36th AIAA Aerospace Sciences Meeting and Exhibit*. 1998, American Institute of Aeronautics and Astronautics doi: 10.2514/6.1998-435.

[9] BALAKUMAR, PONNAMPALAM AND OWENS, LEWIS, Stability of Hypersonic Boundary Layers on a Cone at an Angle of Attack, in *40th Fluid Dynamics Conference and Exhibit*. 2010 doi: 10.2514/6.2010-4718.

[10] DINZL, DEREK J. AND CANDLER, GRAHAM V., Direct Numerical Simulation of Crossflow Instability Excited by Microscale Roughness on HIFiRE-5, in *54th AIAA Aerospace Sciences Meeting*. 2016, American Institute of Aeronautics and Astronautics doi: 10.2514/6.2016-0353.

[11] JULIANO, THOMAS J., BORG, MATTHEW P., AND SCHNEIDER, STEVEN P., Quiet Tunnel Measurements of HIFiRE-5 Boundary-Layer Transition. *AIAA Journal*, 2015. **53**(4): p. 832-846 doi: 10.2514/1.J053189.

[12] BORG, MATTHEW P., KIMMEL, ROGER L., AND STANFIELD, SCOTT, Traveling Crossflow Instability for HIFiRE-5 in a Quiet Hypersonic Wind Tunnel, in *43rd Fluid Dynamics Conference*. 2013, American Institute of Aeronautics and Astronautics doi: 10.2514/6.2013-2737.

[13] BORG, MATTHEW P., KIMMEL, ROGER L., HOFFERTH, JERROD W., BOWERSOX, RODNEY D., AND MAI, CHI L., Freestream Effects on Boundary Layer Disturbances for HIFiRE-5, in *53rd AIAA Aerospace Sciences Meeting*. 2015, American Institute of Aeronautics and Astronautics doi: 10.2514/6.2015-0278.

[14] BORG, MATTHEW P. AND KIMMEL, ROGER L., Simultaneous Infrared and Pressure Measurements of Crossflow Instability Modes for HIFiRE-5, in *54th AIAA Aerospace Sciences Meeting*. 2016, American Institute of Aeronautics and Astronautics doi: 10.2514/6.2016-0354.

[15] BORG, MATTHEW P. AND KIMMEL, ROGER L., Measurements of Crossflow Instability Modes for HIFiRE-5 at Angle of Attack, in *55th AIAA Aerospace Sciences Meeting*. 2017, American Institute of Aeronautics and Astronautics doi: 10.2514/6.2017-1681.

[16] NEEL, IAN T., LEIDY, ANDREW, TICHENOR, NATHAN R., AND BOWERSOX, RODNEY D., Influence of Environmental Disturbances on Hypersonic Crossflow Instability on the HIFiRE-5 Elliptic Cone, in *2018 AIAA Aerospace Sciences Meeting*. 2018, American Institute of Aeronautics and Astronautics doi: 10.2514/6.2018-1821.

[17] CORKE, THOMAS C. AND BOWERSOX, RODNEY D., Hypersonic Boundary Layer Cross Flow Transition - Characteristics and Control, in *2018 AIAA Aerospace Sciences Meeting*. 2018, American Institute of Aeronautics and Astronautics doi: 10.2514/6.2018-0352.

[18] SARIC, WILLIAM AND REED, HELEN, Crossflow Instabilities - Theory & Technology, in *41st Aerospace Sciences Meeting and Exhibit*. 2003, American Institute of Aeronautics and Astronautics doi: 10.2514/6.2003-771.

[19] POGGIE, JONATHAN, KIMMEL, ROGER L., AND SCHWOERKE, STEPHEN N., Traveling Instability Waves in a Mach 8 Flow over an Elliptic Cone. *AIAA Journal*, 2000. **38**(2): p. 251-258 doi: 10.2514/2.979.

[20] LI, FEI, CHOUDHARI, MEELAN, CHANG, CHAU-LYAN, WHITE, JEFFERY, KIMMEL, ROGER, ADAMCZAK, DAVID, BORG, MATTHEW, STANFIELD, SCOTT, AND SMITH, MARK, Stability Analysis for HIFiRE Experiments, in *42nd AIAA Fluid Dynamics*

Conference and Exhibit. 2012, American Institute of Aeronautics and Astronautics doi: 10.2514/6.2012-2961.

[21] NEEL, IAN T., LEIDY, ANDREW, AND BOWERSOX, RODNEY D., Preliminary Study of the Effect of Environmental Disturbances on Hypersonic Crossflow Instability on the HIFiRE-5 Elliptic Cone, in *55th AIAA Aerospace Sciences Meeting*. 2017, American Institute of Aeronautics and Astronautics doi: 10.2514/6.2017-0767.

[22] NEEL, IAN T., LEIDY, ANDREW, TICHENOR, NATHAN R., AND BOWERSOX, RODNEY, Characterization of Environmental Disturbances on Hypersonic Crossflow Instability on the HIFiRE-5 Elliptic Cone, in *22nd AIAA International Space Planes and Hypersonics Systems and Technologies Conference*. 2018, American Institute of Aeronautics and Astronautics doi: 10.2514/6.2018-5375.

[23] HOLDEN, MICHAEL, WADHAMS, TIMOTHY, MACLEAN, MATTHEW, AND MUNDY, ERIK, Reviews of Studies of Boundary Layer Transition in Hypersonic Flows Over Axisymmetric and Elliptic Cones Conducted in the CUBRC Shock Tunnels, in *47th AIAA Aerospace Sciences Meeting including The New Horizons Forum and Aerospace Exposition*. 2009, American Institute of Aeronautics and Astronautics doi: 10.2514/6.2009-782.

[24] BERGER, KAREN, RUFER, SHANN, KIMMEL, ROGER, AND ADAMCZAK, DAVID, Aerothermodynamic Characteristics of Boundary Layer Transition and Trip Effectiveness of the HIFiRE Flight 5 Vehicle, in *39th AIAA Fluid Dynamics Conference*. 2009, American Institute of Aeronautics and Astronautics doi: 10.2514/6.2009-4055.

[25] JULIANO, THOMAS AND SCHNEIDER, STEVEN, Instability and Transition on the HIFiRE-5 in a Mach 6 Quiet Tunnel, in *40th Fluid Dynamics Conference and Exhibit*. 2010, American Institute of Aeronautics and Astronautics doi: 10.2514/6.2010-5004.

[26] KIMMEL, ROGER L., POGGIE, JONATHAN, AND SCHWOERKE, STEPHEN N., Laminar-Turbulent Transition in a Mach 8 Elliptic Cone Flow. *AIAA Journal*, 1999. **37**(9): p. 1080-1087 doi: 10.2514/2.836.

[27] JULIANO, THOMAS J., PAQUIN, LAURA, AND BORG, MATTHEW P., Measurement of HIFiRE-5 Boundary-Layer Transition in a Mach-6 Quiet Tunnel with Infrared Thermography, in *54th AIAA Aerospace Sciences Meeting*. 2016, American Institute of Aeronautics and Astronautics doi: 10.2514/6.2016-0595.

[28] JULIANO, THOMAS J., PAQUIN, LAURA A., AND BORG, MATTHEW P., HIFiRE-5 Boundary-Layer Transition Measured in a Mach-6 Quiet Tunnel with Infrared Thermography. *AIAA Journal*, 2019. **57**(5): p. 2001-2010 doi: 10.2514/1.J056750.

[29] BORG, MATTHEW P. AND KIMMEL, ROGER L., Ground Test of Transition for HIFiRE-5b at Flight-Relevant Attitudes. *Journal of Spacecraft and Rockets*, 2018. **55**(6): p. 1329-1340 doi: 10.2514/1.A34163.

[30] BORG, MATTHEW P. AND KIMMEL, ROGER L., Ground Test Measurements of Boundary-Layer Instabilities and Transition for HIFiRE-5 at Flight-Relevant Attitudes, in *47th AIAA Fluid Dynamics Conference*. 2017, American Institute of Aeronautics and Astronautics doi: 10.2514/6.2017-3135.

[31] BORG, MATTHEW P., KIMMEL, ROGER L., AND STANFIELD, SCOTT, Traveling Crossflow Instability for the HIFiRE-5 Elliptic Cone. *Journal of Spacecraft and Rockets*, 2015. **52**(3): p. 664-673 doi: 10.2514/1.A33145.

[32] NEEL, IAN T. Influence of Environmental Disturbances on Hypersonic Crossflow Instability on the HIFiRE-5 Elliptic Cone. PhD dissertation. 2019 Texas A&M University, College Station, TX.

[33] KOCIAN, TRAVIS S., MOYES, ALEXANDER, MULLEN, DANIEL, AND REED, HELEN L., PSE and Spatial Biglobal Instability Analysis of Reduced Scale and Flight HIFiRE-5 Geometry, in *55th AIAA Aerospace Sciences Meeting*. 2017, American Institute of Aeronautics and Astronautics doi: 10.2514/6.2017-0768.

[34] KIMMEL, ROGER L., ADAMCZAK, DAVID W., BORG, MATTHEW P., JEWELL, JOSEPH S., JULIANO, THOMAS J., STANFIELD, SCOTT, AND BERGER, KAREN T., HIFiRE-1 and -5 Flight and Ground Tests, in *2018 AIAA Aerospace Sciences Meeting*. 2018, American Institute of Aeronautics and Astronautics doi: 10.2514/6.2018-0056.

[35] KIMMEL, ROGER L., ADAMCZAK, DAVID W., BORG, MATTHEW P., JEWELL, JOSEPH S., JULIANO, THOMAS J., STANFIELD, SCOTT A., AND BERGER, KAREN T., First and Fifth Hypersonic International Flight Research Experimentation's Flight and Ground Tests. *Journal of Spacecraft and Rockets*, 2018. **56**(2): p. 421-431 doi: 10.2514/1.A34287.

[36] LAKEBRINK, MATTHEW T. AND BORG, MATTHEW P., Traveling Crossflow Wave Predictions on the HIFiRE-5 at Mach 6: Stability Analysis vs. Quiet Tunnel Data, in *54th AIAA Aerospace Sciences Meeting*. 2016, American Institute of Aeronautics and Astronautics doi: 10.2514/6.2016-0356.

[37] TUFTS, MATTHEW W., BORG, MATTHEW P., GOSSE, RYAN C., AND KIMMEL, ROGER L., Collaboration Between Flight Test, Ground Test, and Computation on HIFiRE-5, in *2018 Applied Aerodynamics Conference*. 2018, American Institute of Aeronautics and Astronautics doi: 10.2514/6.2018-3807.

[38] THOME, JOHN, DWIVEDI, ANUBHAV, NICHOLS, JOSEPH W., AND CANDLER, GRAHAM V., Direct numerical simulation of BOLT hypersonic flight vehicle, in

2018 Fluid Dynamics Conference. 2018, American Institute of Aeronautics and Astronautics doi: 10.2514/6.2018-2894.

[39] MULLEN, CHARLES D., MOYES, ALEXANDER, KOCIAN, TRAVIS S., AND REED, HELEN L., Heat Transfer and Boundary-Layer Stability Analysis of Subscale BOLT and the Fin Cone, in *AIAA Aviation 2019 Forum*. 2019, American Institute of Aeronautics and Astronautics doi: 10.2514/6.2019-3081.

[40] MOYES, ALEXANDER, KOCIAN, TRAVIS S., MULLEN, CHARLES D., AND REED, HELEN L., Pre-Flight Boundary-Layer Stability Analysis of BOLT Geometry, in *2018 Fluid Dynamics Conference*. 2018, American Institute of Aeronautics and Astronautics doi: 10.2514/6.2018-2895.

[41] MOYES, ALEXANDER AND REED, HELEN L., Nonlinear Boundary-Layer Stability Analysis of BOLT and HIFiRE-5, in *AIAA Aviation 2019 Forum*. 2019, American Institute of Aeronautics and Astronautics doi: 10.2514/6.2019-2972.

[42] THOME, JOHN, KNUTSON, ANTHONY, AND CANDLER, GRAHAM V., Boundary layer instabilities on BoLT subscale geometry, in *AIAA Scitech 2019 Forum*. 2019, American Institute of Aeronautics and Astronautics doi: 10.2514/6.2019-0092.

[43] KNUTSON, ANTHONY L., THOME, JOHN S., AND CANDLER, GRAHAM V., Numerical Simulation of Instabilities in the Boundary-Layer Transition Experiment Flowfield, in *Journal of Spacecraft and Rockets*. 2019. p. 1-10 doi: 10.2514/1.A34599.

[44] BERRIDGE, DENNIS C., MCKIERNAN, GREGORY, WADHAMS, TIM P., HOLDEN, MICHAEL, WHEATON, BRADLEY M., WOLF, THOMAS D., AND SCHNEIDER, STEVEN P., Hypersonic Ground Tests In Support of the Boundary Layer Transition (BOLT) Flight Experiment, in *2018 Fluid Dynamics Conference*. 2018, American Institute of Aeronautics and Astronautics doi: 10.2514/6.2018-2893.

[45] BERRIDGE, DENNIS C., KOSTAK, HEATHER E., MCKIERNAN, GREGORY R., WHEATON, BRADLEY M., WOLF, THOMAS D., AND SCHNEIDER, STEVEN P., Hypersonic Ground Tests With High-Frequency Instrumentation In Support of the Boundary Layer Transition (BOLT) Flight Experiment, in *AIAA Scitech 2019 Forum*. 2019, American Institute of Aeronautics and Astronautics doi: 10.2514/6.2019-0090.

[46] KOSTAK, HEATHER E., BOWERSOX, RODNEY D., MCKIERNAN, GREGORY R., THOME, JOHN, CANDLER, GRAHAM V., AND KING, RUDOLPH A., Freestream Disturbance Effects on Boundary Layer Instability and Transition on the AFOSR BOLT Geometry, in *AIAA Scitech 2019 Forum*. 2019, American Institute of Aeronautics and Astronautics doi: 10.2514/6.2019-0088.

[47] KOSTAK, HEATHER AND BOWERSOX, RODNEY D., Hypersonic Boundary Layer Off-Body and Surface Measurements on the AFOSR BOLT Geometry, in *AIAA Scitech 2020 Forum*. 2020, American Institute of Aeronautics and Astronautics doi: 10.2514/6.2020-1043.

[48] LEIDY, ANDREW N. An Experimental Characterization of 3-D Transitional Shock Wave Boundary Layer Interactions at Mach 6. PhD dissertation. 2019 Texas A&M University, College Station, TX.

[49] HOFFERTH, JERROD, BOWERSOX, RODNEY, AND SARIC, WILLIAM, The Mach 6 Quiet Tunnel at Texas A&M: Quiet Flow Performance, in *27th AIAA Aerodynamic Measurement Technology and Ground Testing Conference*. 2010, American Institute of Aeronautics and Astronautics doi: 10.2514/6.2010-4794.

[50] BLANCHARD, ALAN E., LACHOWICZ, JASON T., AND WILKINSON, STEPHEN P., NASA Langley Mach 6 Quiet Wind-Tunnel Performance. *AIAA Journal*, 1997. **35**(1): p. 23-28 doi: 10.2514/2.82.

[51] SARIC, W. S., Görtler Vortices. *Annual Review of Fluid Mechanics*, 1994. **26**(1): p. 379-409 doi: 10.1146/annurev.fl.26.010194.002115.

[52] CRAIG, STUART A. Stability of High-Speed, Three-Dimensional Boundary Layers. PhD dissertation. 2015 Texas A&M University, College Station, TX.

[53] HOFFERTH, JERROD AND SARIC, WILLIAM, Boundary-Layer Transition on a Flared Cone in the Texas A&M Mach 6 Quiet Tunnel, in *50th AIAA Aerospace Sciences Meeting including the New Horizons Forum and Aerospace Exposition*. 2012, American Institute of Aeronautics and Astronautics doi: 10.2514/6.2012-923.

[54] HOFFERTH, JERROD W. Boundary-Layer Stability and Transition on a Flared Cone in a Mach 6 Quiet Wind Tunnel. PhD dissertation. 2013 Texas A&M University, College Station, TX.

[55] TICHENOR, NATHAN RYAN. Characterization of the Influence of a Favorable Pressure Gradient on the Basic Structure of a Mach 5.0 High Reynolds Number Supersonic Turbulent Boundary Layer. PhD dissertation. 2010 Texas A&M University, College Station, TX.

[56] SEMPER, MICHAEL, PRUSKI, BRANDON, AND BOWERSOX, RODNEY, Freestream Turbulence Measurements in a Continuously Variable Hypersonic Wind Tunnel, in *50th AIAA Aerospace Sciences Meeting including the New Horizons Forum and Aerospace Exposition*. 2012, American Institute of Aeronautics and Astronautics doi: 10.2514/6.2012-732.

[57] MAI, CHI LUONG NHAT. Near-region modification of total pressure fluctuations by a normal shock wave in a low-density hypersonic wind tunnel. PhD dissertation. 2014 Texas A&M University, College Station, TX.

[58] STEEN, LAURA-CHERI E. Characterization and development of nozzles for a hypersonic quiet wind tunnel. MS thesis. 2010 Purdue University, West Lafayette, IN.

[59] SWEENEY, CAMERON J. Characterization of a hypersonic quiet wind tunnel nozzle. MS thesis. 2016 Purdue University, West Lafayette, IN.

[60] BERGER, KAREN T., HOLLINGSWORTH, KEVIN E., WRIGHT, SHELIA A., AND RUFER, SHANN J., NASA Langley Aerothermodynamics Laboratory: Hypersonic Testing Capabilities, in *53rd AIAA Aerospace Sciences Meeting*. 2015, American Institute of Aeronautics and Astronautics doi: 10.2514/6.2015-1337.

[61] WADHAMS, TIM, MACLEAN, MATTHEW, AND HOLDEN, MICHAEL, Continuing Experimental Studies of High Speed Boundary Layer Transition in LENS Facilities to Further the Development of Predictive Tools for Boundary Layer Transition in Flight, in *51st AIAA Aerospace Sciences Meeting including the New Horizons Forum and Aerospace Exposition*. 2013, American Institute of Aeronautics and Astronautics doi: 10.2514/6.2013-379.

[62] BOYD, C. F. AND HOWELL, A., Numerical investigation of one-dimensional heat-flux calculations. 1994: NAVAL SURFACE WARFARE CENTER DAHLGREN DIC SILVER SPRING MD.

[63] HUBNER, J. P., CARROLL, B. F., AND SCHANZE, K. S., Heat-Transfer Measurements in Hypersonic Flow Using Luminescent Coating Techniques. *Journal of Thermophysics and Heat Transfer*, 2002. **16**(4): p. 516-522 doi: 10.2514/2.6726.

[64] LIU, TIANSHU AND SULLIVAN, JOHN P., Pressure and Temperature Sensitive Paints. Experimental Fluid Mechanics. 2005, Germany: Springer-Verlag Berlin Heidelberg.

[65] BERESH, STEVEN J., HENFLING, JOHN F., SPILLERS, RUSSELL W., AND PRUETT, BRIAN O. M., Fluctuating wall pressures measured beneath a supersonic turbulent boundary layer. *Physics of Fluids*, 2011. **23**(7): p. 075110 doi: 10.1063/1.3609271.

[66] ORT, DAVID AND DOSCH, JEFFREY J., Influence of Mounting on the Accuracy of Piezoelectric Pressure Measurements for Hypersonic Boundary Layer Transition, in *AIAA Scitech 2019 Forum*. 2019, American Institute of Aeronautics and Astronautics doi: 10.2514/6.2019-2292.

[67] CRAIG, STUART A. AND SARIC, WILLIAM S., Experimental study of crossflow instability on a Mach 6 yawed cone, in *45th AIAA Fluid Dynamics Conference*. 2015, American Institute of Aeronautics and Astronautics doi: 10.2514/6.2015-2774.

[68] SUBBAREDDY, PRAMOD K. AND CANDLER, GRAHAM V., A fully discrete, kinetic energy consistent finite-volume scheme for compressible flows. *Journal of Computational Physics*, 2009. **228**(5): p. 1347-1364 doi: 10.1016/j.jcp.2008.10.026.

[69] SULLIVAN, JOHN, SCHNEIDER, STEVEN, LIU, TIANSHU, RUBAL, JUSTIN, WARD, CHRIS, DUSSLING, JOSEPH, RICE, CODY, FOLEY, RYAN, CAI, ZEMIN, WANG, BO, AND WOODIGA, SUDESH, Quantitative Global Heat Transfer in a Mach-6 Quiet Tunnel. NASA Langley Research Center, Technical Report CR-2012-217331. 2012, Hampton, VA.

[70] KNUTSON, ANTHONY, GS, SIDHARTH, AND CANDLER, GRAHAM V., Instabilities in Mach 6 Flow over a Cone with a Swept Fin, in *2018 Fluid Dynamics Conference*. 2018, American Institute of Aeronautics and Astronautics doi: 10.2514/6.2018-3071.

[71] BRUUN, H. H., Hot wire anemometry : principles and signal analysis. 1995, New York: Oxford Unversity Press.

[72] SEMPER, MICHAEL THOMAS. Examining a Hypersonic Turbulent Boundary Layer at Low Reynolds Number. PhD dissertation. 2013 Texas A&M University, College Station, TX.

APPENDIX A

PAST RUN CONFIGURATIONS OF BOLT

Many wind tunnel run experiments led to the final data analyzed in this thesis at TAMU. The first campaign of the 33% JHUAPL model produced amazing IR results, but the pressure transducers contained an abundance of noise. Due to a limited amount of days with the wind tunnel model for the first campaign, not enough time was present to aid with the noise interference. The first surface pressure spectra from the first campaign will not be included in this thesis due to unreliable results. M6QT3455 IR results will not be included.

Run #	Date	Tunnel	Notes	Sensor Placement	Diagnostics
3300	1/25/2018	ACE	Re/m = $2.3x10^6$ – $6.9x10^6$	-	SC8100
3304	1/28/2018	ACE	Re/m = $2.5x10^6$ – $8.3x10^6$	-	SC8100
3307	2/13/2018	M6QT	Re/m = $9x10^6$-$12x10^6$	-	SC8100
3446	4/30/2018	ACE	Re/m = $3x10^6$ – $7.8x10^6$	K1 K6 P8 K9 P11 K12 P20 P22 P25	SC8100, PCBs, Kulites
3448	4/30/2018	ACE	Re/m = $3.2x10^6$ – $8.3x10^6$	K1 K6 P8 K9 P11 K12 P20 P22 P25	SC8100, PCBs, Kulites
3450	4/30/2018	M6QT	Re/m = $9.3x10^6$ – $11.5x10^6$, Re/m = $11.5x10^6$ – $5.4x10^6$, Lost K9	K1 K6 P8 K9 P11 K12 P20 P22 P25	SC8100, PCBs, Kulites
3451	5/2/2018	M6QT	Re/m = $11x10^6$ – $11.7x10^6$, Re/m = $11.8x10^6$ – $5.3x10^6$	K2 K4 K10 K12 P16 P19 P23 P24 P28	SC8100, PCBs, Kulites
3452	5/2/2018	ACE	Re/m = $3.1x10^6$ – $8.3x10^6$	K2 K4 K10 K12 P16 P19 P23 P24 P28	SC8100, PCBs, Kulites
3453	5/2/2018	ACE	Re/m = $3.2x10^6$ – $7.9x10^6$	K3 K5 K7 P14 P17 P21 P26 P29	SC8100, PCBs, Kulites
3454	5/2/2018	M6QT	Re/m = $10x10^6$ – $11.7x10^6$, Re/m = $11.7x10^6$ – $5.4x10^6$	K3 K5 K7 P14 P17 P21 P26 P29	SC8100, PCBs, Kulites
3455	5/4/2018	M6QT	Re/m = $10x10^6$ – $11.7x10^6$, Re/m = $11.7x10^6$ – $5.5x10^6$ Bleed valves opened halfway	K9 K13 P15 P20 P23 P24 P26 K27	SC8100, PCBs, Kulites

Run #	Date	Tunnel	Notes	Sensor Placement	Diagnostics
			during tunnel ramp down of Reynolds number		
3456	5/4/2018	ACE	Re/m = $2.8x10^6$ – $7.9x10^6$	K9 K13 P15 P20 P23 P24 P26 K27	SC8100, PCBs, Kulites
3457	5/4/2018	M6QT	Re/m = $9.7x10^6$ – $11.7x10^6$, Re/m = $11.7x10^6$ – $5.6x10^6$	K18 P24 K27 K30 P32 P33 P34 P35	SC8100, PCBs, Kulites

APPENDIX B

RUN CONFIGURATIONS OF BOLT

TAMU received the 33% JHUAPL scale model again for completion of this thesis. All IR and surface pressure transducer measurements were repeated. The 33% TAMU model was used for hot-wires measurements.

Run #	Date	Tunnel	Notes	Sensor Placement	Diagnostics
3687	1/31/2019	ACE	Re/m = $2.9x10^6$ – $7.4x10^6$ Checking diagnostics, checking calibration of camera, checking PCB and Kulite instrumentation – noise present in PCBs with flow off on both PEEK and aluminum side	K1 K2 P8 P11 P25 P26 P28	SC8100 PCBs, Kulites
3689	2/1/2019	ACE	Re/m = $3.4x10^6$ – $8x10^6$ Checking diagnostics, checking PCB and Kulite instrumentation – noise is still present in PCBS with flow off on both PEEK and aluminum side	K1 K2 P8 P11 P25 P26 P28	SC8100, PCBs, Kulites
3690_{test} – 3725_{test}	2/4/2019 – 2/18/2019	benchtop	Testing different cables for PCBs, testing grounding of wires, testing sensor filters with function generator inputs, testing length of cables to DAQ, testing interference with facility heaters, testing PCB boxes close to and far from DAQ, testing power input to PCB boxes – PCB 7709 is not giving correct output (more noisy than others) – testing different input/output configurations for PCBs plugged into DAQ, testing low-pass 500 kHz filter in replace of 1 MHz filter for PCB 7629 and PCB 7705	K1 K2 P8 P11 P25 P26 P28	SC8100, PCBs, Kulites

Run #	Date	Tunnel	Notes	Sensor Placement	Diagnostics
3703	3/6/2019	ACE	Re/m = $3x10^6$ – $6.6x10^6$ DAQ system for data was full, so no PCB and Kulite data past $6.6x10^6$	K1 K2 P8 P11 P25 P26	SC8100, PCBs, Kulites
3706	3/7/2019	ACE	Re/m = $2.3x10^6$ – $6.6x10^6$ Started at a lower Reynolds number. P14 and P15 had odd noise interference that was seen in previous campaign.	K4 K12 P14 P15 P19 P29	SC8100, PCBs, Kulites
3710	3/11/2019	ACE	Re/m = $2.3x10^6$ – $6.6x10^6$ After numerous test cases of the PCBs, it was discovered that the IR camera on backup battery influenced noise in the PCBs! All runs hereafter had IR camera on normal power.	K4 K12 P14 P15 P19 P29	SC8100, PCBs, Kulites
3713	3/12/2019	ACE	Re/m = $2.3x10^6$ – $6.9x10^6$ PCB 7707 was not working prior to run, so P21 disregarded.	K5 K7 P16 P20 ~~P21~~ P24	SC8100, PCBs, Kulites
3715	3/13/2019	ACE	Re/m = $2.3x10^6$ – $7.3x10^6$ Due to flawed design of the wind tunnel model, PCBs 17 and 22 may protrude above surface.	K6 K9 P17 P22 P28 P32	SC8100, PCBs, Kulites
3717	3/13/2019	ACE	Re/m = $2.4x10^6$ – $7x10^6$	K3 K10 P23 P31 P33 P34	SC8100, PCBs, Kulites
3720	3/18/2019	ACE	Re/m = $2.3x10^6$ – $7.6x10^6$	K13 K18 **P21**	SC8100, PCBs, Kulites
3722	3/18/2019	ACE	Re/m = $2.2x10^6$ – $7.2x10^6$	K27 K30	SC8100, PCBs, Kulites
3794	6/21/2019	M6QT	Re/m = $7.9x10^6$ – $10.5x10^6$ May have interference in PCBs	K27 K30 P8 P11 P25 P26	SC8100, PCBs, Kulites
3799	6/24/2019	M6QT	Re/m = $7.9x10^6$ – $12x10^6$ K4 gave weird results. Interference in PCBs	K3 K4 P14 P15 P19 P29	SC8100, PCBs, Kulites
3814	7/9/2019	M6QT	Re/m = $8.1x10^6$ – $12x10^6$ Brand new sensors installed	K2 K27 K30 P8 P11 P14 P15 P32	SC8100, PCBs, Kulites
3815	7/10/2019	M6QT	Re/m = $7.9x10^6$ – $11.6x10^6$	K1 K4 K12 P15 P19 P26 P31 P33	SC8100, PCBs, Kulites

Run #	Date	Tunnel	Notes	Sensor Placement	Diagnostics
3816	7/11/2019	M6QT	Re/m = $7.9x10^6$ – $11.6x10^6$	K5 K7 K9 P16 P20 P21 P24 P29	SC8100, PCBs, Kulites
3820	7/12/2019	M6QT	Re/m = $7.8x10^6$ – $11.6x10^6$	K3 K6 K10 P15 P17 P22 P28 P34	SC8100, PCBs, Kulites
3824	7/13/2019	M6QT	Re/m = $7.7x10^6$ – $11.7x10^6$	K13 K18 P23 P24 P25 P29 P35	SC8100, PCBs, Kulites
4015	11/6/2019	M6QT	Re/m = $9.9x10^6$ Hot-wire	Z = 8.6mm Y = 32-35 mm	TSI 1220-PI2.5(A)
4016	11/6/2019	M6QT	Re/m = $9.8x10^6$ Hot-wire	Z = 8.7mm Y = 32-35 mm	TSI 1220-PI2.5(A)
4017	11/6/2019	M6QT	Re/m = $9.7x10^6$ Hot-wire	Z = 8.5mm Y = 32-35 mm	TSI 1220-PI2.5(B)
4018	11/6/2019	M6QT	Re/m = $9.7x10^6$ Hot-wire	Z = 8.8mm Y = 32-35 mm	TSI 1220-PI2.5(B)
4019	11/6/2019	M6QT	Re/m = $9.7x10^6$ Hot-wire	Z = 8.2mm Y = 32-35 mm	TSI 1220-PI2.5(B)
4020	11/6/2019	M6QT	Re/m = $9.7x10^6$ Hot-wire	Z = 8.6mm Y = 32-40 mm	TSI 1220-PI2.5(B)
4022	11/7/2019	M6QT	Re/m = $9.6x10^6$ Hot-wire	Z = 5.5-6.9mm Y = 32-37 mm	TSI 1220-PI2.5(B)
4023	11/7/2019	M6QT	Re/m = $9.6x10^6$ Hot-wire	Z = 7.4-8.8mm Y = 32-37 mm	TSI 1220-PI5
4098	01/23/2020	M6QT	Re/m = $9.9x10^6$ Hot-wire	Z = 8.7-9.8mm Y = 32-39 mm	TSI 1220-PI2.5(C)
4099	01/23/2020	M6QT	Re/m = $9.9x10^6$ Hot-wire	Z = 10.3-11.4mm Y = 32-39 mm	TSI 1220-PI2.5(C)
4100	01/24/2020	M6QT	Re/m = $9.8x10^6$ Hot-wire	Z = 11.9-12.9mm Y = 32-39 mm	TSI 1220-PI2.5(C)
4101	01/24/2020	M6QT	Re/m = $9.9x10^6$ Hot-wire	Z = 13.5-14.5mm Y = 32-39 mm	TSI 1220-PI2.5(C)
4103	01/27/2020	M6QT	Re/m = $9.9x10^6$ Hot-wire	Z = 7.2-8.2mm Y = 32-39 mm	TSI 1220-PI2.5(C)
4104	01/27/2020	M6QT	Re/m = $9.8x10^6$ Hot-wire	Z = 5.6-6.6mm Y = 32-39 mm	TSI 1220-PI2.5(C)
4105	01/27/2020	M6QT	Re/m = $9.9x10^6$ Hot-wire	Z = 4-5.1mm Y = 32-39 mm	TSI 1220-PI2.5(C)
4108	01/28/2020	M6QT	Re/m = $9.9x10^6$ Hot-wire	Z = 15-16.1mm Y = 32-39 mm	TSI 1220-PI2.5(C)
4109	01/28/2020	M6QT	Re/m = $9.9x10^6$ Hot-wire	Z = 16.6-17.7mm Y = 32-39 mm	TSI 1220-PI2.5(C)
4112	01/29/2020	M6QT	Re/m = $9.9x10^6$ Hot-wire	Z = 18.2-19.2mm Y = 32-39 mm	TSI 1220-PI2.5(C)
4113	01/29/2020	M6QT	Re/m = $9.9x10^6$ Hot-wire	Z = 19.8-20.8mm Y = 32-39 mm	TSI 1220-PI2.5(C)

APPENDIX C

HEAT FLUX RESULTS CONVENTIONAL FLOW

Heat flux results for several conventional wind tunnel runs in ACE with the BOLT model are located here. Flow is from left to right. Colorbar is in W/m^2. Above each image is the designated wind tunnel run number and corresponding Reynolds number.

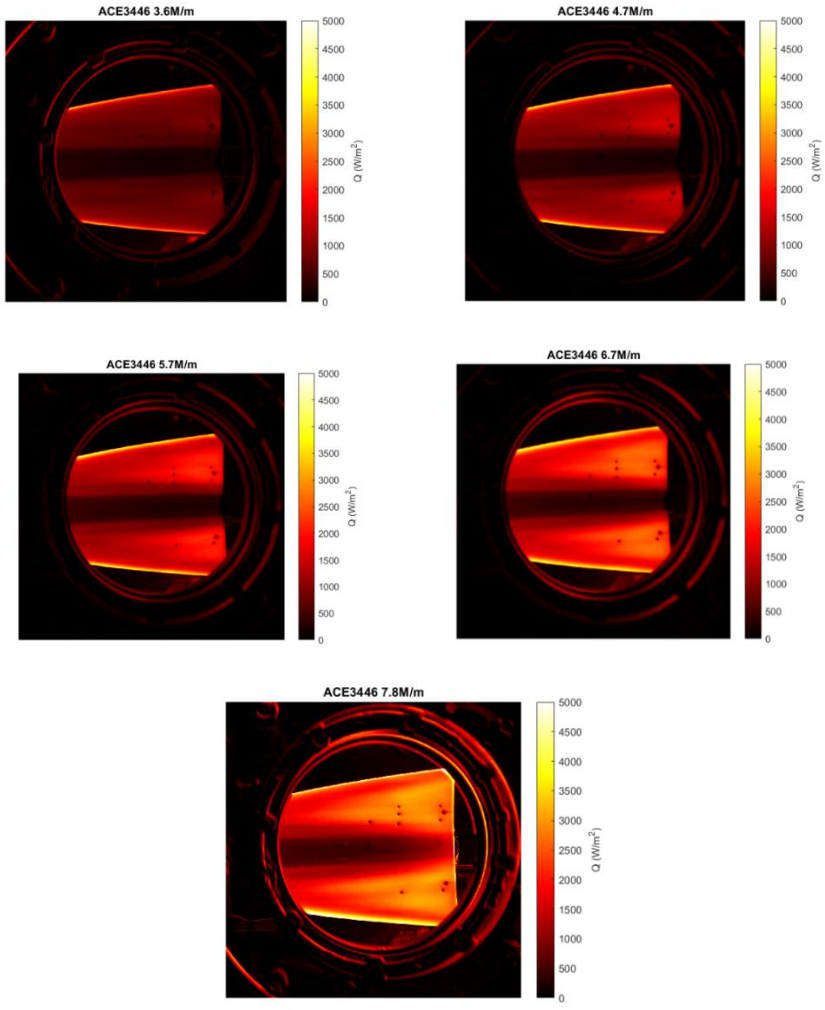

Figure C-1. ACE 3446 Reynolds number sweep, 33% scale machined JHUAPL model, heat flux results

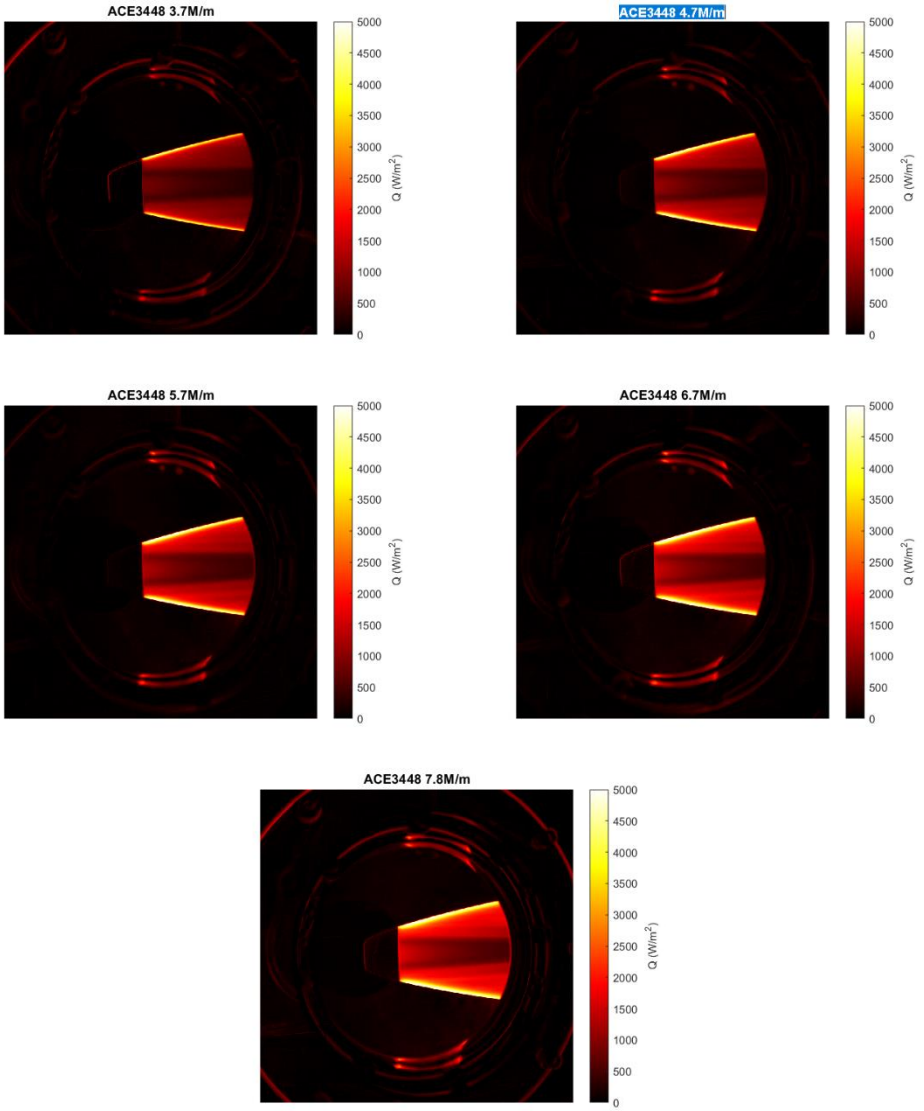

Figure C-2. ACE 3448 Reynolds number sweep, 33% scale machined JHUAPL model, heat flux results

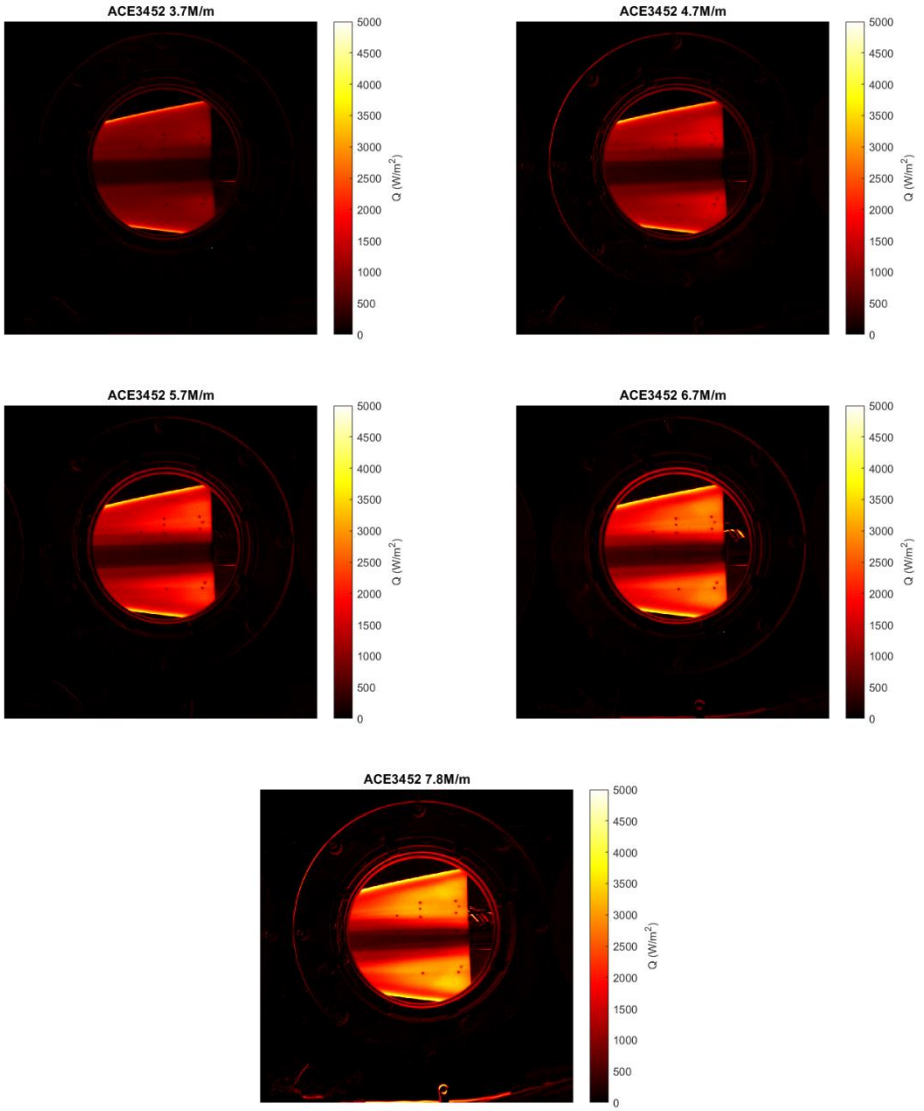

Figure C-3. ACE 3452 Reynolds number sweep, 33% scale machined JHUAPL model, heat flux results

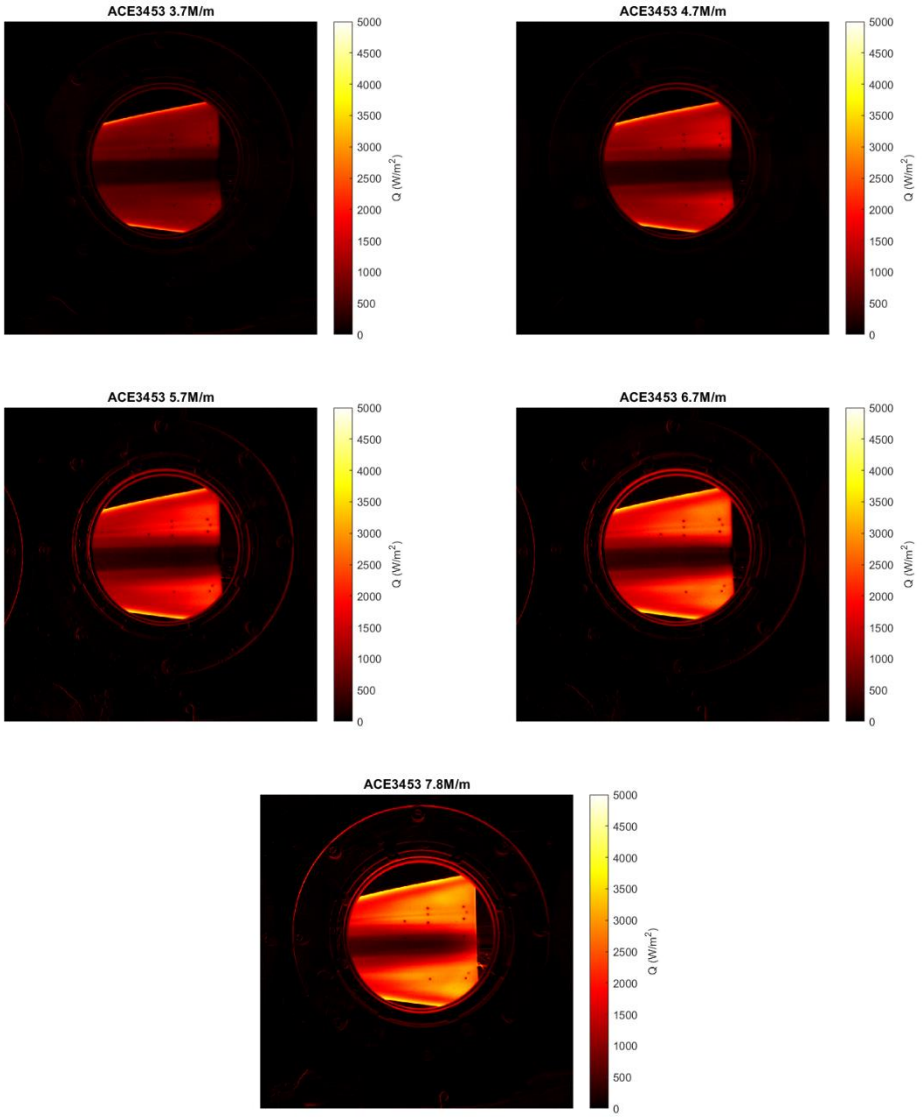

Figure C-4. ACE 3453 Reynolds number sweep, 33% scale machined JHUAPL model, heat flux results

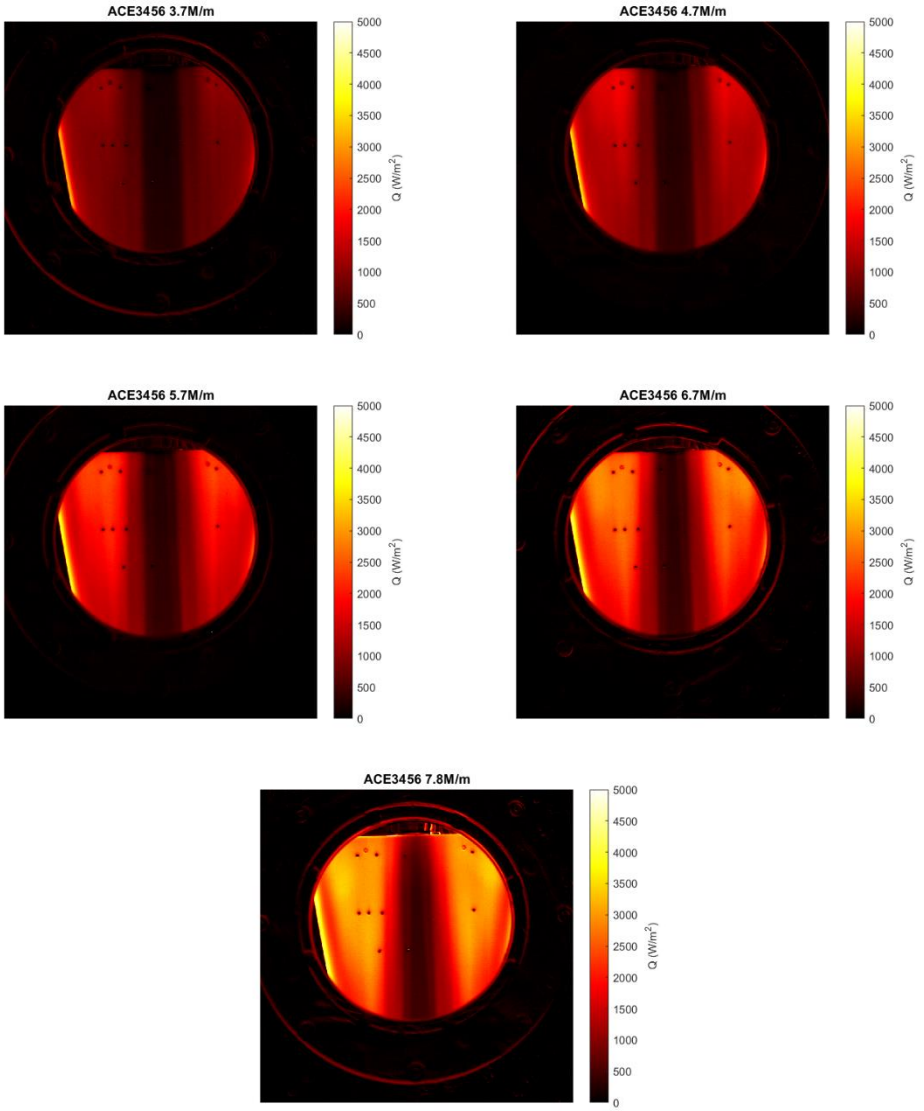

Figure C-5. ACE 3456 Reynolds number sweep, 33% scale machined JHUAPL model, flow is from bottom to top, heat flux results

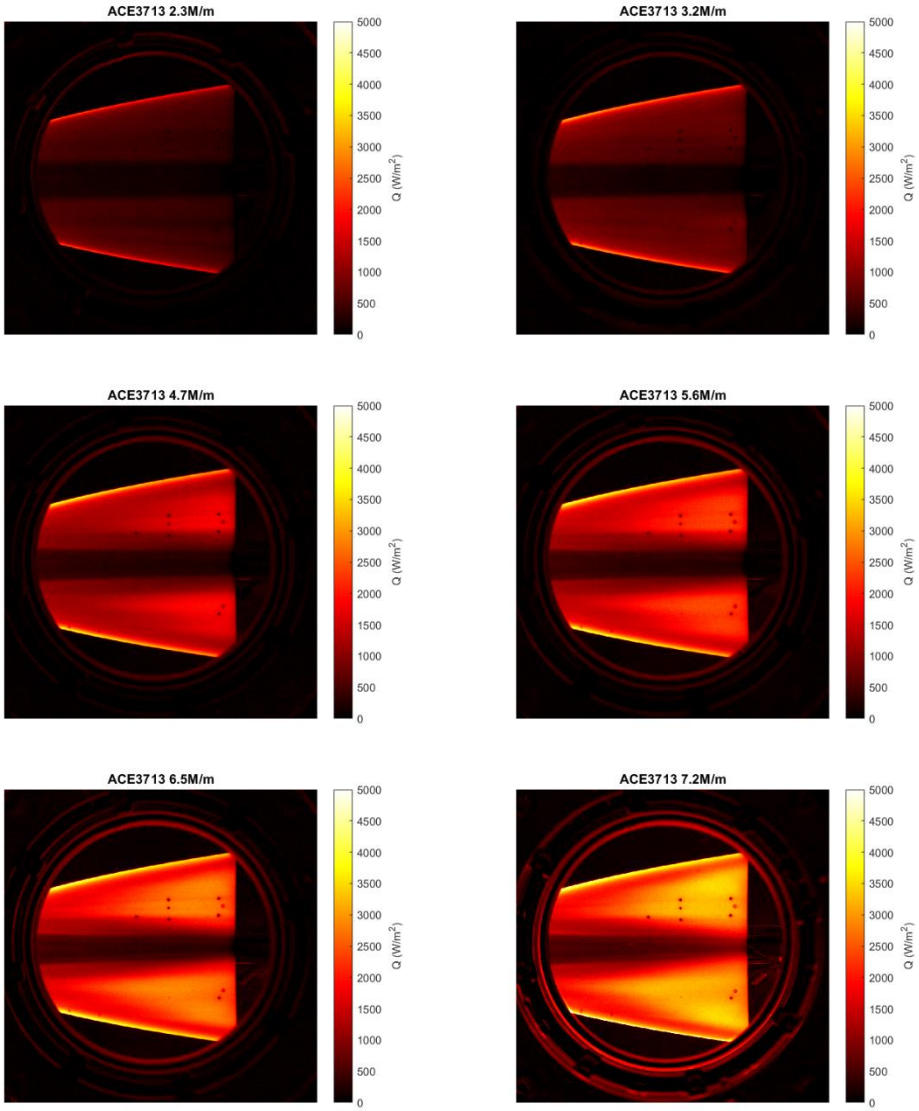

Figure C-6. ACE 3713 Reynolds number sweep, 33% scale machined JHUAPL model, heat flux results

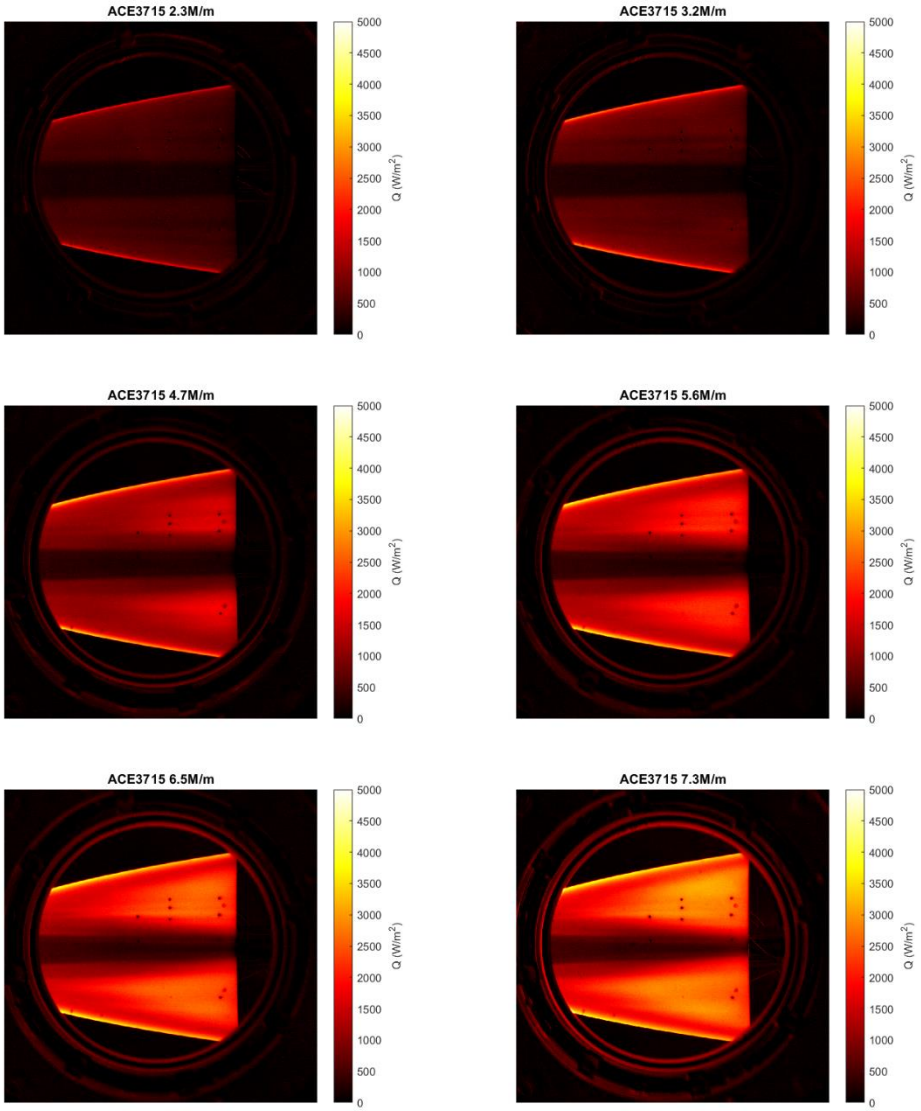

Figure C-7. ACE 3715 Reynolds number sweep, 33% scale machined JHUAPL model, heat flux results

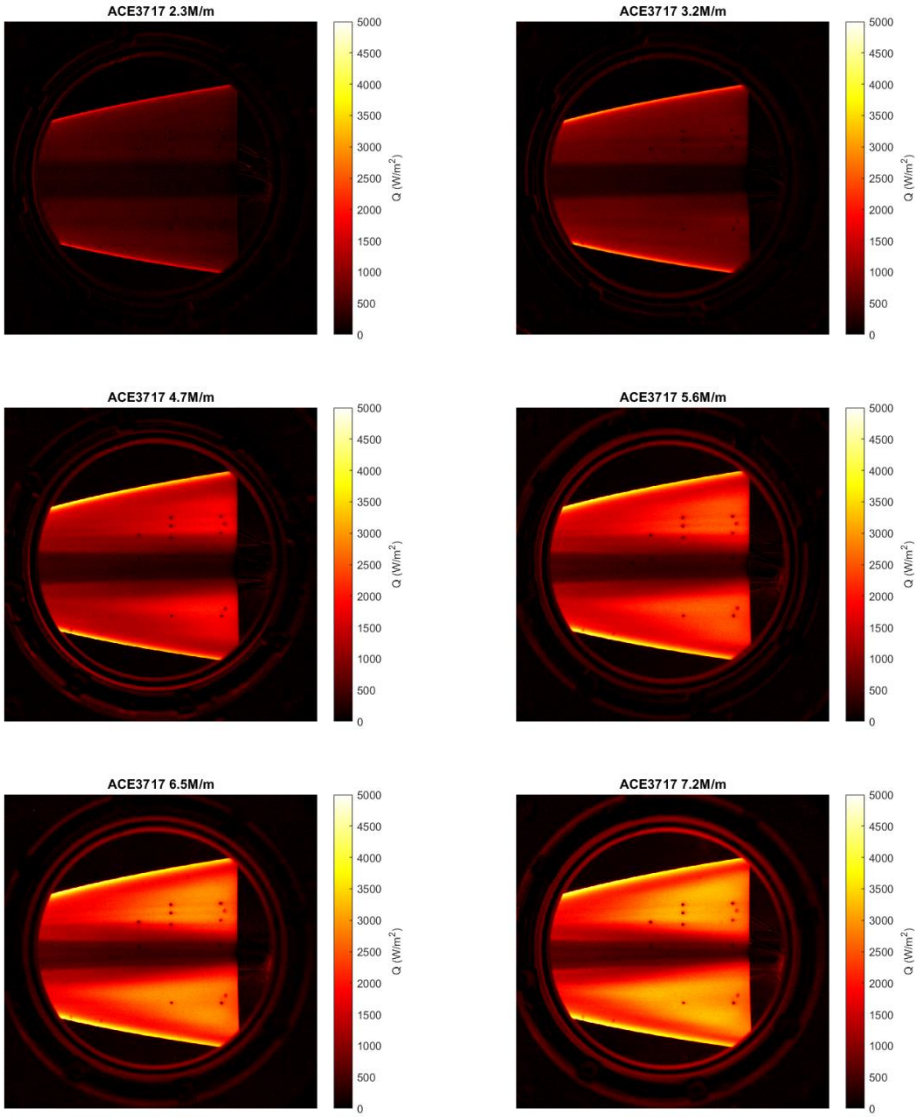

Figure C-8. ACE3717 Reynolds number sweep, 33% scale machined JHUAPL model, heat flux results

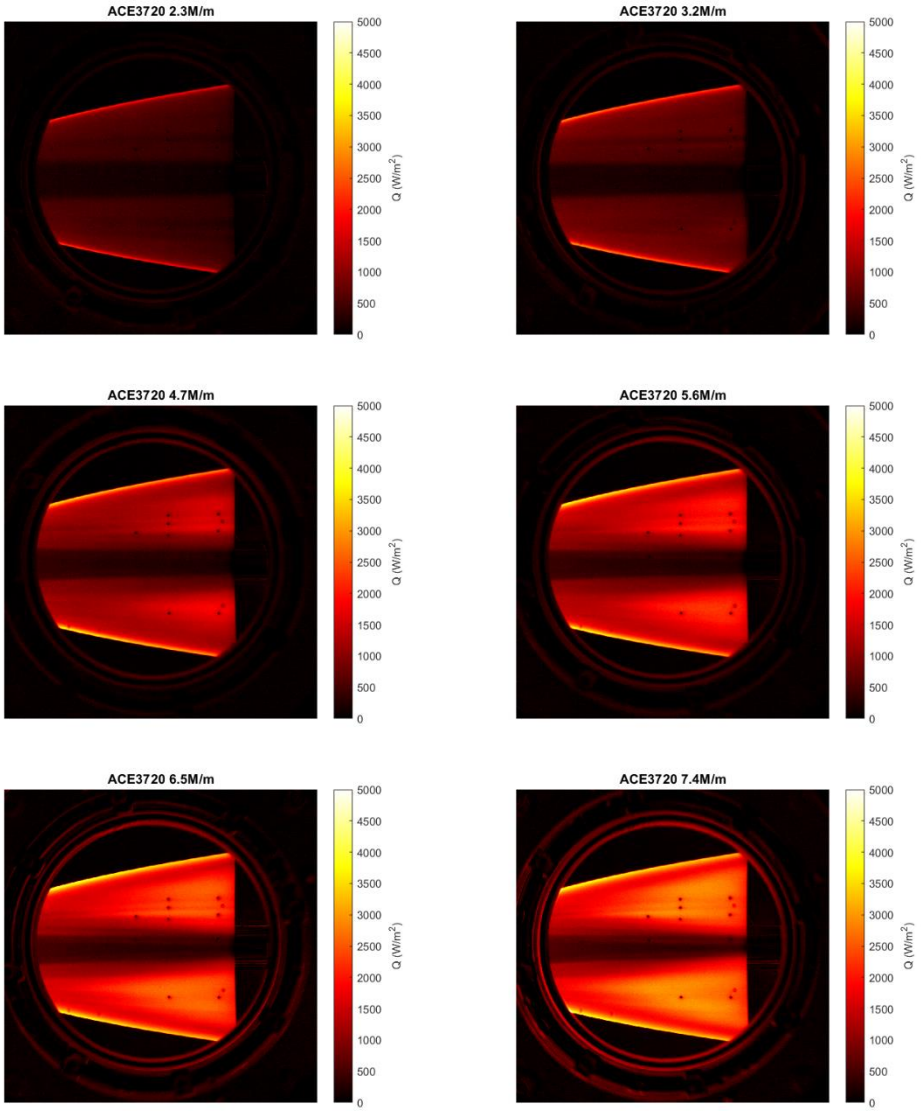

Figure C-9. ACE3720 Reynold number sweep, 33% scale machined JHUAPL model, heat flux results

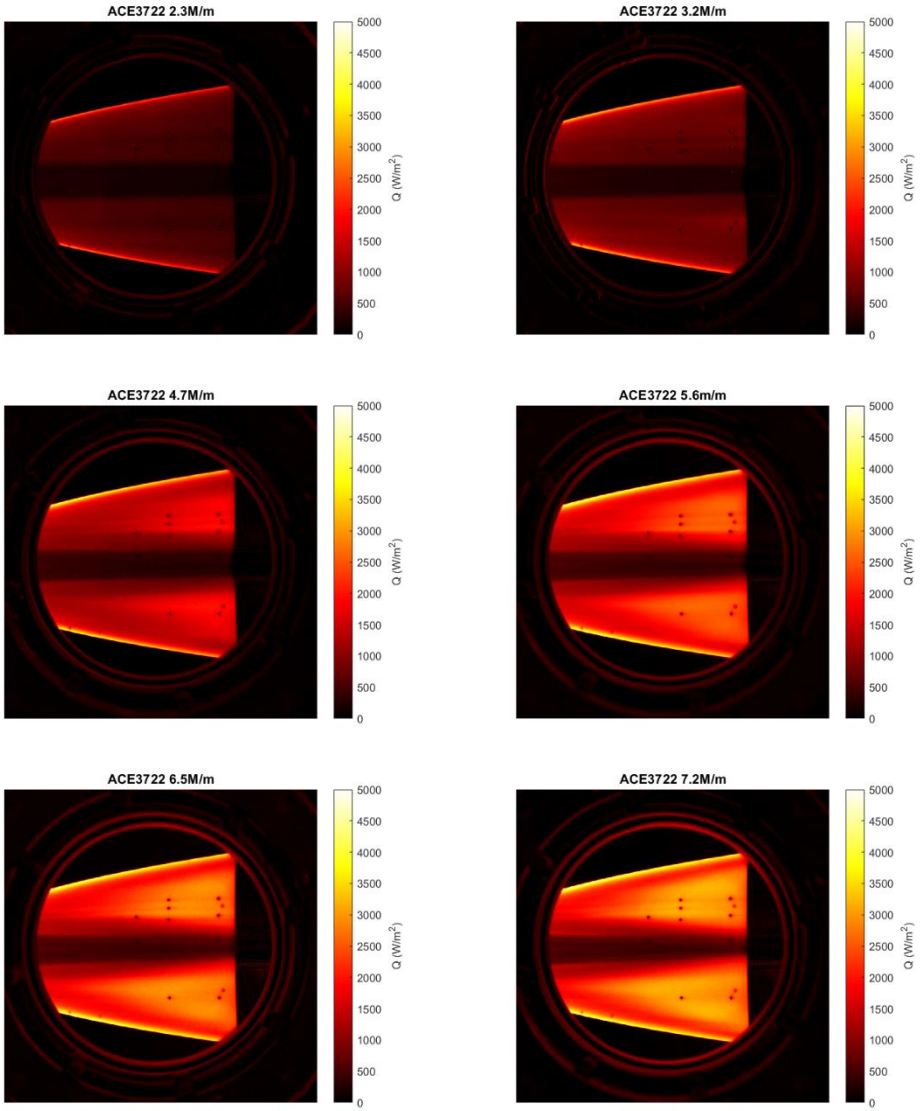

Figure C-10. ACE3722 Reynolds number sweep, 33% scale machined JHUAPL model, heat flux results

APPENDIX D

HEAT FLUX RESULTS QUIET FLOW

Heat flux results for several quiet wind tunnel runs in the M6QT with the BOLT model. Flow is from left to right. Colorbar is in W/m^2. Above each image is the designated wind tunnel run number and corresponding Reynolds number.

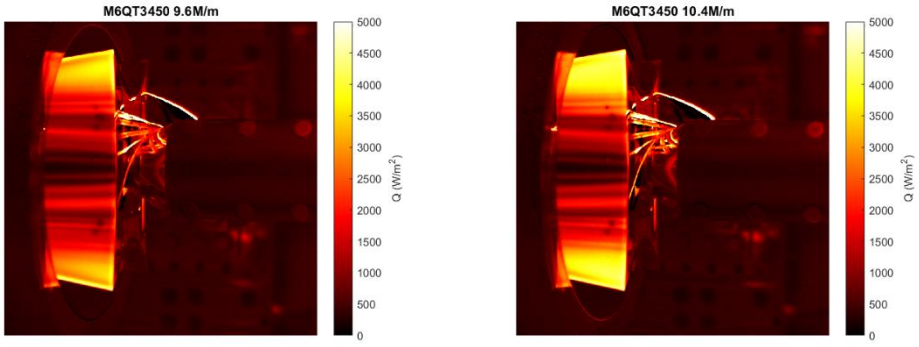

Figure D-1. M6QT3450 Reynolds number sweep, 33% scale machined JHUAPL model, heat flux results

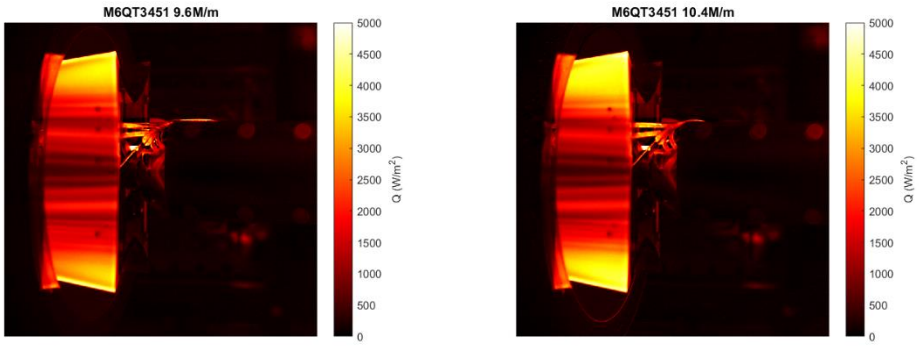

Figure D-2. M6QT3451 Reynolds number sweep, 33% scale machined JHUAPL model, heat flux results

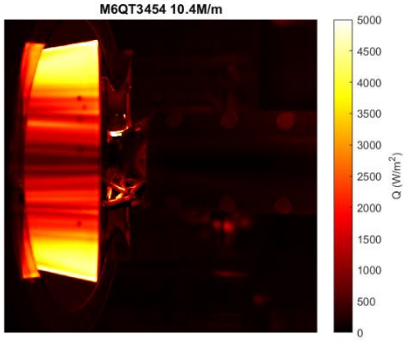

Figure D-3. M6QT3454 Reynolds number sweep, 33% scale machined JHUAPL model, heat flux results

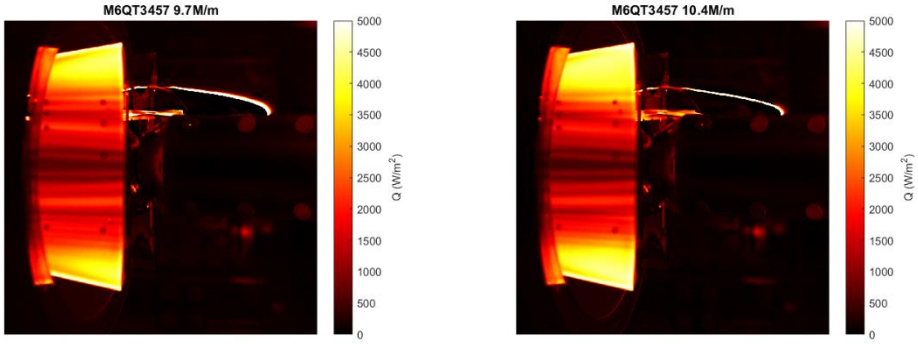

Figure D-4. M6QT3457 Reynolds number sweep, 33% scale machined JHUAPL model, heat flux results

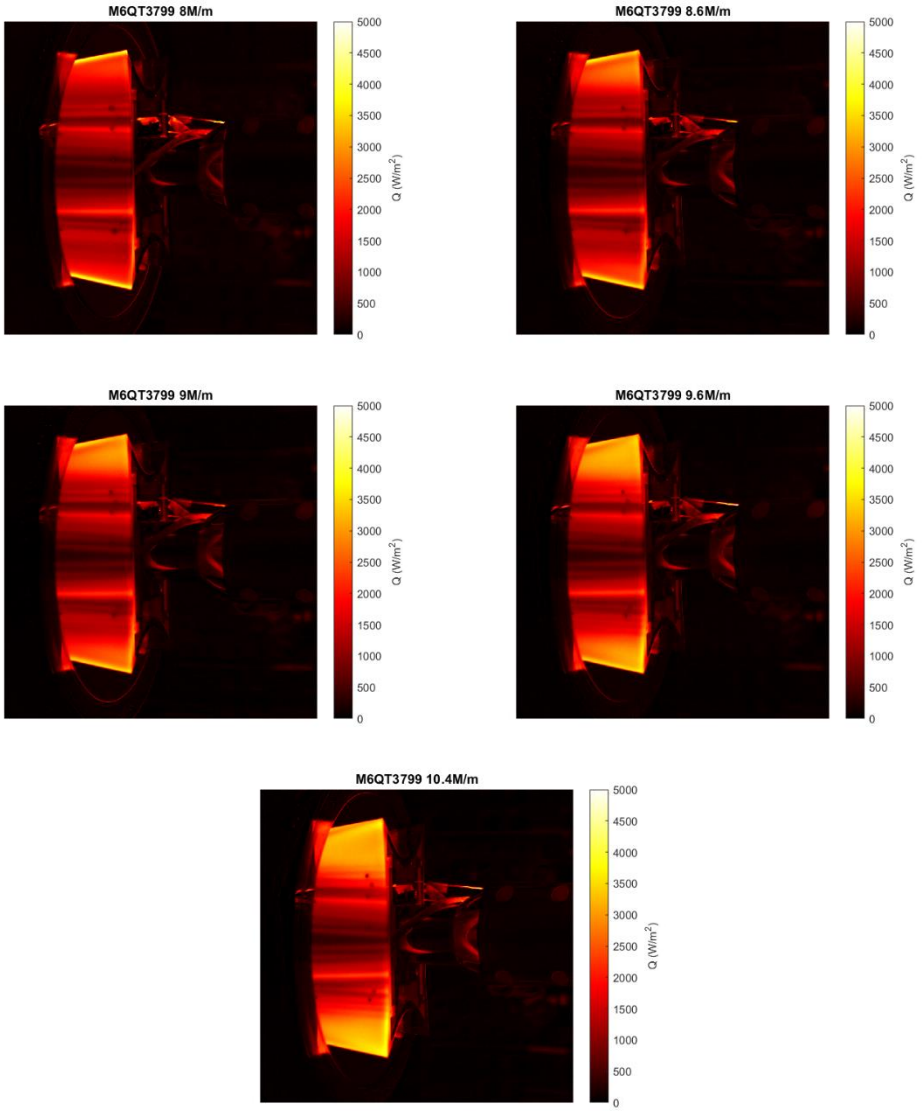

Figure D-5. M6QT3799 Reynolds number sweep, 33% scale machined JHUAPL model, heat flux results

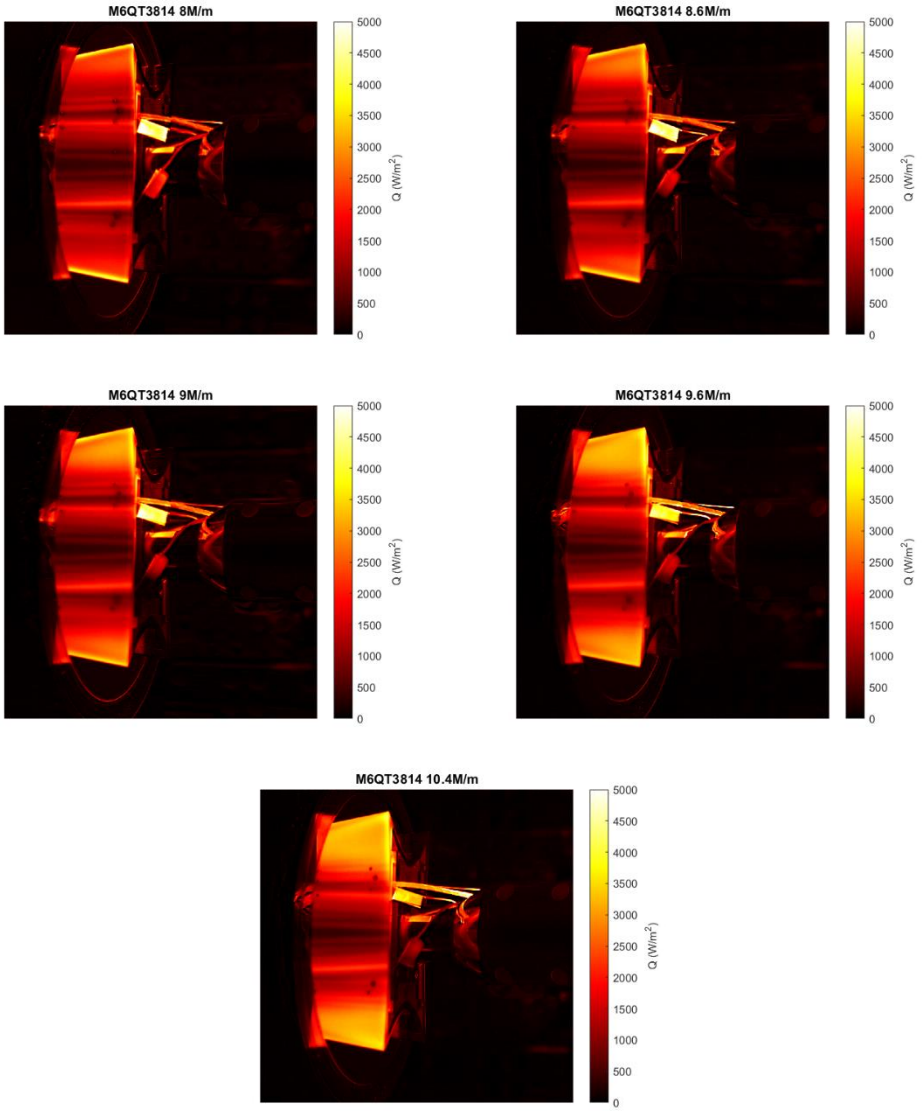

Figure D-6. M6QT3814 Reynolds number sweep, 33% scale machined JHUAPL model, heat flux results

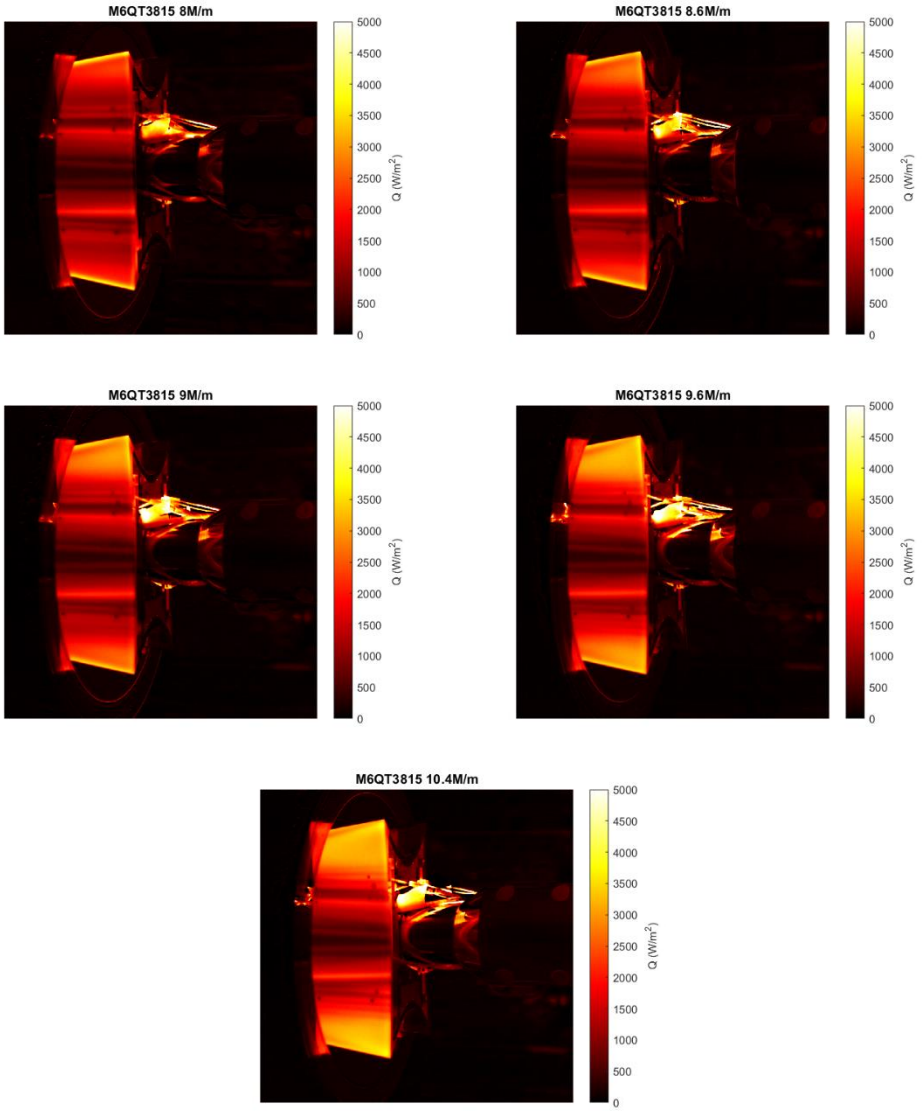

Figure D-7. M6QT3815 Reynolds number sweep, 33% scale machined JHUAPL model, heat flux results

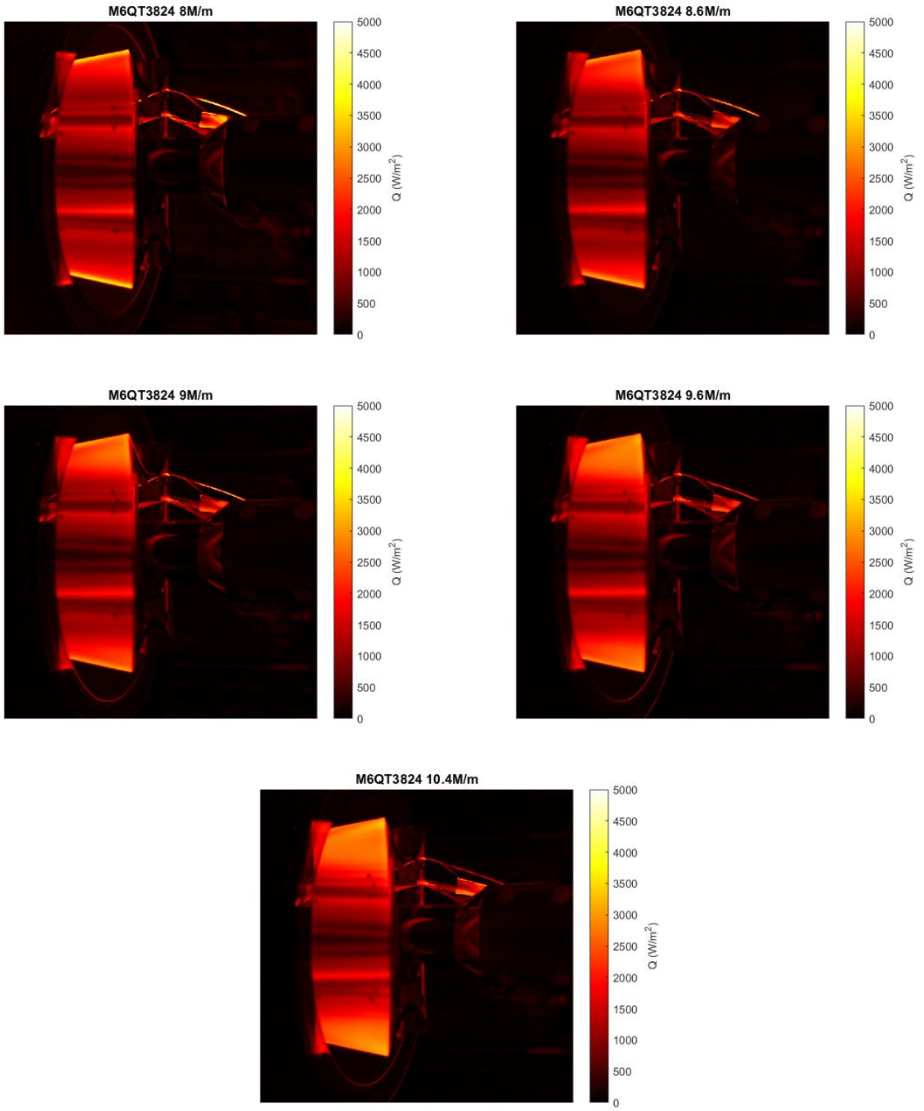

Figure D-8. M6QT3824 Reynolds number sweep, 33% scale machined JHUAPL model, heat flux results

APPENDIX E

SURFACE PRESSURE SPECTRA (CONVENTIONAL)

Surface pressure transducer data from TAMU, Purdue, and NASA Langley for conventional flow. Some measurements were not taken in each facility. Plots from Chapter 3 are repeated here for completeness of all 35 sensors. The results are labeled in sensor number order.

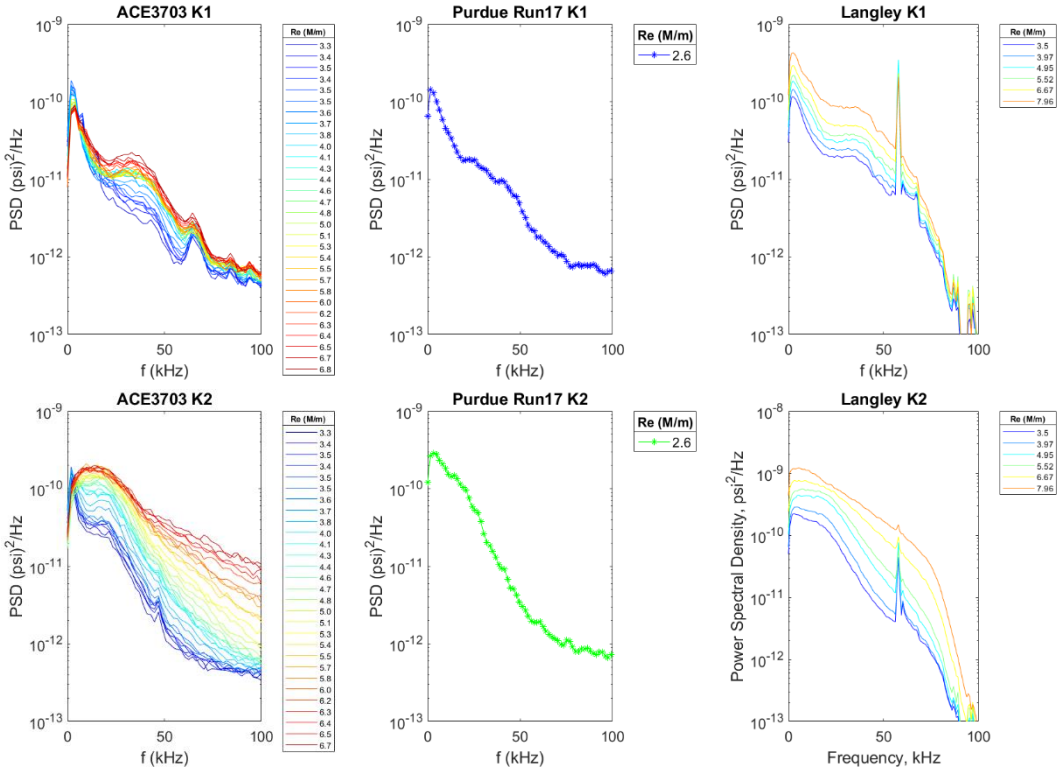

Figure E-1. Surface pressure spectra for every sensor located on JHUAPL BOLT 33% scale model; conventional flow

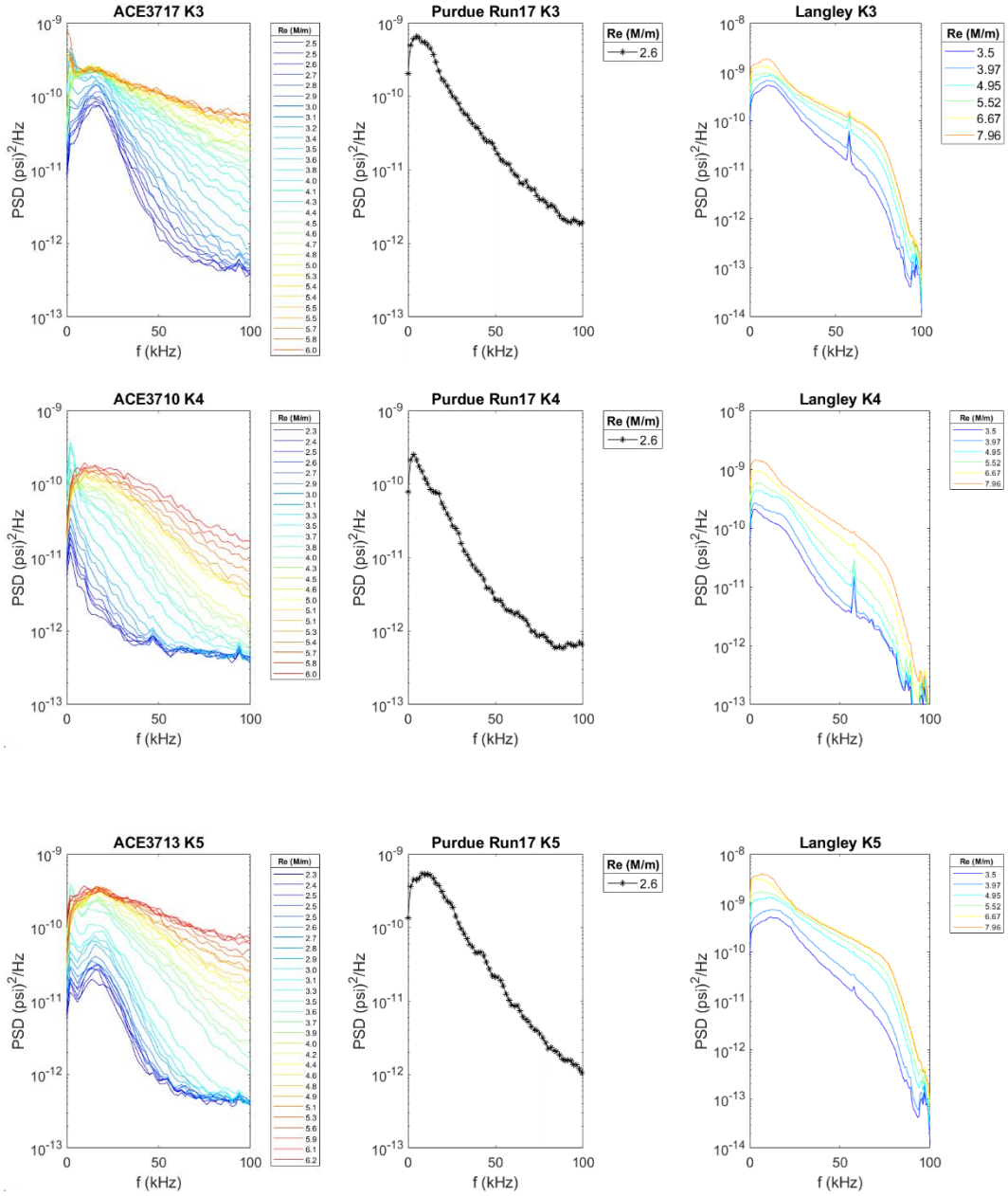

Figure E-1. Continued.

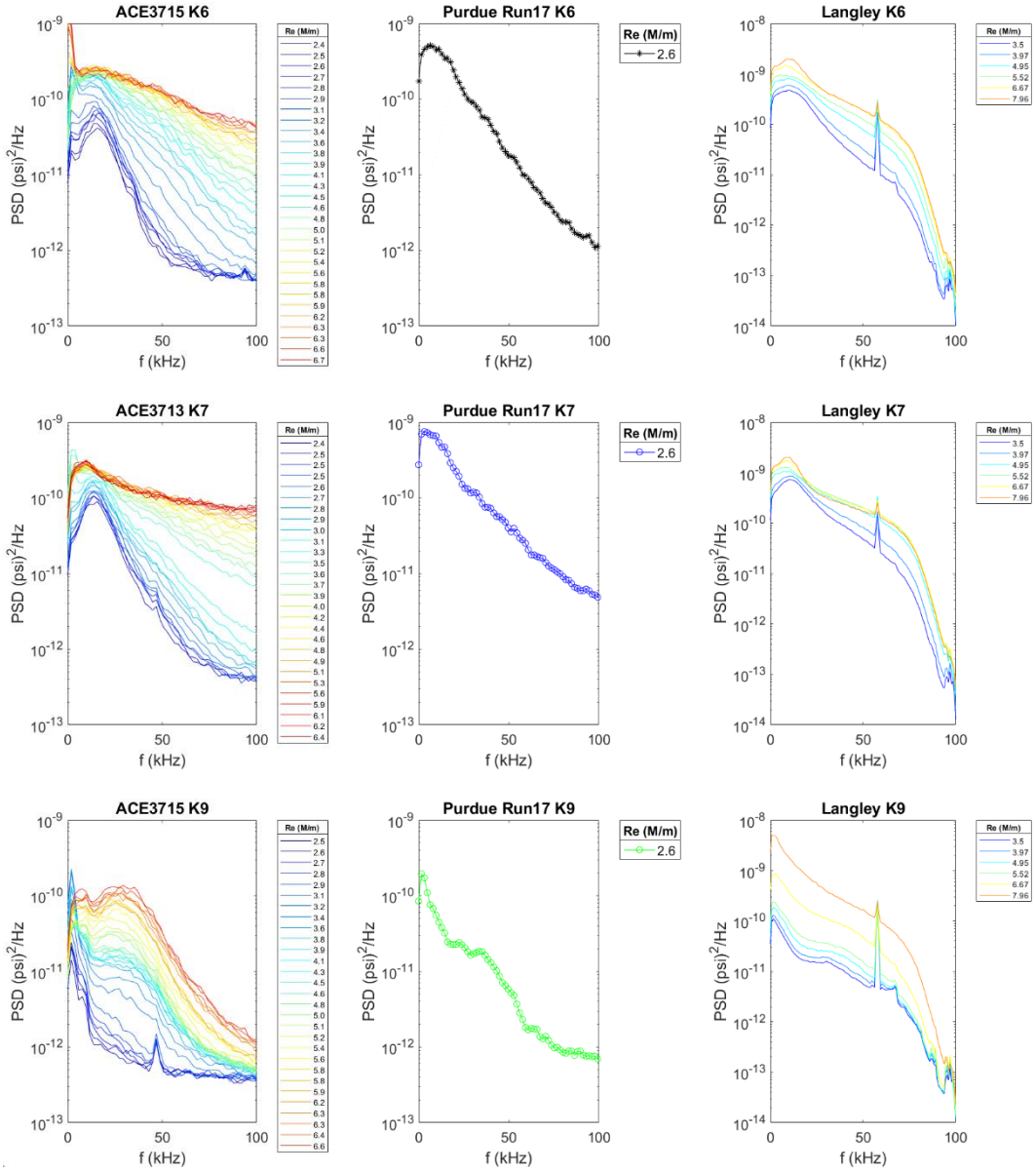

Figure E-1. Continued.

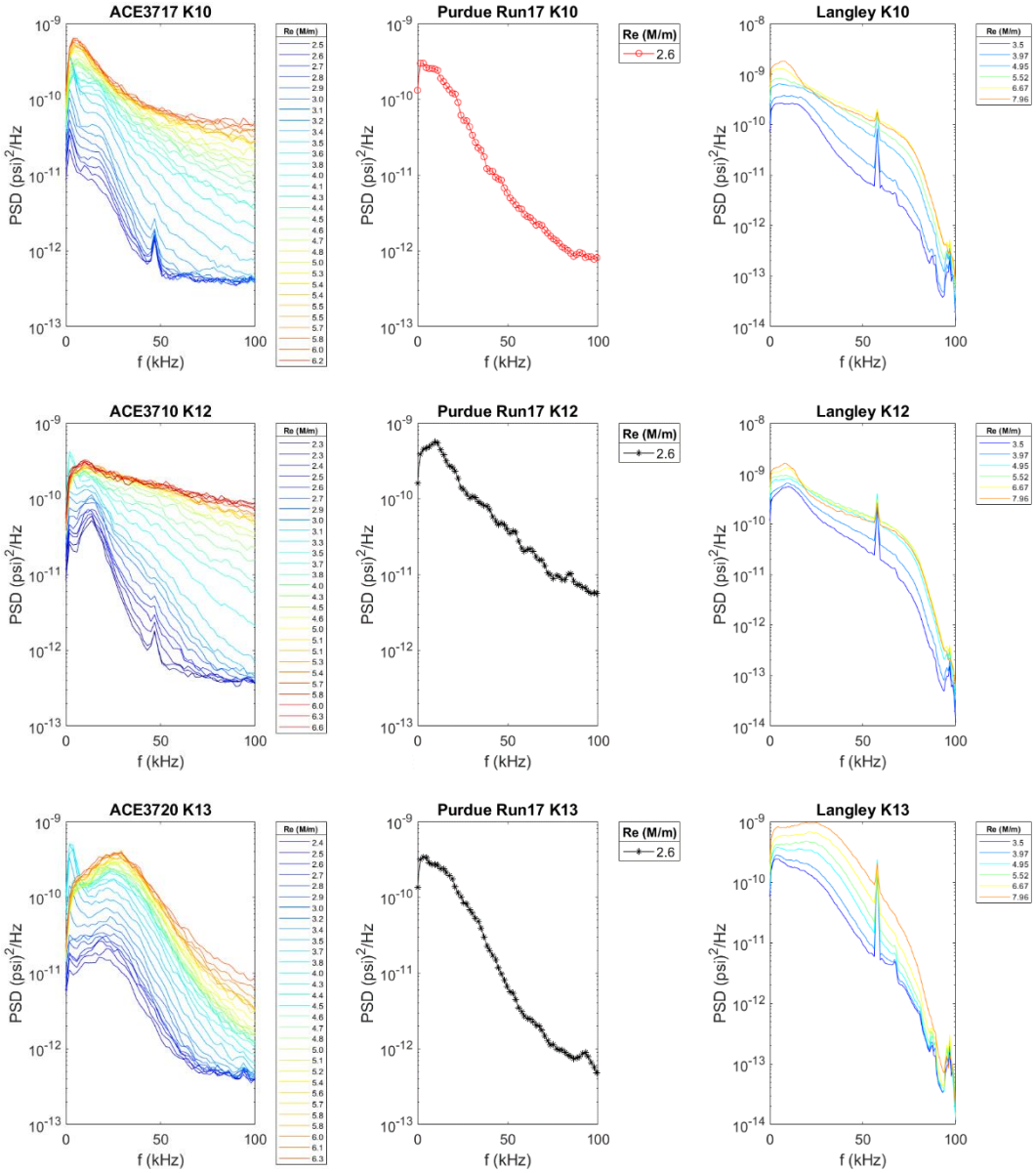

Figure E-1. Continued.

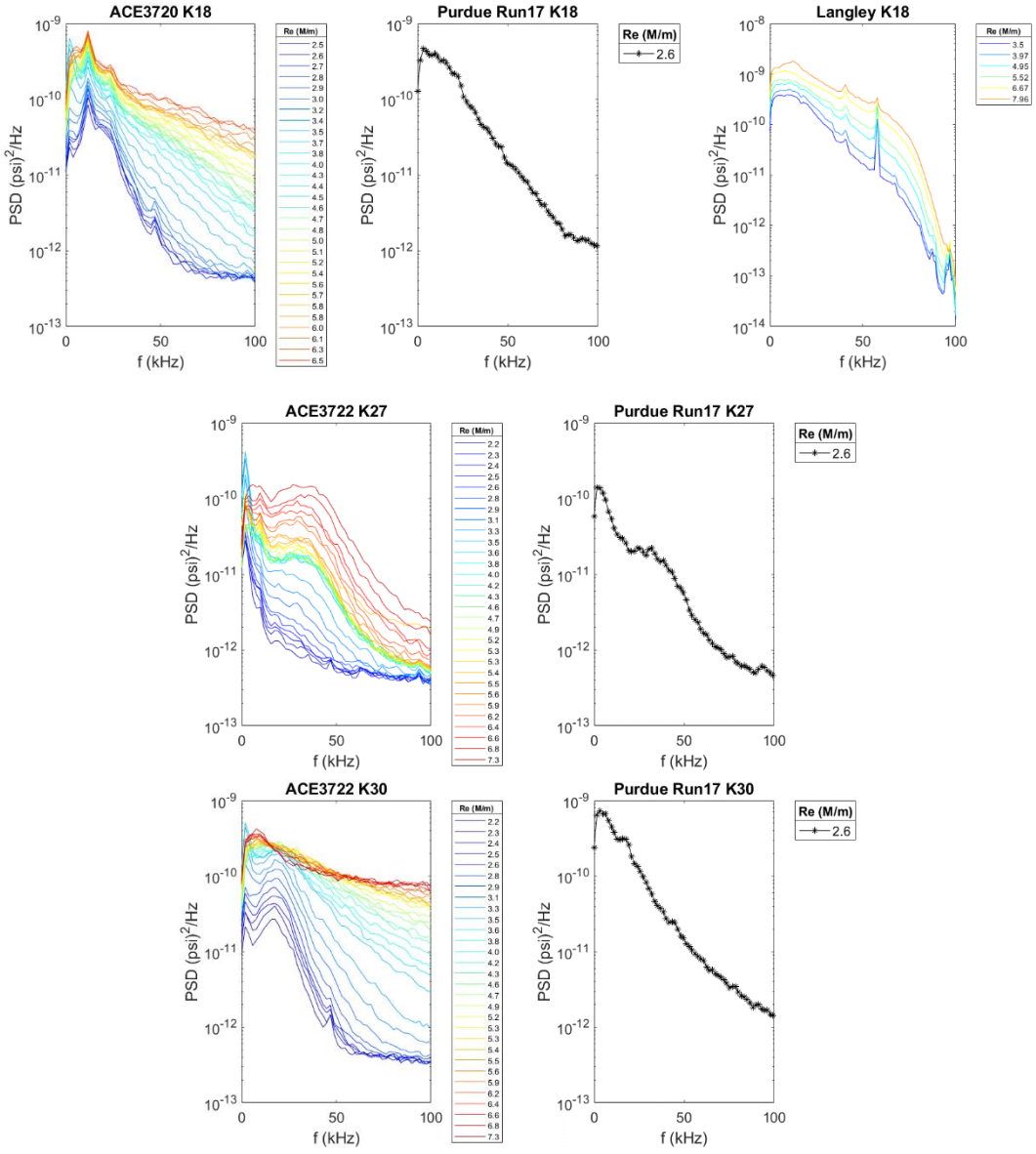

Figure E-1. Continued.

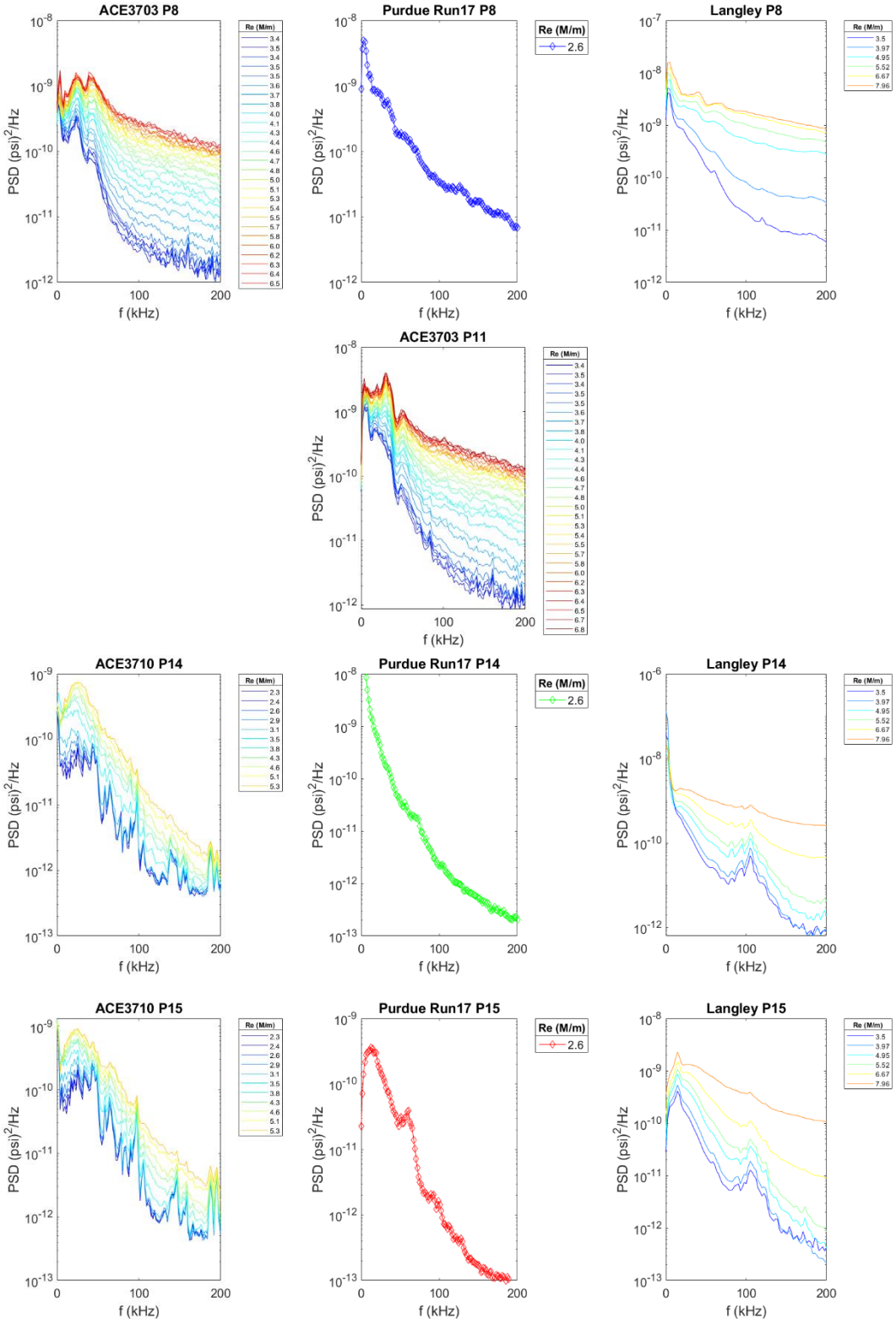

Figure E-1. Continued.

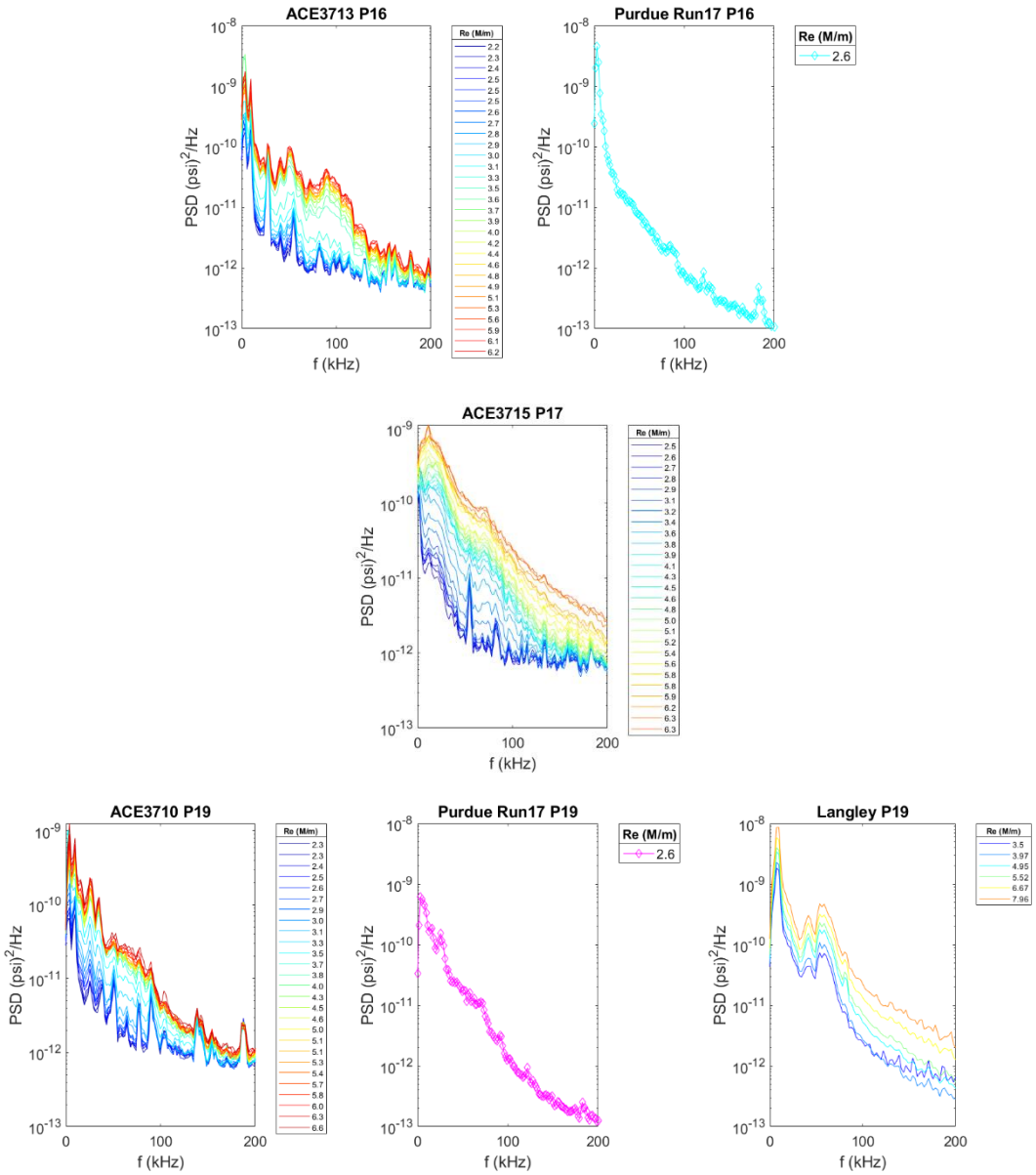

Figure E-1. Continued.

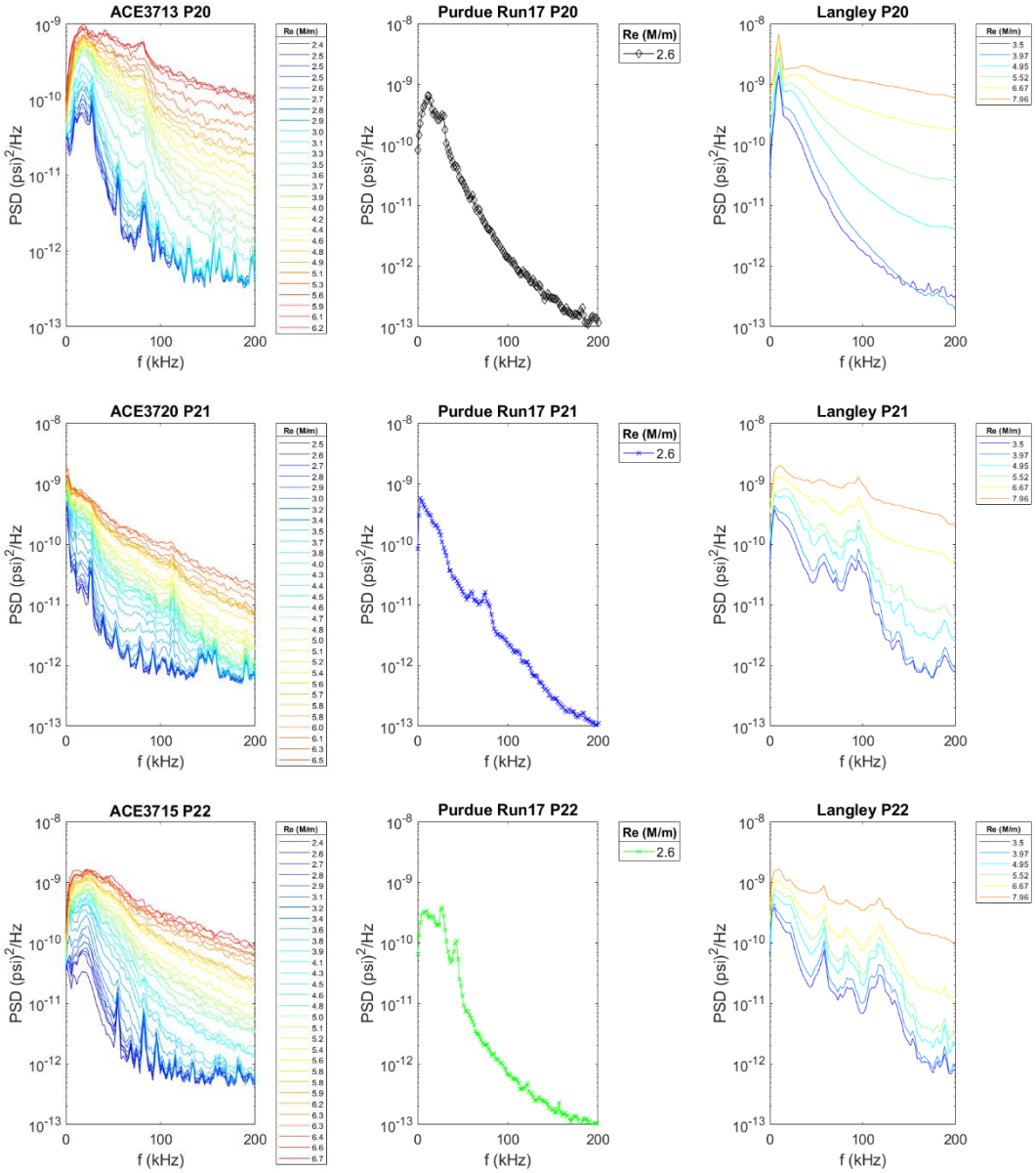

Figure E-1. Continued.

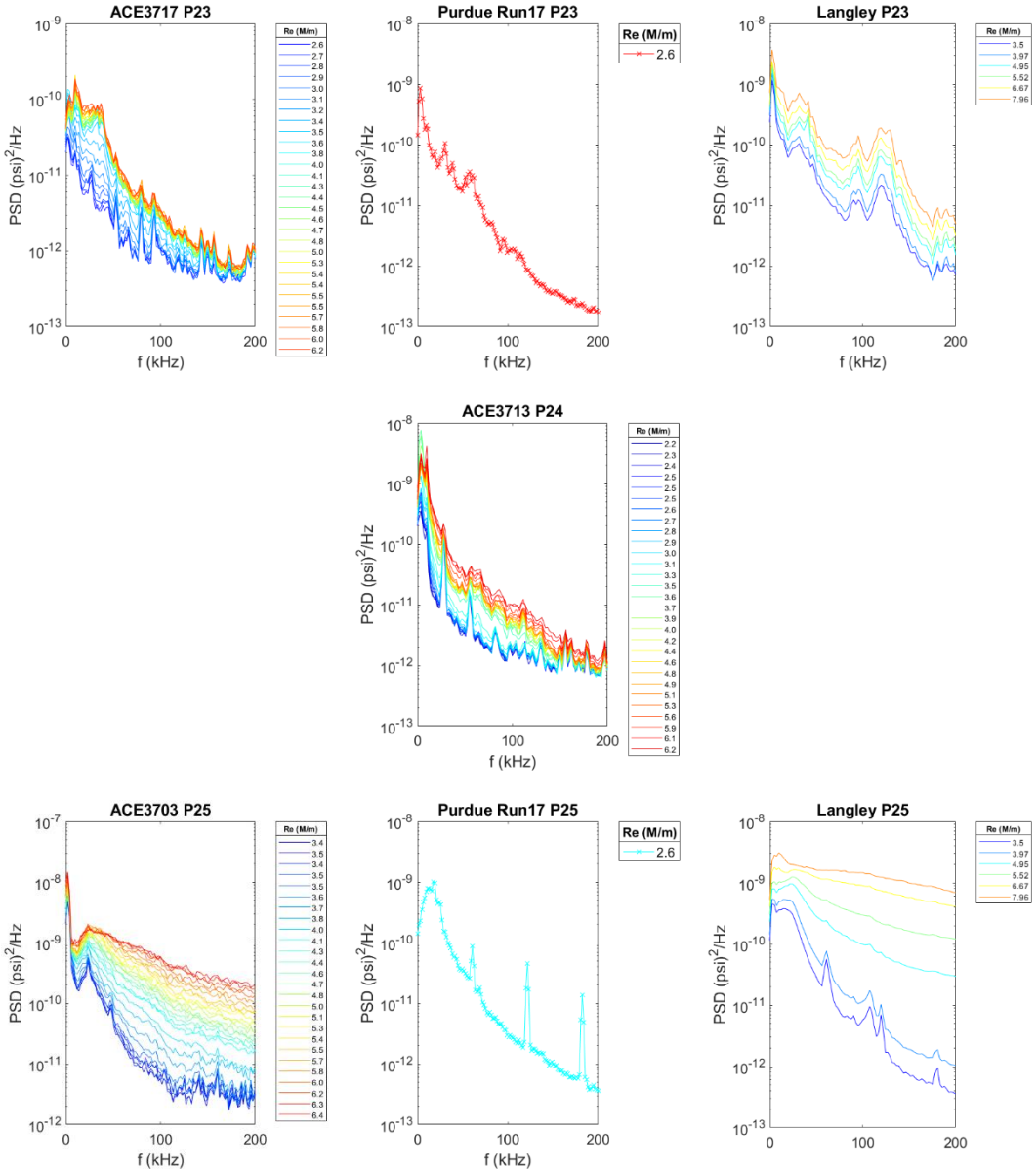

Figure E-1. Continued.

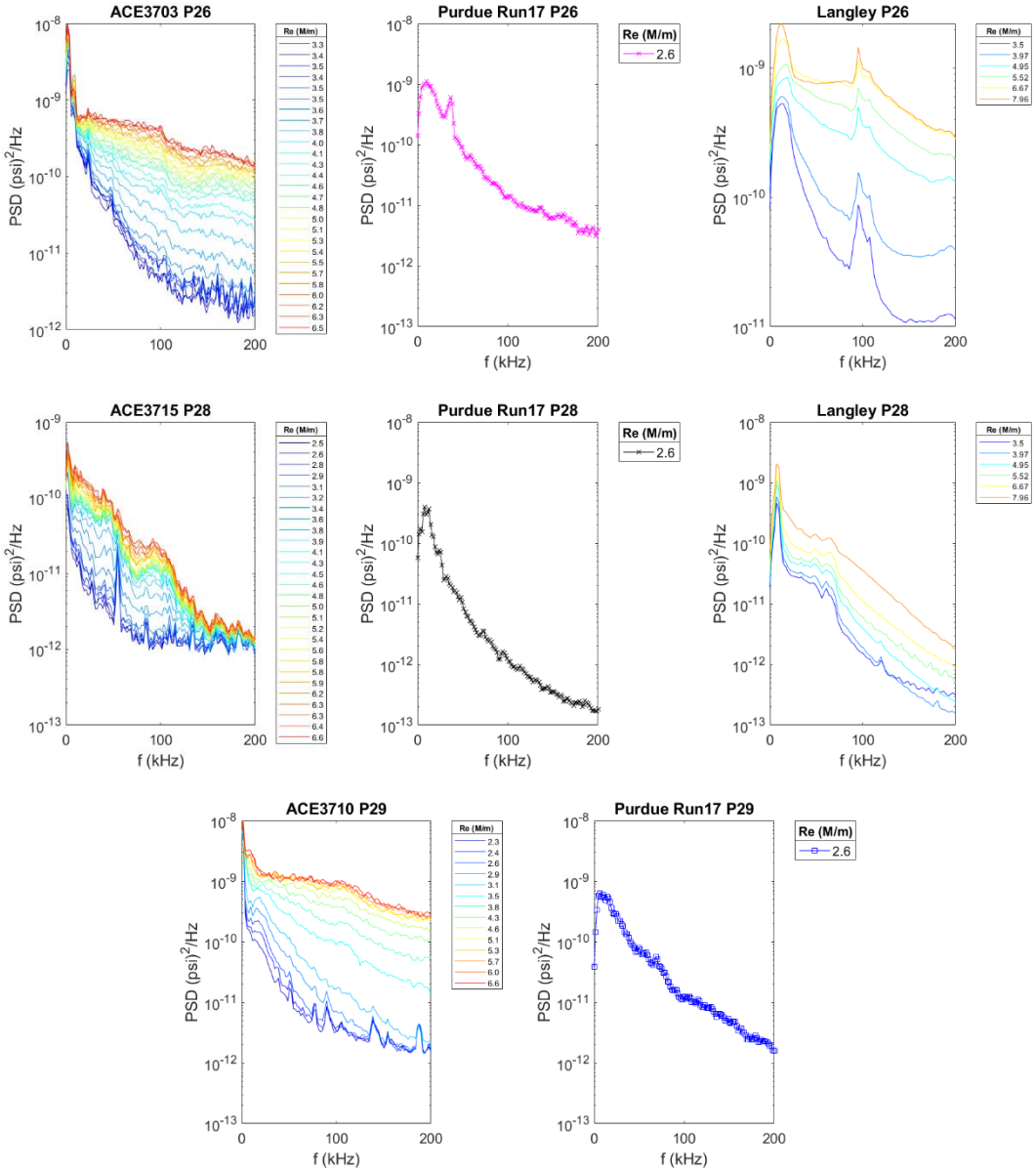

Figure E-1. Continued.

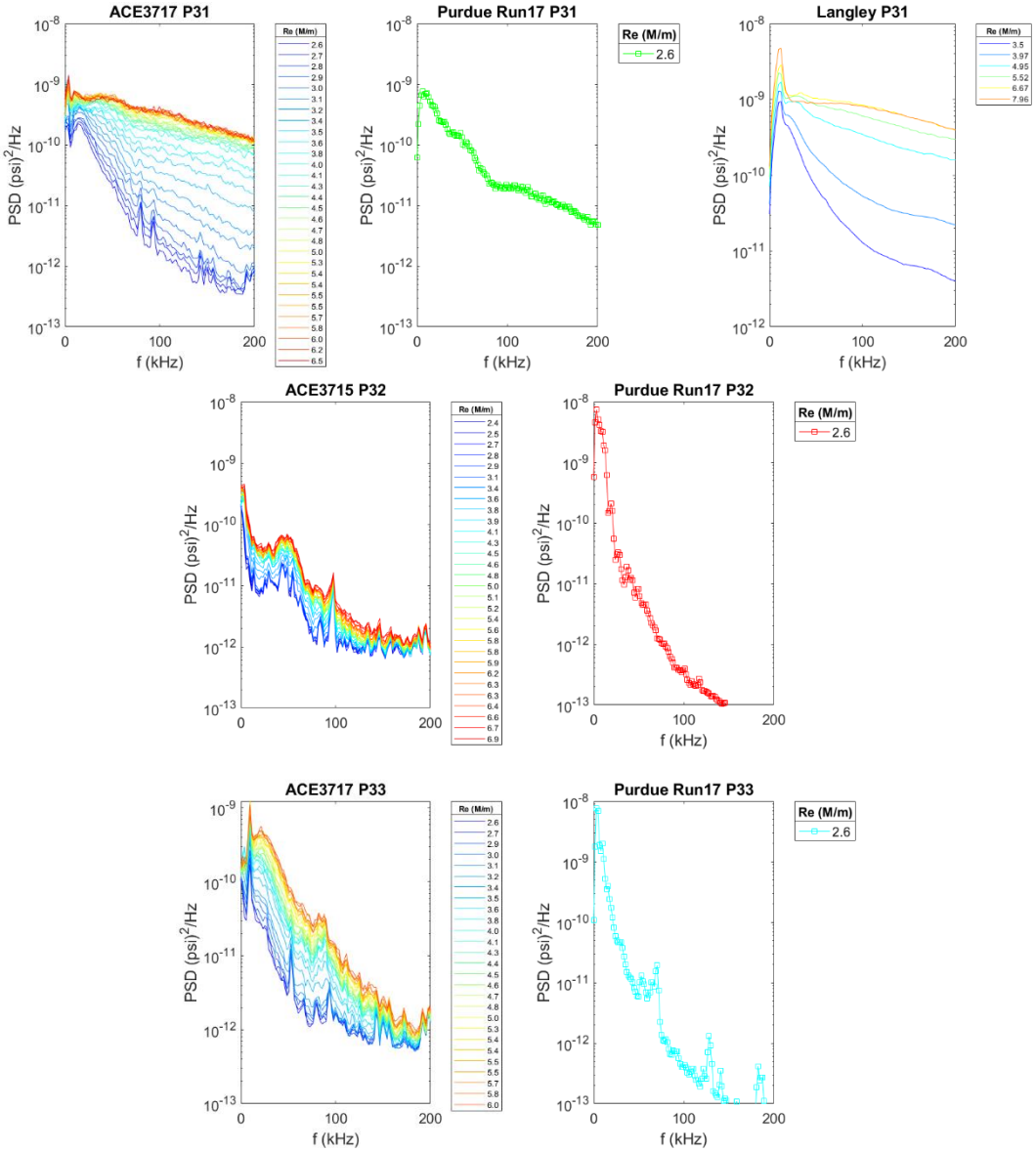

Figure E-1. Continued.

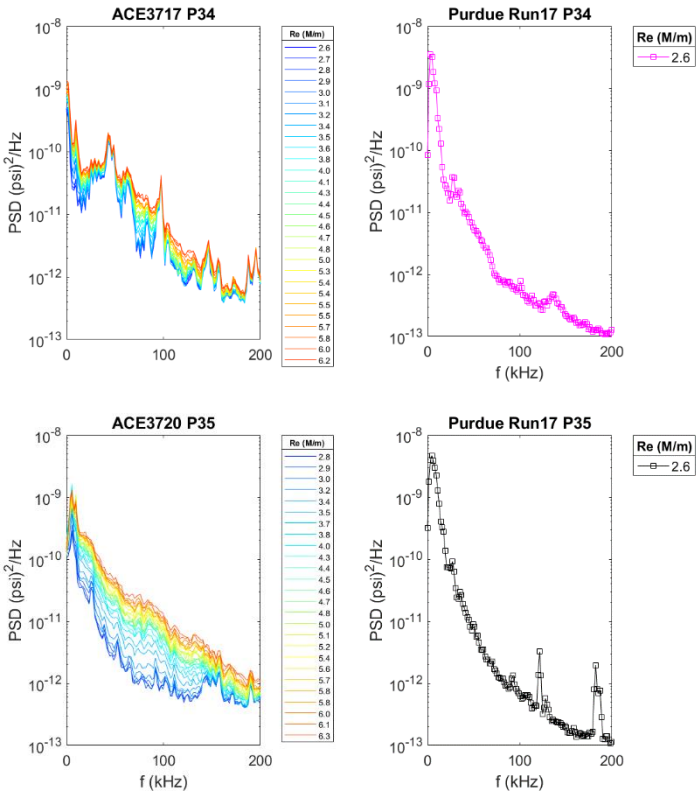

Figure E-1. Continued.

APPENDIX F

SURFACE PRESSURE SPECTRA (QUIET)

Surface pressure transducer data from TAMU and Purdue for quiet flow. Some measurements were not taken in each facility. Plots from Chapter 3 are repeated here for completeness of all 35 sensors. The results are labeled in sensor number order.

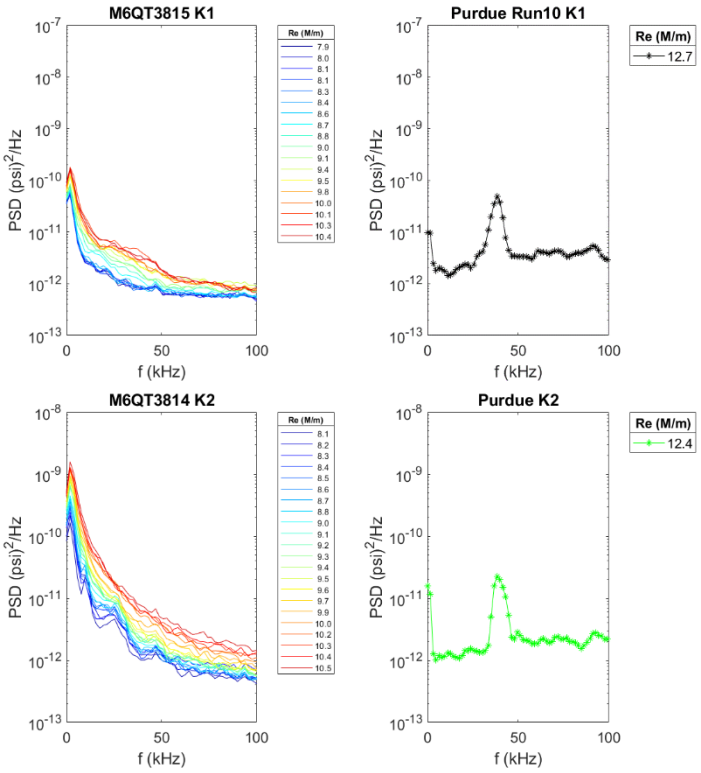

Figure F-1. Surface pressure spectra for every sensor located on JHUAPL BOLT 33% scale model; quiet flow

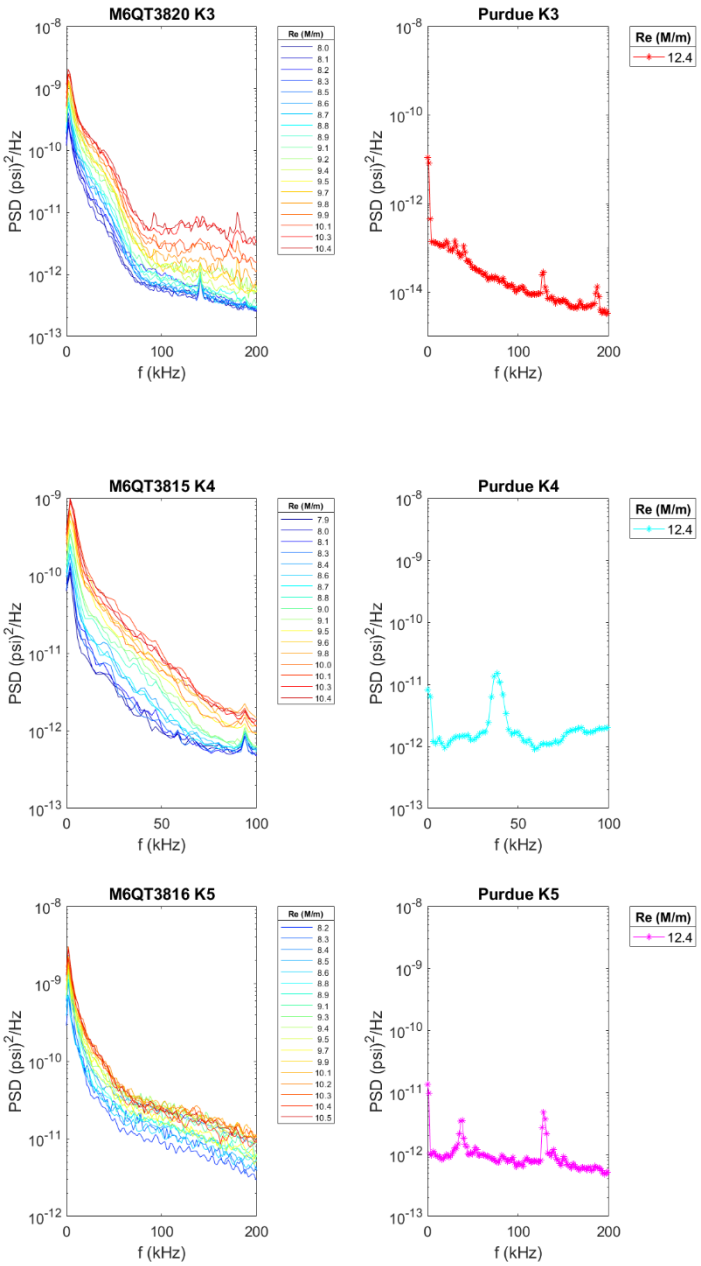

Figure F-1. Continued.

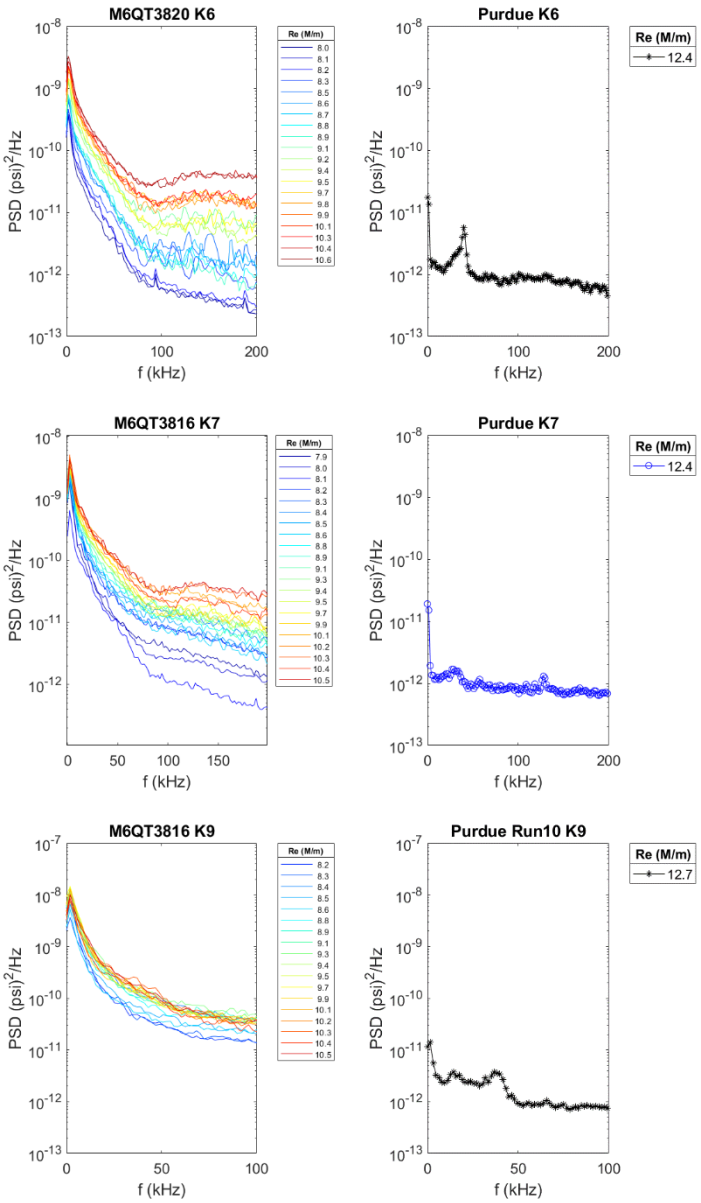

Figure F-1. Continued.

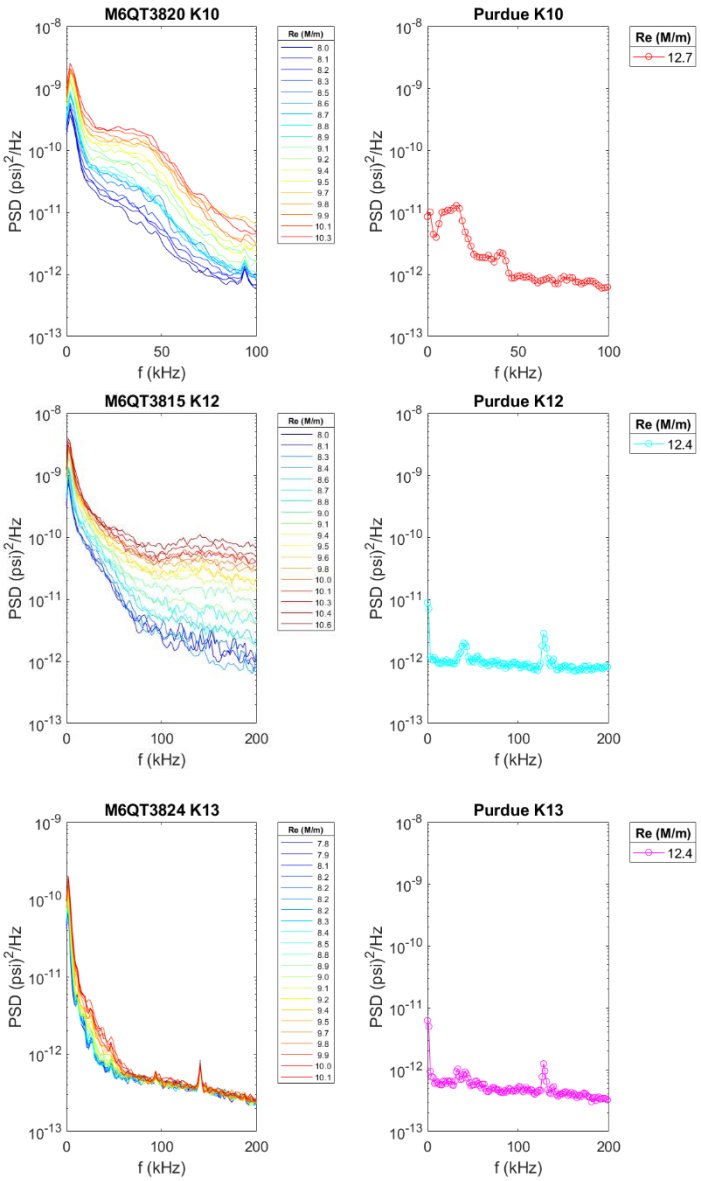

Figure F-1. Continued.

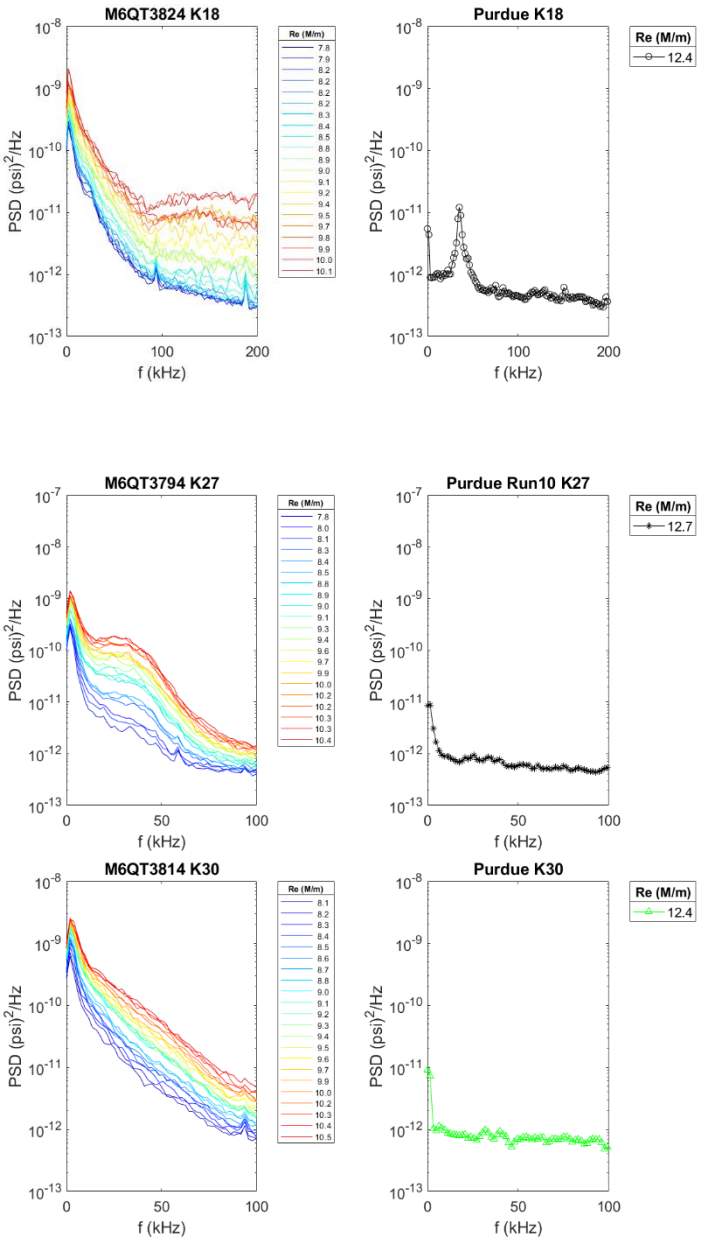

Figure F-1. Continued.

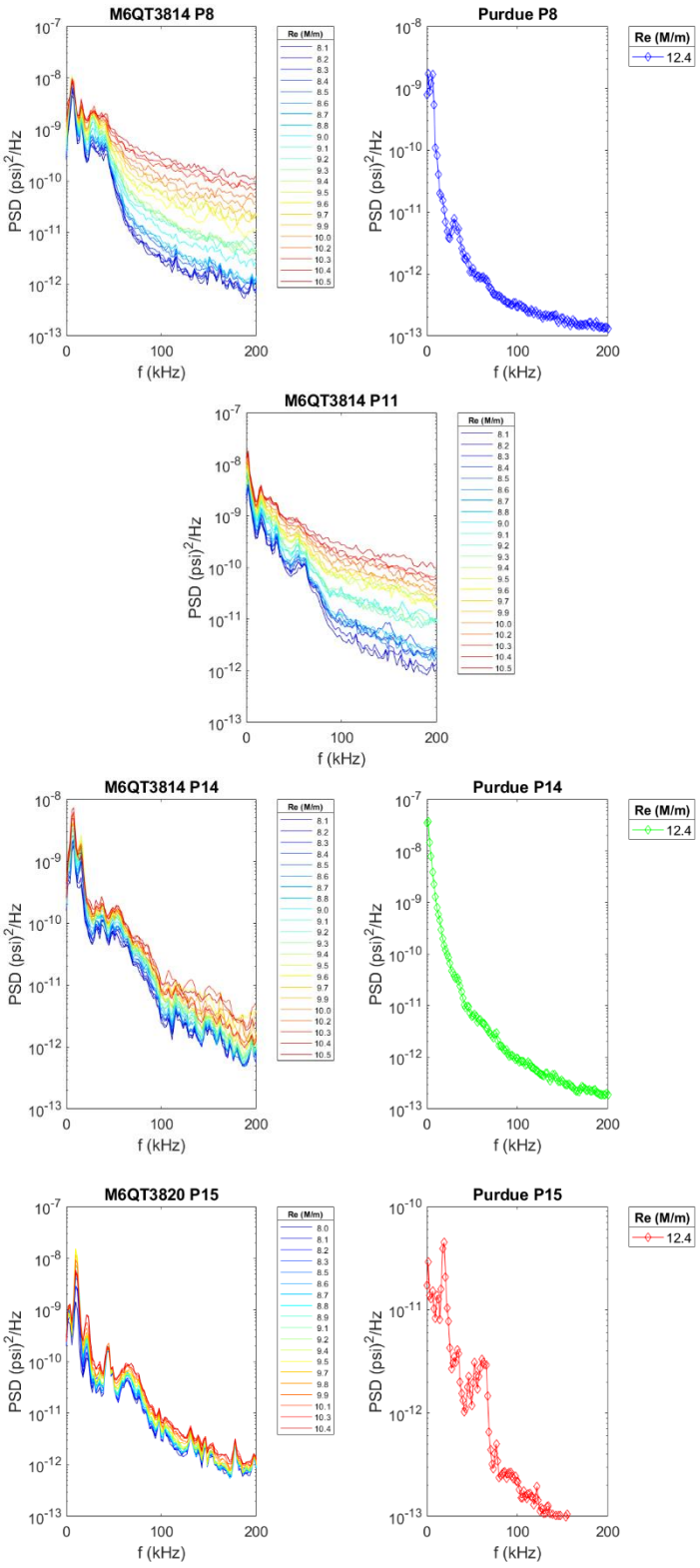

Figure F-1. Continued.

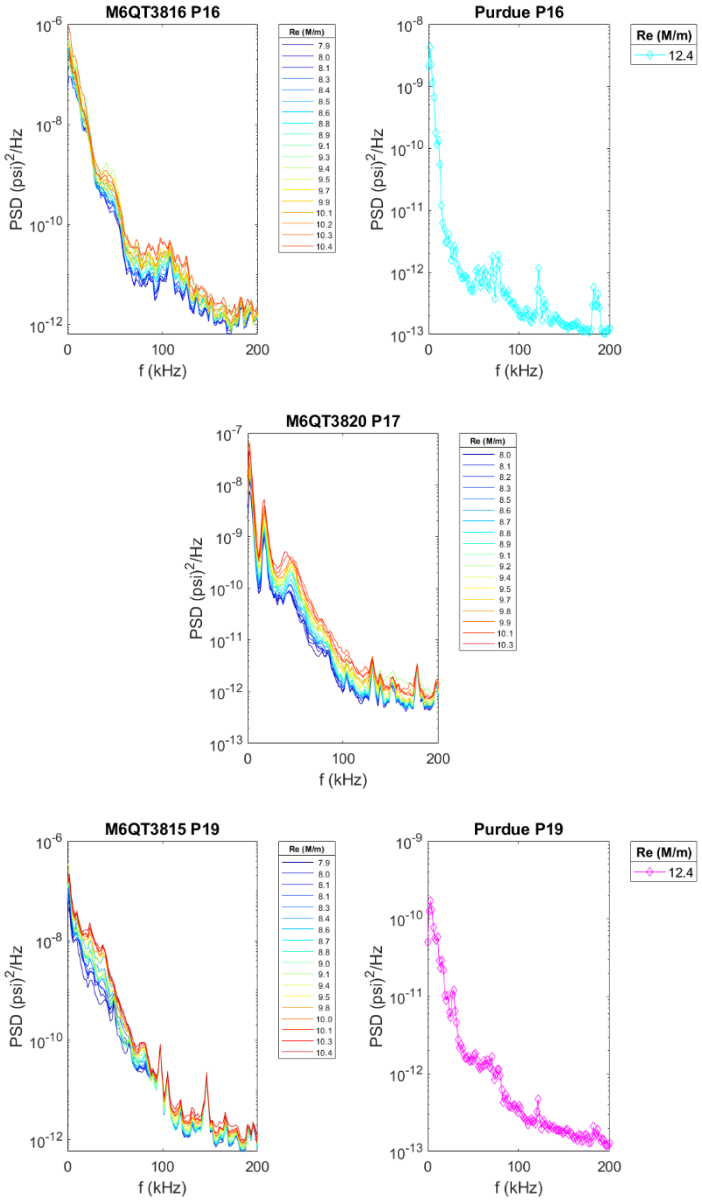

Figure F-1. Continued.

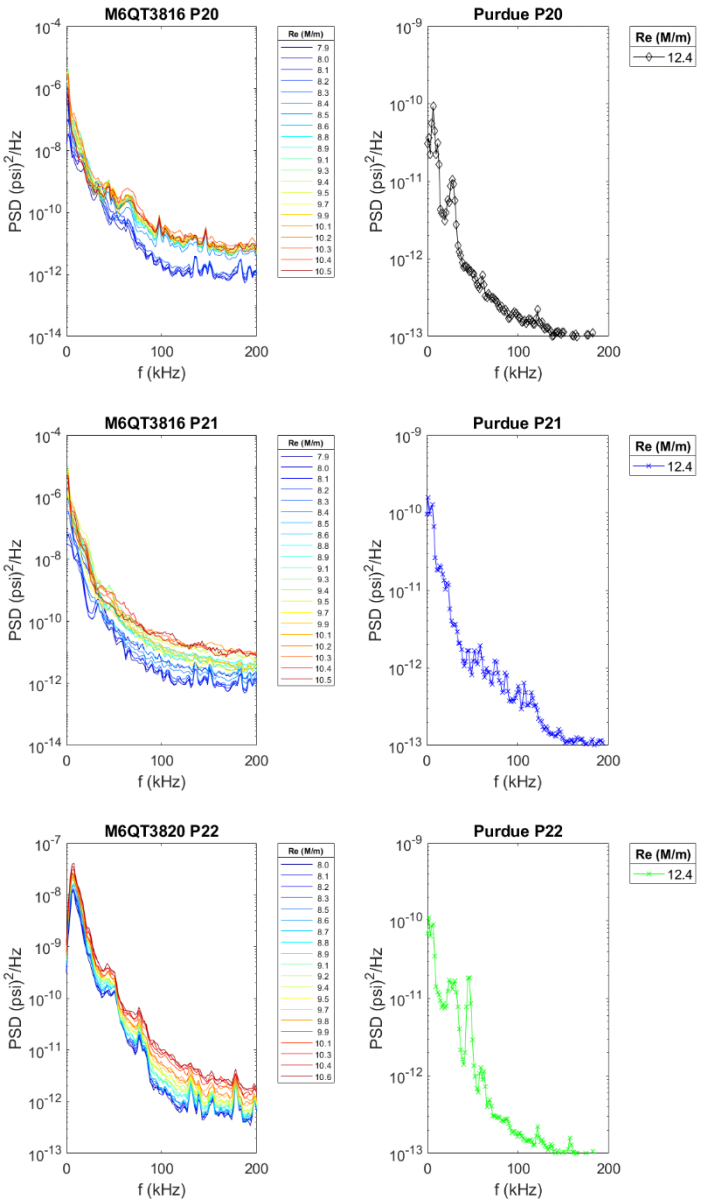

Figure F-1. Continued.

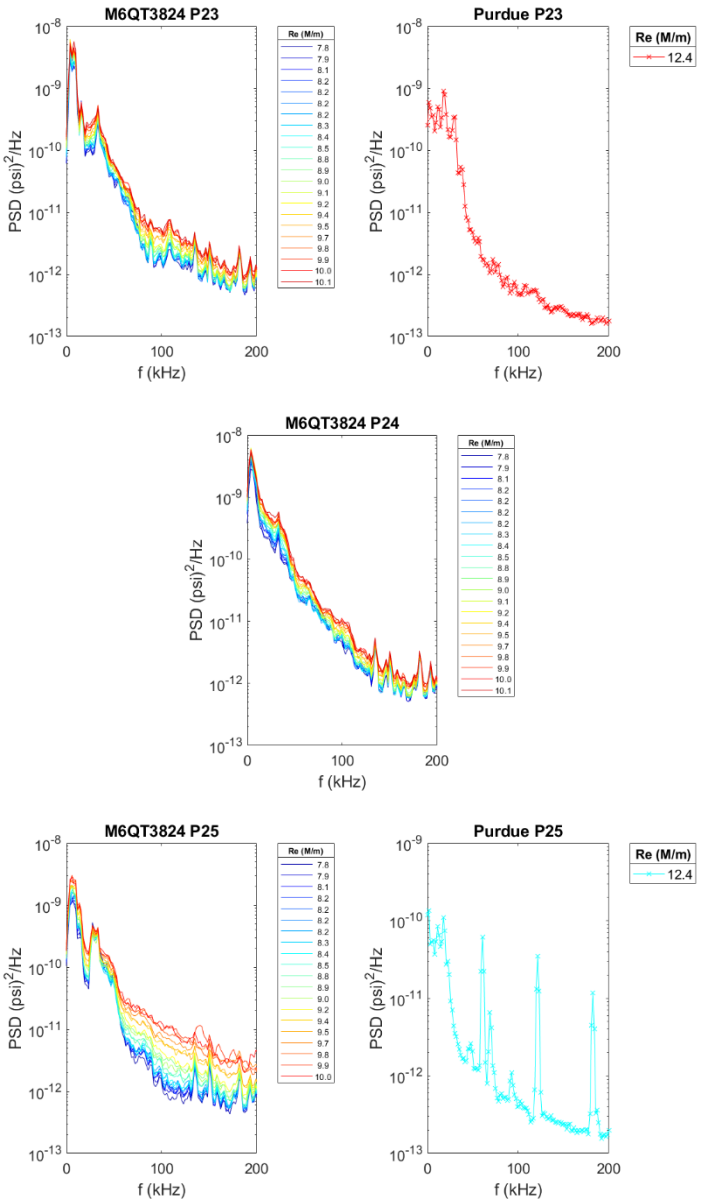

Figure F-1. Continued.

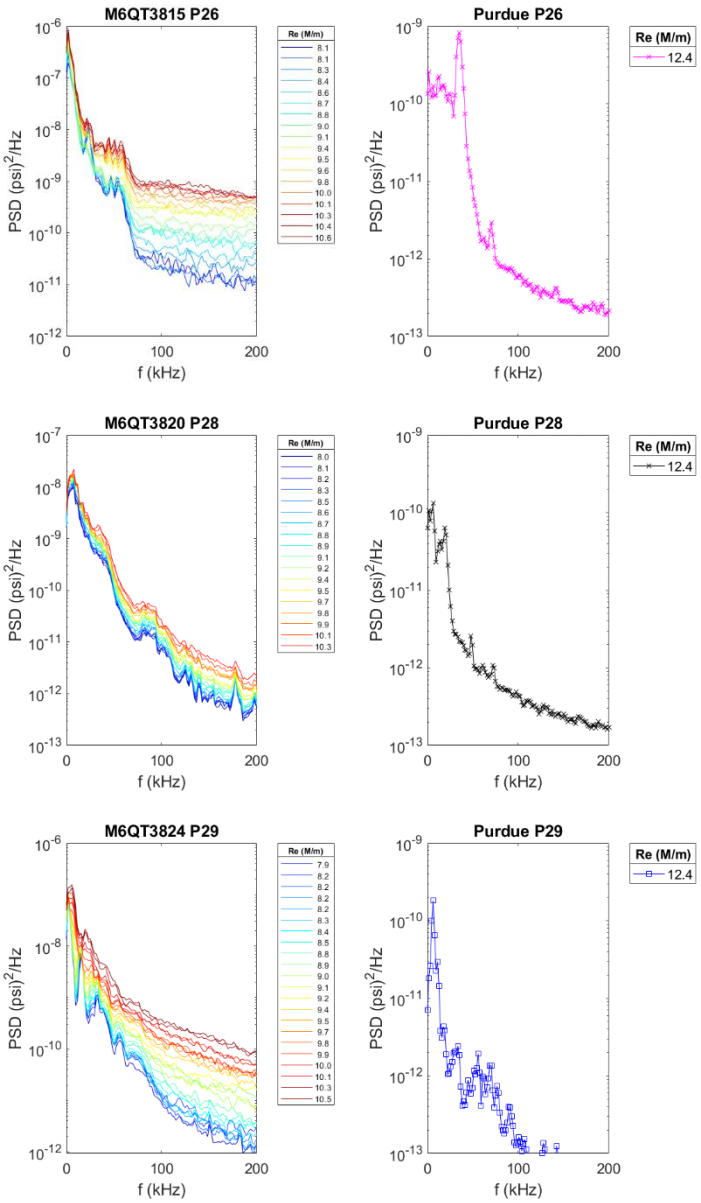

Figure F-1. Continued.

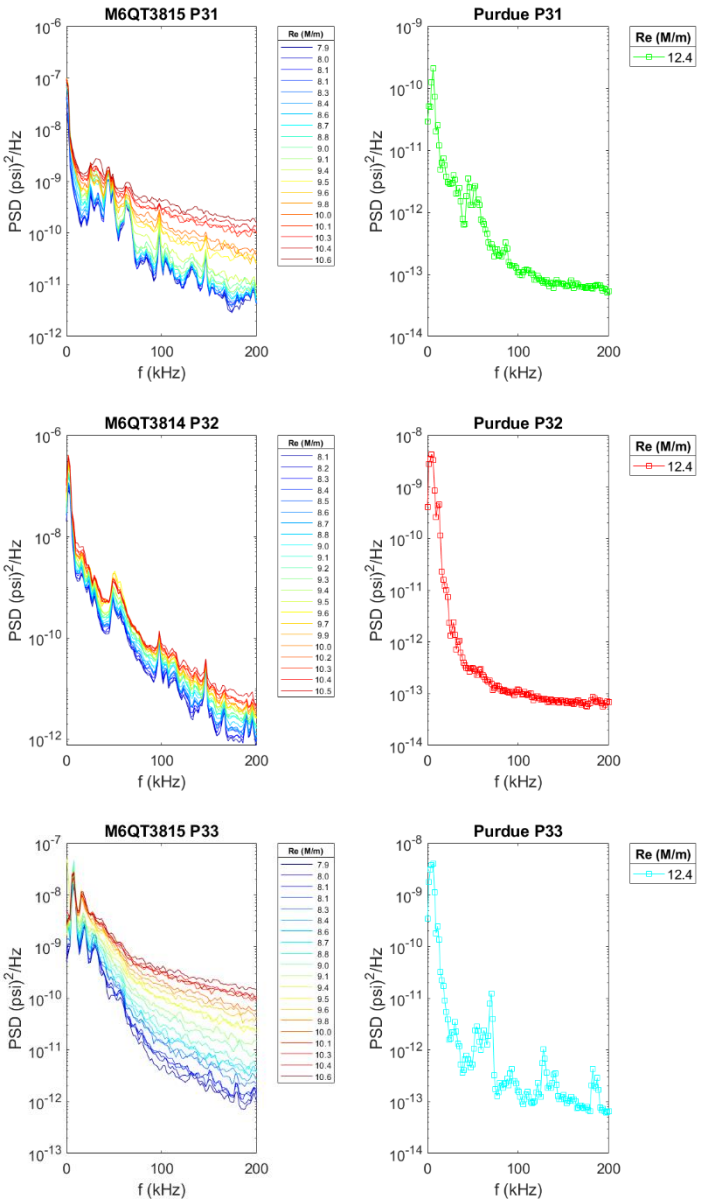

Figure F-1. Continued.

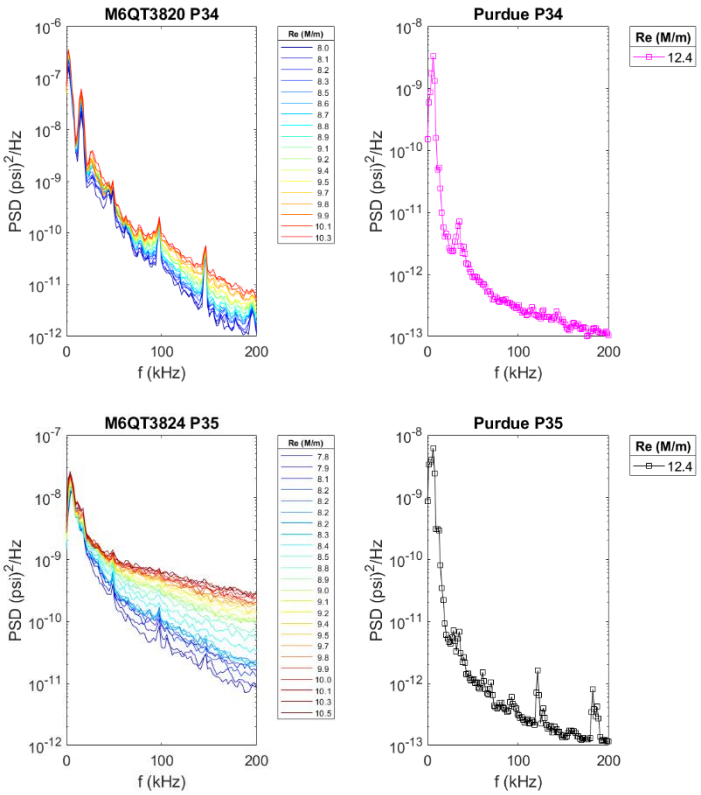

Figure F-1. Continued.

APPENDIX G

PAST BOLT IR DATA

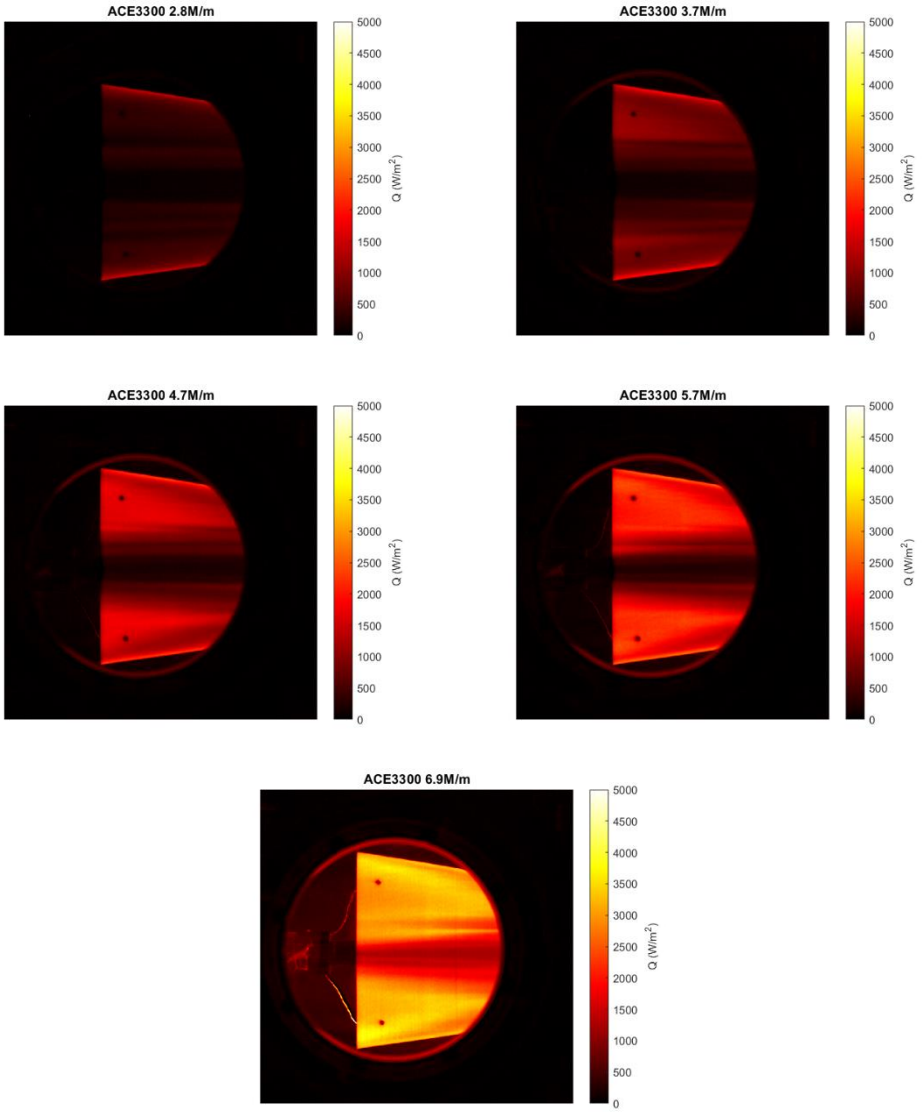

Figure G-1. 31% scale BOLT geometry, ACE tunnel results, polycarbonate material, Reynolds sweep, heat flux results, flow is from right to left

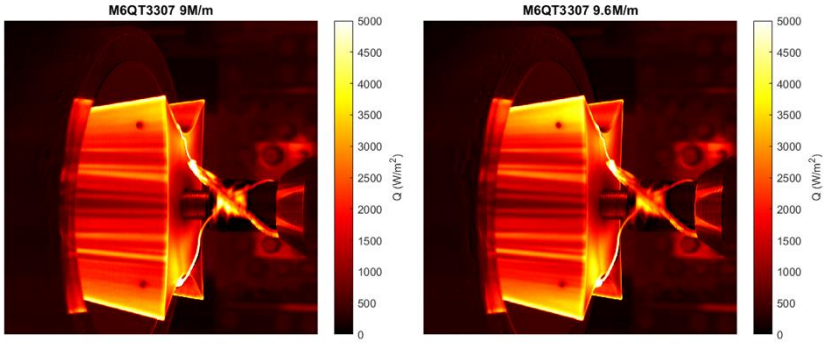

Figure G-2. 31% scale BOLT geometry, M6QT results, polycarbonate material, heat flux results, flow is from left to right